# Generation of Nonclassical States of Light from Linear Photonic Molecules to Linearly Uncoupled Resonators
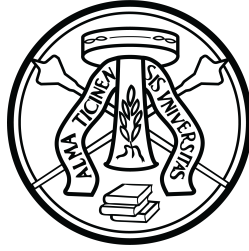
Luca Zatti

Tesi per il conseguimento del titolo

*If you can't explain something to a first year student,*
*then you haven't really understood.*
*Richard P. Feynman*

# Generation of Nonclassical States of Light from Linear Photonic Molecules to Linearly Uncoupled Resonators

Luca Zatti

A dissertation submitted to the Graduate School in Physics
in partial fulfillment of the requirements for the degree of

*Doctor of Philosophy in Physics*

Supervised by Prof. Marco Liscidini

University of Pavia
Department of Physics

Luca Zatti

*Generation of Nonclassical States of Light from Linear Photonic Molecules to Linearly Uncoupled Resonators*

Pavia, Italy (2022)

# Abstract

The focus of this PhD research is the theoretical study of the generation of non-classical states of light by parametric fluorescence in integrated devices. The analyzed quantum phenomena are spontaneous four-wave mixing (SFWM) and spontaneous parametric down conversion (SPDC). The core idea of this research is to study systems composed of two resonators and take advantage of the possible coupling between them, maximizing the generation efficiency of the selected nonlinear process. Here, we present two main strategies: the strong linear coupling and the linear uncoupling. The former exploits the interaction between two resonators that behave like two atoms of a (photonic) molecule, by playing on the common resonances that they may have. The latter relies on the linear uncoupling of two resonators that can interact solely through a nonlinear interaction, with light circulating in one resonator that cannot flows into the other. Among all the possibilities to achieve this (un)coupling, we study two situations: one where the coupling is obtained by the use of a directional coupler and one where it's obtained by the use of a Mach-Zehnder interferometer. The result of the linear uncoupling of two resonators, while maintaining the nonlinear coupling between them, depends strongly on the type of process under consideration. We investigate both SFWM and SPDC in both kinds of coupling situation, the challenges that can be encountered and what solutions can be used to overcome the different problems. We see how the strong coupling strategy is best suitable to suppress nonlinear parasitic processes without compromising the generation efficiency, resulting in a high-level of squeezing of the generated state; this platform can be used in a quantum computation framework for the generation of q-bits. On the other hand, with the linear uncoupling strategy we can obtain the independent control on the linear properties of the two resonators, enabling the suppression of parasitic processes and the generation of photon pairs, with a fine control on their spectral properties, in a reconfigurable photonic chip.

# Contents

# Introduction

The field of integrated photonics has become of paramount importance in the framework of quantum technologies. Its basic idea is to encode information in a quantum state and then exploit the main features of quantum mechanics, such as superposition and entanglement, to perform quantum computation, quantum communication, and quantum metrology. Photons are one of the best candidates to play this role. For example, using photons as quantum bit (q-bit) allows to work at room temperature, instead of the liquid-nitrogen temperature for superconductive q-bits, and employing light to transmit information is more efficient with respect to electrical signals, thanks to the ease with which light can be guided. There are many different ways to generate a quantum state of light. For example, single molecules, Rydberg atoms, colour centers and quantum dots are used as single photon sources. Instead, parametric fluorescence can be exploited to generate single or multiple photon pairs or squeezed light.

In this research, we studied the theory regarding the generation of photon pairs through second- and third-order nonlinear processes such as spontaneous parametric down conversion (SPDC) and spontaneous four-wave mixing (SFWM). These are nonlinear processes and lack in efficiency, because the optical nonlinear response of most systems far from electronic transitions is very weak. Integrated structures are thus the most convenient way to examine these phenomena, by exploiting spatial and temporal light confinement. Depending on the process, different platforms can be analyzed, such as Lithium Niobate for SPDC and Silicon or Silicon Nitride for what concerns SFWM. During this research we had the chance to collaborate with several research groups, providing the theoretical model to both study and design the most suitable structure and to validate the theory after the experiment was performed. In particular, we studied the generation of quantum states of light in systems composed of two coupled resonators, where the key point is the strength of the coupling between them. In fact, they can be strongly linearly coupled, to form a linear photonic molecule, or they can be linearly uncoupled, but coupled through the nonlinear interaction, to form a nonlinear photonic molecule. The main advantage of exploiting a molecule is the possibility to play with the set of resonances of each resonator (the atoms composing the molecule), adjusting the spectral position, splitting or eliminating the wanted and unwanted resonances. This kind of flexibility is a very desirable feature

of an integrated structure that, once is fabricated, cannot be modified. Obtaining quantum light states generation and control on chip is one of the most desired target, for an out-of-laboratory spreading of this technology. Differently, by linearly uncouple two resonators we can achieve the independent control of their linear properties, allowing for a reconfigurable structure, that can be tuned easily thanks to electrical heaters or electro-optical modulators.

In the first chapter of this manuscript, we recall the necessary theoretical formalism and retrace the derivation of the most important equations. In the second chapter we describe the first strategy of strongly couple two resonators and in the third chapter we address the second strategy of linearly uncouple two resonators that still remain coupled through a nonlinear interaction. The simulations in this thesis were mainly performed thanks to a custom *Python* code that we developed and kept on upgrading during these years of work. We used this code to simulate and study the different structures, improving its efficiency and reliability, by comparing the simulations with experimental data and other groups' results. We are currently collaborating with theoretical and experimental research groups at the University of Toronto (CA), at Xanadu Quantum Technology in Toronto (CA), at CEA-LETI in Grenoble (FR), at the University of Munster (GE), and at NIST in Maryland (US), other than the one here at the University of Pavia. Our task is to provide the theoretical model and the best parameter for efficient designs and to perform simulations to estimate the properties of the analyzed structures.

# Theoretical formalism

In this chapter, we review the theory necessary to face the generation of nonclassical states of light in integrated structures. We discuss the quantization of the field in an integrated device, fundamental concepts of nonlinear quantum optics and the coupling of two resonators, to conclude with the main features of a ring resonator.

## 1.1. Quantization in an integrated device

The first step to describe quantum states of light is, of course, to quantize the electromagnetic field. This goal can be achieved in several ways. To properly deal with nonlinear optics, though, it has been shown [1] that we need to quantize the field in terms of the displacement field $\boldsymbol{D}$ instead of the usual $\boldsymbol{E}$, otherwise we would get incorrect expressions for three and higher-order photon interaction terms in the Hamiltonian describing usual nonlinear processes, such as parametric down conversion, frequency conversion, and four-wave mixing. Maxwell's equations in absence of sources are

$$\frac{\partial}{\partial t}\boldsymbol{B}(\boldsymbol{r},t) = -\nabla \times \boldsymbol{E}(\boldsymbol{r},t) \ ,$$
$$\frac{\partial}{\partial t}\boldsymbol{D}(\boldsymbol{r},t) = \nabla \times \boldsymbol{H}(\boldsymbol{r},t) \ ,$$
$$\nabla \cdot \boldsymbol{B}(\boldsymbol{r},t) = 0 \ ,$$
$$\nabla \cdot \boldsymbol{D}(\boldsymbol{r},t) = 0 \ , \tag{1.1}$$

and this way of writing them also suggests that we should focus on $\boldsymbol{B}$ and $\boldsymbol{D}$. The first two equations can be seen as the equation of motion for the two field operators and the last two equations as the boundary conditions. Then, we need to write $\boldsymbol{E}$ and $\boldsymbol{H}$ in terms of $\boldsymbol{D}$ and $\boldsymbol{B}$. In general, only non-magnetic materials are considered, thus we use the following constitutive relations

$$\boldsymbol{D}(\boldsymbol{r},t) = \varepsilon_0 \varepsilon_r(\boldsymbol{r})\boldsymbol{E}(\boldsymbol{r},t) \ ,$$
$$\boldsymbol{B}(\boldsymbol{r},t) = \mu_0 \boldsymbol{H}(\boldsymbol{r},t) \ , \tag{1.2}$$

with $\varepsilon_r(\boldsymbol{r})$ a position-dependent relative dielectric constant. With eqs. (1.2) we can solve Maxwell's equations.

To quantize the field we need a set of commutators and a Hamiltonian $\mathcal{H}$ that would lead to the dynamical equations of (1.1) when used in Hamilton's equation of motion for the operators $\boldsymbol{B}$ and $\boldsymbol{D}$

$$i\hbar\frac{\partial \boldsymbol{D}}{\partial t} = [\boldsymbol{D}, \mathcal{H}] \quad \text{and} \quad i\hbar\frac{\partial \boldsymbol{B}}{\partial t} = [\boldsymbol{B}, \mathcal{H}] \ . \tag{1.3}$$

The appropriate equal-time commutation relations are

$$\left[D^i(\boldsymbol{r}), D^j(\boldsymbol{r}')\right]\left[B^i(\boldsymbol{r}), B^j(\boldsymbol{r}')\right] = 0 \ ,$$

$$\left[D^i(\boldsymbol{r}), B^j(\boldsymbol{r}')\right] = i\hbar\epsilon^{ilj}\frac{\partial}{\partial r^l}\left[\delta(\boldsymbol{r} - \boldsymbol{r}')\right] . \tag{1.4}$$

The Hamiltonian is obtained integrating the energy density, defined as

$$d\mathfrak{h} = \boldsymbol{E} \cdot d\boldsymbol{D} + \boldsymbol{H} \cdot d\boldsymbol{B} \ , \tag{1.5}$$

over the quantization volume, resulting in

$$\mathcal{H} = \int_V \frac{D^i(\boldsymbol{r})D^i(\boldsymbol{r})}{2\varepsilon_0\varepsilon_r(\boldsymbol{r})}d\boldsymbol{r} + \int_V \frac{B^i(\boldsymbol{r})B^i(\boldsymbol{r})}{2\mu_0}d\boldsymbol{r} \ , \tag{1.6}$$

where we used the constitutive relations (1.2).

**1.1.1. Isolated resonators - Mode Expansion.** In the case of an isolated resonator, such as a ring resonator, a common strategy is to identify a set of modes $m$ with associated angular frequency $\omega_m$ for the field operators. To do so, we solve the linear Maxwell equations written in terms of $\boldsymbol{D}$ and $\boldsymbol{B}$, thanks to (1.2),

$$\frac{\partial}{\partial t}\boldsymbol{B}(\boldsymbol{r}, t) = -\frac{1}{\varepsilon_0}\nabla \times \left[\frac{\boldsymbol{D}(\boldsymbol{r}, t)}{\varepsilon(\boldsymbol{r})}\right]$$

$$\frac{\partial}{\partial t}\boldsymbol{D}(\boldsymbol{r}, t) = \frac{1}{\mu_0}\nabla \times \boldsymbol{B}(\boldsymbol{r}, t) \ , \tag{1.7}$$

which lead to the master equation

$$\Theta(\boldsymbol{B}_m(\boldsymbol{r})) = \frac{\omega_m}{c^2}\boldsymbol{B}_m(\boldsymbol{r}) \ , \tag{1.8}$$

where

$$\Theta(\ ) = \nabla \times \left[\frac{\nabla \times (\ )}{\varepsilon(\boldsymbol{r})}\right] \ , \tag{1.9}$$

is the Maxwell operator. We solve (1.7) by looking for stationary solutions of eq. (1.8) in the form

$$\boldsymbol{D}(\boldsymbol{r}, t) = \boldsymbol{D}_m(\boldsymbol{r})e^{-i\omega_m t} + \text{c.c.}$$
$$\boldsymbol{B}(\boldsymbol{r}, t) = \boldsymbol{B}_m(\boldsymbol{r})e^{-i\omega_m t} + \text{c.c. ,} \tag{1.10}$$

where c.c. means complex conjugate. With (1.10) we find a pair of fields associated to $\omega_m$ $(\boldsymbol{D}_m(\boldsymbol{r}), \boldsymbol{B}_m(\boldsymbol{r}))$ . Since Maxwell operator (1.9) must be Hermitian, fields associated with different modes are orthogonal, thus we normalize according to

$$\int_V \frac{\boldsymbol{E}_m^*(\boldsymbol{r}) \cdot \boldsymbol{E}_m(\boldsymbol{r})}{\varepsilon_0 \varepsilon_r(\boldsymbol{r})} d\boldsymbol{r} = \int_V \frac{\boldsymbol{B}_m^*(\boldsymbol{r}) \cdot \boldsymbol{B}_m(\boldsymbol{r})}{\mu_0} d\boldsymbol{r} = \frac{\hbar\omega_m}{2}. \tag{1.11}$$

In terms of these stationary solutions (1.10) we can write any $\boldsymbol{D}_m(\boldsymbol{r})$ and $\boldsymbol{B}_m(\boldsymbol{r})$ fields as

$$\boldsymbol{D}(\boldsymbol{r}, t) = \sum_m \left( a_m(t)\boldsymbol{D}_m(\boldsymbol{r}) + a_m^\dagger(t)\boldsymbol{D}_m^*(\boldsymbol{r}) \right)$$
$$\boldsymbol{B}(\boldsymbol{r}, t) = \sum_m \left( a_m(t)\boldsymbol{B}_m(\boldsymbol{r}) + a_m^\dagger(t)\boldsymbol{B}_m^*(\boldsymbol{r}) \right) , \tag{1.12}$$

where $a_m$ and $a_m^\dagger$ are the usual ladder operators for the mode $m$, that satisfy the commutation rules

$$\left[ a_m(t), a_{m'}(t) \right] = 0$$
$$\left[ a_m(t), a_{m'}^\dagger(t) \right] = \delta_{mm'} . \tag{1.13}$$

Substituting eq (1.12) in (1.6) with the use of (1.11), we get

$$\mathcal{H}_L = \sum_m \hbar\omega_m \left( a_m^\dagger(t)a_m(t) + \frac{1}{2} \right), \tag{1.14}$$

which is the well known linear Hamiltonian written in terms of ladder operators. This Hamiltonian does not depend on time, since the phases of the ladders operators cancel out.

**1.1.2. Asymptotic fields.** In this work, we will deal with general integrated structures with more than one optical element, that are more complex with respect to the standard ring resonator. We thus adopt the strategy of using the formalism of the so called asymptotic fields [2, 3]. Instead of expanding the fields as in (1.12), we use these particular stationary solutions of Maxwell equations as a basis to build the electromagnetic field. If we consider a structure composed of an arbitrary number of channels connected via an interaction region, as sketched in Fig. 1.1, an asymptotic-in wavepacket consists in general of an incoming wavepacket at $t \to -\infty$ in one channel, and outgoing fields in every channel at $t \to \infty$. Similarly, an asymptotic-out wavepacket consists of a single outgoing wavepacket at $t \to \infty$, and fields incoming from every channel at $t \to -\infty$.

In this framework, we explicit the subscript $k$, which indicates the continuous variable wavevector, to distinguish it from the discrete variable $m$ which represents the mode band where $\omega_{m,k}$ belongs. We can write the field operators in terms of either asymptotic-in or -out fields as

$$\boldsymbol{D}(\boldsymbol{r},t) = \sum_{X,m} \int dk\, \boldsymbol{D}_{m,k}^{\text{asy-in(out)(X)}}(\boldsymbol{r}) a_{m,k}^{\text{asy-in(out)(X)}}(t) + H.c.\ ,$$

$$\boldsymbol{B}(\boldsymbol{r},t) = \sum_{X,m} \int dk\, \boldsymbol{B}_{m,k}^{\text{asy-in(out)(X)}}(\boldsymbol{r}) a_{m,k}^{\text{asy-in(out)(X)}}(t) + H.c.\ , \qquad (1.15)$$

where $(X)$ denotes the channel where the asymptotic field expansion is defined, and $a^{\text{asy-in(out)(X)}}(k)$ are ladder operators which obey (1.13). The asy-out and asy-in states are not independent, for they are linked by the complex conjugation operation

$$\boldsymbol{D}_{m,k}^{\text{asy-out}}(\boldsymbol{r}) = \left[ \boldsymbol{D}_{m,k}^{\text{asy-in}}(\boldsymbol{r}) \right]^* \ ,$$

$$\boldsymbol{B}_{m,k}^{\text{asy-out}}(\boldsymbol{r}) = \left[ -\boldsymbol{B}_{m,k}^{\text{asy-in}}(\boldsymbol{r}) \right]^* \ . \qquad (1.16)$$

Due to their asymptotic behavior, the asymptotic-in expansion is a natural choice for any incoming pump or seed field, and the asymptotic-out expansion for output fields, such as fields generated by nonlinear processes.

As an example, in the simple case of a waveguide, as sketched in Fig. 1.2(a), if we consider only one channel (i.e. light incoming from the left) the asymptotic-in displacement field would be

$$\boldsymbol{D}_{m,k}^{\text{asy-in,wg}}(\boldsymbol{r}) = \sqrt{\frac{\hbar\omega_k}{4\pi}}\, \boldsymbol{d}_{m,k}(x,y) e^{ikz}\ , \qquad (1.17)$$

where $\boldsymbol{d}_{m,k}(x,y)$ is the displacement field distribution in the plane transverse to the propagation direction. Instead, in the case of a single ring resonator (Fig. 1.2(b)),
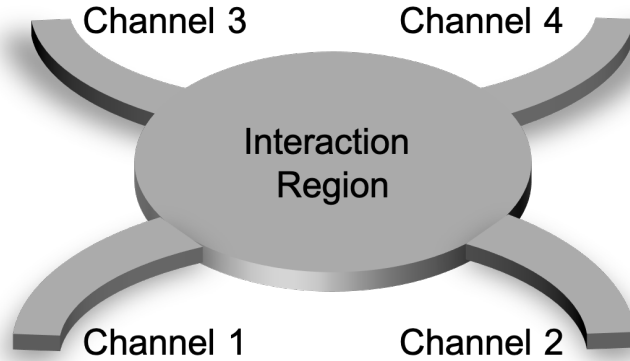


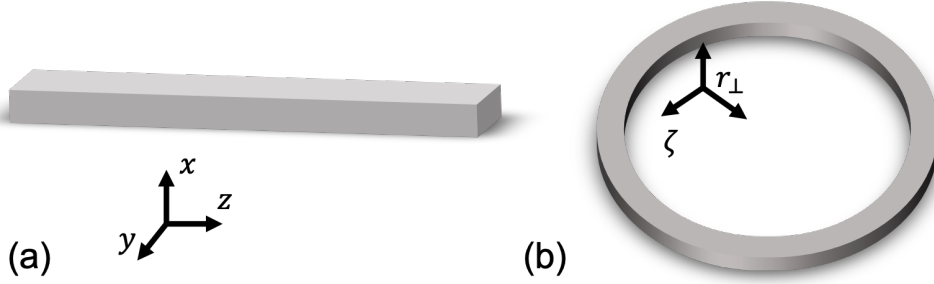FIGURE 1.1. Sketch of the system's interaction region with four channels.

FIGURE 1.2. (a) Sketch of a channel waveguide and (b) of a ring resonator.

we would have

$$\boldsymbol{D}_{m,k}^{\text{asy-in,ring}}(\boldsymbol{r}) = \sqrt{\frac{\hbar\omega_k}{4\pi}}\boldsymbol{d}_{m,k}(\boldsymbol{r}_\perp)f_k e^{ik\zeta} \ , \tag{1.18}$$

where $f_k$ is the field enhancement inside the ring, $\boldsymbol{r}_\perp$ and $\zeta$ are the transverse and longitudinal coordinates along the ring, respectively.

A subtle point in this framework is taking into account for losses. Even if absorption losses can be neglected, in a realistic system scattering losses should be included. Here the problem is how to calculate the asymptotic fields in the presence of such losses. The solution of modelling the structure using finite-difference-time-domain (FDTD) is impractical for large systems, for it would require a detailed description of the structure at the nanometer level. The effect of scattering is a decrease in the field intensity as light propagates both through a waveguide or inside a resonator. This loss can be modelled as an effective absorption [4]. A common way to describe this kind of absorption consists of introducing a complex wavevector $\tilde{k}$. For asymptotic-in states we have

$$\tilde{k}_{in} = k + i\frac{\xi}{2} \ , \tag{1.19}$$

where $k$ is the usual wavevector and $\xi$ brings into effect the field intensity decay due to the propagation losses. For asymptotic-out states we have

$$\tilde{k}_{out} = k - i\frac{\xi}{2} \ , \tag{1.20}$$

where we see that $\tilde{k}_{out} = [\tilde{k}_{in}]^*$. This strategy allows for a straightforward implementation of the losses inside the theoretical model that can be easily include in any numerical code.

## 1.2. Parametric Fluorescence

Parametric fluorescence is one of the various nonlinear effects that arise when the response of the polarization of a medium is non linear in the electric field. When light interacts with a medium, to describe the fields we have to include the polarization

field $\boldsymbol{P}(\boldsymbol{r}, t)$ in the definition of the constitutive relations (1.2) to get the general form

$$\boldsymbol{D}(\boldsymbol{r}, t) = \varepsilon_0 \boldsymbol{E}(\boldsymbol{r}, t) + \boldsymbol{P}(\boldsymbol{r}, t) \ . \tag{1.21}$$

Since the magnetic response can be neglected, we focus only on the electric contribution. To describe this effect, we consider the limit of a small nonlinear response of the medium and expand $\boldsymbol{P}(\boldsymbol{r}, t)$ in terms of $\boldsymbol{E}(\boldsymbol{r}, t)$ as

$$\begin{aligned}
P^i(\boldsymbol{r}, t) = {} & \varepsilon_0 \chi_{ij}^{(1)}(\boldsymbol{r}) E^j(\boldsymbol{r}, t) + \varepsilon_0 \chi_{ijl}^{(2)}(\boldsymbol{r}) E^j(\boldsymbol{r}, t) E^l(\boldsymbol{r}, t) \\
& + \varepsilon \chi_{ijlm}^{(2)}(\boldsymbol{r}) E^j(\boldsymbol{r}, t) E^l(\boldsymbol{r}, t) E^m(\boldsymbol{r}, t) + ... \ ,
\end{aligned} \tag{1.22}$$

where $i, j, l, m$ are the Cartesian components, that are to be summed over if repeated, and $\chi^{(n)}$ is the n-th order of the susceptibility tensor. We broke the expansion at the third order because we are interested in studying second- and third-order nonlinear phenomena, neglecting higher order terms. Since our choice of fundamental field was the displacement field, we use (1.21) to include (1.22) and write

$$\begin{aligned}
D^i(\boldsymbol{r}, t) = {} & \varepsilon_0 E^i(\boldsymbol{r}, t) + \varepsilon_0 \chi_{ij}^{(1)}(\boldsymbol{r}) E^j(\boldsymbol{r}, t) + \varepsilon_0 \chi_{ijl}^{(2)}(\boldsymbol{r}) E^j(\boldsymbol{r}, t) E^l(\boldsymbol{r}, t) \\
& + \varepsilon \chi_{ijlm}^{(3)}(\boldsymbol{r}) E^j(\boldsymbol{r}, t) E^l(\boldsymbol{r}, t) E^m(\boldsymbol{r}, t) \\
= {} & \varepsilon_0 \left[ \varepsilon_r(\boldsymbol{r}) E^i(\boldsymbol{r}, t) + \chi_{ijl}^{(2)}(\boldsymbol{r}) E^j(\boldsymbol{r}, t) E^l(\boldsymbol{r}, t) \right. \\
& \left. + \chi_{ijlm}^{(3)}(\boldsymbol{r}) E^j(\boldsymbol{r}, t) E^l(\boldsymbol{r}, t) E^m(\boldsymbol{r}, t) \right] \ ,
\end{aligned} \tag{1.23}$$

where we wrote

$$\varepsilon_r(\boldsymbol{r}) E^i(\boldsymbol{r}, t) = E^i(\boldsymbol{r}, t) + \chi_{ij}^{(1)}(\boldsymbol{r}) E^j(\boldsymbol{r}, t) \ . \tag{1.24}$$

Then, we use (1.23) to find the expression for the $i$-th component of the electric field

$$\begin{aligned}
E^i(\boldsymbol{r}, t) = {} & \frac{D^j(\boldsymbol{r}, t)}{\varepsilon_0 \varepsilon_r(\boldsymbol{r})} - \frac{\chi_{ijl}^{(2)}(\boldsymbol{r})}{\varepsilon_r(\boldsymbol{r})} E^j(\boldsymbol{r}, t) E^l(\boldsymbol{r}, t) \\
& - \frac{\chi_{ijlm}^{(3)}(\boldsymbol{r})}{\varepsilon_r(\boldsymbol{r})} E^j(\boldsymbol{r}, t) E^l(\boldsymbol{r}, t) E^m(\boldsymbol{r}, t) \ .
\end{aligned} \tag{1.25}$$

For any other component $E^p(\boldsymbol{r}, t)$, with $p = j, l, m$, we can use the linear relation $E^p(\boldsymbol{r}, t) = D^p(\boldsymbol{r}, t) / (\varepsilon_0 \varepsilon_r(\boldsymbol{r}))$ to write the electric field $E^i(\boldsymbol{r}, t)$ in terms of $\boldsymbol{D}(\boldsymbol{r}, t)$ as

$$E^i(\boldsymbol{r},t) = \frac{D^i(\boldsymbol{r},t)}{\varepsilon_0 \varepsilon_r(\boldsymbol{r})} - \frac{\chi^{(2)}_{ijl}(\boldsymbol{r})}{\varepsilon_0^2 \varepsilon_r^2(\boldsymbol{r})} D^j(\boldsymbol{r},t) D^l(\boldsymbol{r},t)$$
$$- \frac{\chi^{(3)}_{ijlm}(\boldsymbol{r})}{\varepsilon_0^3 \varepsilon_r^3(\boldsymbol{r})} D^j(\boldsymbol{r},t) D^l(\boldsymbol{r},t) D^m(\boldsymbol{r},t) \ , \tag{1.26}$$

and finally

$$E^i(\boldsymbol{r},t) = \frac{1}{\varepsilon_0} \left[ \frac{D^i(\boldsymbol{r},t)}{\varepsilon_r(\boldsymbol{r})} - \Gamma^{(2)}_{ijl}(\boldsymbol{r}) D^j(\boldsymbol{r},t) D^l(\boldsymbol{r},t) \right.$$
$$\left. - \Gamma^{(3)}_{ijlm}(\boldsymbol{r}) D^j(\boldsymbol{r},t) D^l(\boldsymbol{r},t) D^m(\boldsymbol{r},t) \right] \ , \tag{1.27}$$

with

$$\Gamma^{(2)}_{ijl}(\boldsymbol{r}) = \frac{\chi^{(2)}_{ijl}(\boldsymbol{r})}{\varepsilon_0 \varepsilon_r^3(\boldsymbol{r})} \quad \text{and} \quad \Gamma^{(3)}_{ijlm}(\boldsymbol{r}) = \frac{\chi^{(3)}_{ijlm}(\boldsymbol{r})}{\varepsilon_0^2 \varepsilon_r^4(\boldsymbol{r})} \ , \tag{1.28}$$

where we neglected cascaded second-order nonlinear contributions to the third-order nonlinearity. Using (1.27) in eq. (1.5), we find the total Hamiltonian

$$\mathcal{H}(t) = \mathcal{H}_{\mathrm{L}} + \mathcal{H}_{\mathrm{NL}}(t) \ , \tag{1.29}$$

where $\mathcal{H}_{\mathrm{L}}$ is the linear Hamiltonian of equation (1.6) and

$$\mathcal{H}_{\mathrm{NL}} = -\frac{1}{3\varepsilon_0} \int \Gamma^{(2)}_{ijl}(\boldsymbol{r}) D^i(\boldsymbol{r},t) D^j(\boldsymbol{r},t) D^l(\boldsymbol{r},t) d\boldsymbol{r}$$
$$- \frac{1}{4\varepsilon_0} \int \Gamma^{(3)}_{ijlm}(\boldsymbol{r}) D^i(\boldsymbol{r},t) D^j(\boldsymbol{r},t) D^l(\boldsymbol{r},t) D^m(\boldsymbol{r},t) d\boldsymbol{r} \tag{1.30}$$

is the nonlinear part of the full Hamiltonian, fundamental to study nonlinear phenomena. From the nonlinear Hamiltonian (1.30) we can write the state of the generated photons in a channel waveguide due to an exciting pump pulse as the two-mode squeezed vacuum

$$|\psi_{\mathrm{II}}\rangle = e^{\left( \beta C^\dagger_{\mathrm{II}} - H.c. \right)} |\mathrm{vac}\rangle \ , \tag{1.31}$$

where $|\beta|^2$ can be seen as the probability of generating the photon pair and

$$C^\dagger_{\mathrm{II}} = \frac{1}{\sqrt{2}} \int dk_1 dk_2 \phi(k_1, k_2) a^\dagger_{S,k_1} a^\dagger_{I,k_1} \tag{1.32}$$

is an operator, such that $C^\dagger_{\mathrm{II}} |\mathrm{vac}\rangle$ is a normalized two-photon state, where $a^\dagger_{S,k}$ is the signal creation operator and $a^\dagger_{I,k}$ is the idler creation operator, and $\phi(k_1, k_2)$ is the biphoton wavefunction, which is unique for each process. We will work in the limit

of small probability of photon pairs generation, $|\beta|^2 \ll 1$, and thus expand eq. (1.31) in

$$|\psi_{\text{II}}\rangle \approx |\text{vac}\rangle + \beta C_{\text{II}}^{\dagger} |\text{vac}\rangle . \qquad (1.33)$$

The number of generated pairs of a nonlinear process is obtained from the biphoton wavefunction $\phi(k_1, k_2)$: the modulus square of this quantity represents the probability density of generating a pair of photon with wavevectors $k_1$ and $k_2$. Two of the most exploited processes among parametric fluorescence are spontaneous parametric down conversion (SPDC) and spontaneous four-wave mixing (SFWM). These are the two processes that we will investigate in this work.

**1.2.1. SPDC.** Spontaneous parametric down conversion (SPDC), see Fig. 1.3, is a second order nonlinear interaction which involves three photons and can be viewed as the spontaneous decay of one photon at higher energy into two photons at smaller energies. These three photons are historically called pump (the pumping photon), signal and idler (the generated photons). For energy and momentum conservation (also called phase matching condition) to be satisfied, equations

$$\begin{cases} \omega_P = \omega_S + \omega_I \\ \mathbf{k}_P = \mathbf{k}_S + \mathbf{k}_I \end{cases}$$

must hold, where

$$|\mathbf{k}| = \frac{\omega}{c} n_{\text{eff}}(\omega) \qquad (1.34)$$

is the wavevector, with $n_{\text{eff}}(\omega)$ the effective refractive index. The indices $P, S, I$ refer to pump, signal, and idler, respectively, and this notation will be use throughout the work.

The most common material platforms that naturally possess second-order non-linear response are standard III-V semiconductors alloys, such as AlN [5, 6], GaN
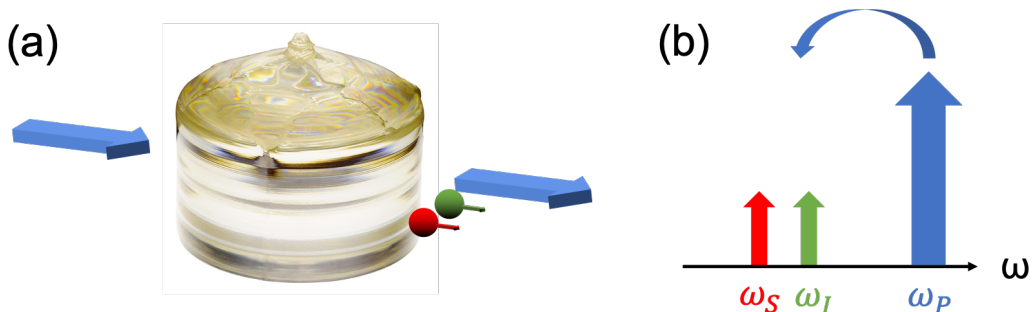


FIGURE 1.3. Schematic representation of (a) SPDC by a $\chi^{(2)}$ medium (e.g. Lithium Niobate) and (b) frequencies involved in the process.

[7], GaAs [8, 9], AlGaAs [10] and GaP [11], thanks to their high $\chi^{(2)}$ tensor components, with typical values ranging from $0.01\,\mathrm{pm/V}$ up to $600\,\mathrm{pm/V}$ [12] and emerging material such as Lithium Niobate (LiNbO$_3$) [13, 14] which possesses both second- and third-order nonlinear responses and is particularly appealing for the integration of optical modulators [15]. Despite their drawbacks, such as fabrication complexity, device capability and cost, a great effort is being put into the development of these platforms.

The goal is to calculate the pair generation and, to do so, we need the expression of the biphoton wavefunction $\phi(k_1, k_2)$ that appears in (1.32). We can calculate it following a backward Heisenberg picture approach [16]. We start from the nonlinear Hamiltonian related to second-order nonlinear interaction

$$\mathcal{H}_{\mathrm{NL}}(t) = -\frac{1}{3\varepsilon_0} \int d\boldsymbol{r}\, \Gamma^{(2)}_{ijl}(\boldsymbol{r}) D^i(\boldsymbol{r}, t) D^j(\boldsymbol{r}, t) D^l(\boldsymbol{r}, t) \tag{1.35}$$

and restrict to the SPDC process considering only terms associated with down conversion of photons, in the framework of the asymptotic field formalism, obtaining

$$\mathcal{H}_{\mathrm{SPDC}}(t) = -\int dk_1\, dk_2\, dk_3\, J(k_1, k_2, k_3) a^\dagger_{S,k_1}(t) a^\dagger_{I,k_2}(t) a_{P,k_3}(t) + \mathrm{H.c.}\ , \tag{1.36}$$

that is the Hamiltonian that will drive the evolution of the asymptotic state, where

$$J(k_1, k_2, k_3) = \frac{1}{\varepsilon_0} \int d\boldsymbol{r}\, \Gamma^{(2)}_{ijl}(\boldsymbol{r}) [D^{\mathrm{out}}_{S,k_1}(\boldsymbol{r})]^* [D^{\mathrm{out}}_{I,k_2}(\boldsymbol{r})]^* D^{\mathrm{in}}_{P,k_3}(\boldsymbol{r}) \tag{1.37}$$

is the overlap integral of the asymptotic fields involved in the process; this quantity depends on the geometry of the structure under consideration. Following this approach, we obtain, from equation (1.32), the expression for the biphoton wavefunction

$$\phi_{\mathrm{SPDC}}(k_1, k_2) = \frac{2\pi\sqrt{2}\alpha}{\beta} \frac{i}{\hbar} \int dk_3\, \phi_P(k_3) J(k_1, k_2, k_3)$$
$$\times\, \delta(\omega_{P,k_3} - \omega_{S,k_1} - \omega_{I,k_2})\ , \tag{1.38}$$

where $|\alpha|^2$ is the expected number of photons in the input pulse and $\phi_P(k)$ is the pulse shape. The Dirac delta function expresses the energy conservation of the process, by setting $\omega_{P,k} = \omega_{S,k_1} + \omega_{I,k_2}$.

We can move from a wavevector notation to a frequency notation defining

$$a_{m,\omega} = \sqrt{\frac{1}{v_{g,m}(\omega)}} a_{m,k} \ , \tag{1.39}$$

$$\phi_P(\omega_3) = \sqrt{\frac{1}{v_{g,P}(\omega_3)}} \phi_P(k_3) \ , \tag{1.40}$$

$$\phi(\omega_1, \omega_2) = \sqrt{\frac{1}{v_{g,S}(\omega_1) v_{g,I}(\omega_2)}} \phi(k_1, k_2) \tag{1.41}$$

where, for every $m = P, S, I$, $v_{g,m}(\omega_3) = \frac{d\omega_m}{dk_m}$ is the group velocity of the mode $m$. The prefactors ensure canonical commutation relations for (1.39) and the proper normalization conditions for (1.40) and (1.41)

$$\int |\phi_P(\omega_3)| \, d\omega_3 = 1 \ , \tag{1.42}$$

$$\int d\omega_1 \int d\omega_2 \, |\phi(\omega_1, \omega_2)| = 1 \ . \tag{1.43}$$

Thus, we obtain for the biphoton wavefunction

$$\begin{aligned}
\phi_{\mathrm{SPDC}}(\omega_1, \omega_2) =& \frac{2\pi\sqrt{2}\alpha}{\beta} \frac{i}{\hbar} \sqrt{\frac{1}{v_{g,S}(\omega_1) v_{g,I}(\omega_2)}} \\
&\times \int d\omega_3 \frac{1}{v_{g,P}(\omega_3)} \phi_P(\omega_3) J(\omega_1, \omega_2, \omega_3) \delta(\omega_3 - \omega_1 - \omega_2) \ ,
\end{aligned} \tag{1.44}$$

where the integral over $\omega_3$ can be solved thanks to the delta function, resulting in

$$\begin{aligned}
\phi_{\mathrm{SPDC}}(\omega_1, \omega_2) =& \frac{2\pi\sqrt{2}\alpha}{\beta} \frac{i}{\hbar} \sqrt{\frac{1}{v_{g,S}(\omega_1) v_{g,I}(\omega_2) v_{g,P}(\omega_1 + \omega_2)}} \\
&\times \phi_P(\omega_1 + \omega_2) J(\omega_1, \omega_2, \omega_1 + \omega_2) \ .
\end{aligned} \tag{1.45}$$

From equation (1.45), applying the normalization condition (1.43), we can calculate the number of pairs generated per pulse $|\beta|^2$ as

$$\begin{aligned}
|\beta_{\mathrm{SPDC}}|^2 =& \frac{8\pi^2 |\alpha|^2}{\hbar^2} \int d\omega_1 d\omega_2 \frac{1}{(v_{g,S}(\omega_1) v_{g,I}(\omega_2) v_{g,P}(\omega_1 + \omega_2))} \\
&\times |\phi_P(\omega_1 + \omega_2)|^2 \, |J(\omega_1, \omega_2, \omega_1 + \omega_2)|^2 \ .
\end{aligned} \tag{1.46}$$

**1.2.2. SFWM.** On the other hand, spontaneous four-wave mixing (SFWM), see Fig. 1.4, is a third order nonlinear process which can be represented as the elastic
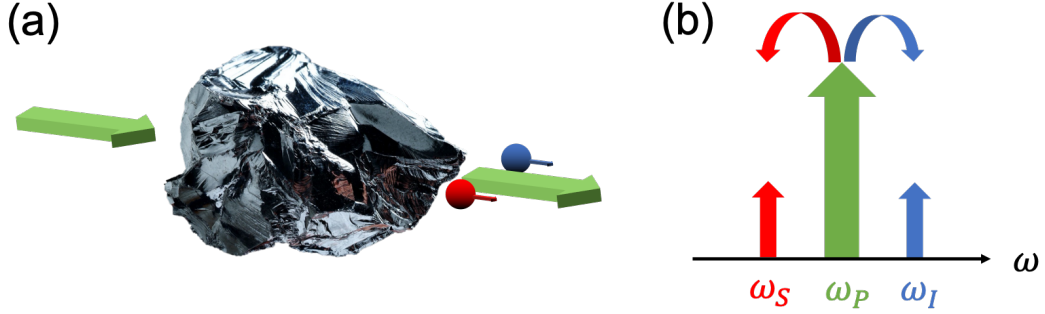
FIGURE 1.4. Schematic representation of (a) SFWM by a $\chi^{(3)}$ medium (e.g. Silicon) and (b) frequencies involved in the process.

scattering between two photons into two other photons at different energies. Here, four photons are involved: two pump photons, one signal and one idler. In both cases energy and momentum conservation must be satisfied; for SFWM it holds

$$\begin{cases} 2\omega_P = \omega_S + \omega_I \\ 2\mathbf{k}_P = \mathbf{k}_S + \mathbf{k}_I \end{cases}, \tag{1.47}$$

with $\mathbf{k}$ defined in (1.34). The platforms commonly employed for third-order nonlinear processes are Silicon [17], Silicon Nitride ($Si_3N_4$) [18], Silica ($SiO_2$) [19], and Hydex [15]. These materials are characterized by high values of $\chi^{(3)}$ components, of the order of $10^2$ pm$^2$/V$^2$ up to $10^5$ pm$^2$/V$^2$ [20], with almost negligible $\chi^{(2)}$, due to their centrosymmetric (invariant to an inversion symmetry transformation) or amorphous structure. However, it is possible to induce effective $\chi^{(2)}$ in silicon photonic materials, for example by symmetry-breaking mediated by an externally applied electric field [21], intrinsic symmetry-breaking at a ($SiO_2$) interface [22], and all-optical poling of ($Si_3N_4$) [23]. The biggest advantage when working with Silicon photonics is the compatibility with the modern complementary-metal-oxide-semiconductor (CMOS) technology, which allows for an easier fabrication process and a dramatic cost reduction.

The nonlinear Hamiltonian to be considered here is

$$\mathcal{H}_{\mathrm{NL}}(t) = -\frac{1}{4\varepsilon_0} \int d\mathbf{r}\, \Gamma^{(3)}_{ijlm}(\mathbf{r}) D^i(\mathbf{r},t) D^j(\mathbf{r},t) D^l(\mathbf{r},t) D^m(\mathbf{r},t) \ , \tag{1.48}$$

that can be rewritten in a form that describes only the four wave mixing process [24], considering only operators that destroy two pump photons and create the signal and idler photons, as

$$\mathcal{H}_{\text{SFWM}}(t) = -\int dk_1\, dk_2\, dk_3\, dk_4\, J(k_1, k_2, k_3, k_4) \times$$
$$a^\dagger_{S,k_1}(t) a^\dagger_{I,k_2}(t) a_{P,k_3}(t) a_{P,k_4}(t) \ , \qquad (1.49)$$

where

$$J(k_1, k_2, k_3, k_4) = \frac{3}{2\varepsilon_0} \int d\mathbf{r}\, \Gamma^{(3)}_{ijlm}(\mathbf{r}) [D^{\text{out}}_{S,k_1}(\mathbf{r})]^* [D^{\text{out}}_{I,k_2}(\mathbf{r})]^* D^{\text{in}}_{P,k_3}(\mathbf{r}) D^{\text{in}}_{P,k_4}(\mathbf{r}).$$
$$(1.50)$$

Following a similar procedure as done for the SPDC case, we obtain for the biphoton wavefunction

$$\phi_{\text{SFWM}}(k_1, k_2) = \frac{2\pi\sqrt{2}\alpha^2}{\beta} \frac{i}{\hbar} \int dk_3\, dk_4\, \phi_P(k_3)\phi_P(k_4) J(k_1, k_2, k_3, k_4)$$
$$\times\, \delta(\omega_{P,k_4} + \omega_{P,k_3} - \omega_{S,k_1} - \omega_{I,k_2}) \ , \qquad (1.51)$$

and, in the angular frequency domain, after computing the integral with the delta function,

$$\phi_{\text{SFWM}}(\omega_1, \omega_2) = \frac{2\pi\sqrt{2}\alpha^2}{\beta} \frac{i}{\hbar} \sqrt{\frac{1}{v_{g,S}(\omega_1)\, v_{g,I}(\omega_2)}} \int d\omega_3\, \phi_P(\omega_1 + \omega_2 - \omega_3)$$
$$\times\, \phi_P(\omega_3) \sqrt{\frac{1}{v_{g,P}(\omega_3) v_{g,P}(\omega_1 + \omega_2 - \omega_3)}} J(\omega_1, \omega_2, \omega_3, \omega_1 + \omega_2 - \omega_3) \ , \quad (1.52)$$

which gives the number of generated pairs per pulse

$$|\beta_{\text{SFWM}}|^2 = \frac{8\pi^2 |\alpha|^2}{\hbar^2} \int d\omega_1\, d\omega_2 \frac{1}{v_{g,S}(\omega_1)\, v_{g,I}(\omega_2)} \left| \int d\omega_3\, \phi_P(\omega_1 + \omega_2 - \omega_3) \right.$$
$$\left. \times\, \phi_P(\omega_3) \sqrt{\frac{1}{v_{g,P}(\omega_3) v_{g,P}(\omega_1 + \omega_2 - \omega_3)}} J(\omega_1, \omega_2, \omega_3, \omega_1 + \omega_2 - \omega_3) \right|^2 .$$
$$(1.53)$$

In order to practically calculate the number of generated pairs, we have to dive into the overlap integral expressions (1.37) and (1.50) which contain the field involved in the processes. These fields strongly depend on the framework in which one is studying the nonlinear phenomena. As a matter of fact, due to the nonlinear nature itself, the generation of photon pairs in bulk systems is quite low. We can try to give an estimate of such a generation efficiency using a simplified expression for the generated photon power [25], in this case the idler,

$$P_I = \frac{\hbar \omega_P}{\mathcal{T}} \left( \gamma_{\mathrm{NL}} P_P L \right)^2 \;, \tag{1.54}$$

with $\gamma_{\mathrm{NL}}$ the nonlinear power factor, defined as

$$\gamma_{\mathrm{NL}} = \frac{n_2 \omega_P}{c A_{\mathrm{eff}}} \;, \tag{1.55}$$

where $P_P$ is the pump power, $L$ is the length of the sample, $A_{\mathrm{eff}}$ is the effective area, which can be thought as the focusing area, $n_2$ is the nonlinear refractive index of the material and $\mathcal{T}$ is the generation bandwidth time, defined as

$$\mathcal{T} = \frac{2\pi}{\displaystyle\int_0^{\omega_P} \left[ 1 - \left( \frac{\Omega}{\omega_P} \right)^2 \right] \mathrm{sinc}^2(\Delta k \frac{L}{2}) \, d\Omega} \;, \tag{1.56}$$

where $\Omega = \omega - \omega_P$ indicates positive detuning from the pump and $\Delta k = 2\mathbf{k}_P(\omega_P) - \mathbf{k}_S(\omega_P - \Omega) + \mathbf{k}_I(\omega_P + \Omega)$ represents the phase matching condition. If we assume $\Delta k = 0$ over the entire bandwidth,

$$\mathcal{T} \approx \frac{2\pi}{\displaystyle\int_0^{\omega_P} \left[ 1 - \left( \frac{\Omega}{\omega_P} \right)^2 \right] d\Omega} = \frac{2\pi}{\left[ \Omega - \frac{\Omega^3}{3\omega_P^2} \right]_0^{\omega_P}} = \frac{3\pi}{\omega_P} \;, \tag{1.57}$$

giving

$$P_I = \frac{\hbar \omega_P^4}{3\pi} \left( \frac{n_2 P_P L}{c A_{\mathrm{eff}}} \right)^2 \;. \tag{1.58}$$

We are overestimating this result by neglecting any diffraction and assuming the focusing area constant over the entire sample. Thus, if we assume a pump power $P_P = 1\,\mathrm{mW}$ at $\omega_P = 1215\,\mathrm{rad/ps}$ (1550 nm), a length $L = 1\,\mathrm{cm}$, an area $A_{\mathrm{eff}} = 100\,\mu\mathrm{m}^2$, and a nonlinear refractive index for Silicon $n_2(@1550\,\mathrm{nm}) = 5.59 \times 10^{-18}\,\mathrm{m}^2/\mathrm{W}$, we get a generated power of $P_I = 8 \times 10^{-15}\,\mathrm{W}$, that makes this process almost impossible to detect. It is clear that we need a strategy to increase the generation. Looking at equation (1.58), one solution could be to take advantage of the interaction length, by considering a very large $L$. This is the case of nonlinear phenomena in an optical fiber, where light is guided for kilometers. Another solution could be to reduce the effective area $A_{\mathrm{eff}}$ of the process, connected to the nonlinear coefficient $\gamma_{\mathrm{NL}}$ in (1.55). This can be achieved by confining light in an integrated waveguide, which can be characterized by an effective area of the orders of $10^{-2}\,\mu\mathrm{m}$. In this case, given the increase of four orders of magnitude of $\gamma_{\mathrm{NL}}$, the generated power would increase of eight orders of

magnitude. Integrated circuits are thus the best way to exploit nonlinear phenomena, since they allow for tighter modal confinement and better modal overlap, leading to higher conversion efficiency [25]. To increase the interaction, one can also benefit from temporal confinement; this is the case of a resonator, where light is confined in a small volume for a long time. From the simple ring resonator to more complex structures, resonators offer both spatial and temporal confinement as well as a well-defined set of resonances that can be exploited in the parametric processes. Furthermore, having the photon source directly on an integrated chip is desirable for an efficient use in quantum-information processing [26]. In this work we will show how resonators can be employed to generate states of light.

### 1.3. Main features of a ring resonators

The simplest resonator we can design is a ring resonator, like the one shown in Fig. 1.2(b), that can be realized by bending a ridge waveguide on itself. Due to the circular symmetry, the ring presents a set of resonances (modes) (see Fig. 1.6 and 1.7) at the frequencies that satisfy the phase condition

$$\delta = kL = m2\pi \ , \tag{1.59}$$

with $m$ integer and $L$ the length of the ring.

We considered chromatic dispersion (1.34), thus, if the frequency range is sharp enough around a reference frequency $\omega_0$, we can expand the real part of the wavevector (1.19)-(1.20) in Taylor series around that frequency

$$k(\omega) = k_0 + \frac{1}{v_g}(\omega - \omega_0) + \frac{1}{2}\beta_2(\omega - \omega_0)^2, \tag{1.60}$$

where $k_0 = \omega_0/c\, n_{\text{eff}}$, $n_{\text{eff}}$ is the effective index at $\omega_0$, $v_g = [d\omega/dk]_{\omega_0} = c/n_g$ the group velocity, $n_g$ is the group index, and $\beta_2 = [d^2k/d\omega^2]_{\omega_0}$ the group velocity dispersion (GVD). From this, we can calculate the free spectral range (FSR$_\omega$), which is the spectral distance between two consecutive resonance peaks $\omega_{m+1} - \omega_m$. If we consider (1.59) with (1.60), by neglecting the GVD, we can write

$$\begin{cases} k_0 L + \frac{L}{v_g}(\omega_{m+1} - \omega_0) = (m+1)2\pi \\ k_0 L + \frac{L}{v_g}(\omega_m - \omega_0) = m2\pi \end{cases}, \tag{1.61}$$

and subtract the two equations, obtaining

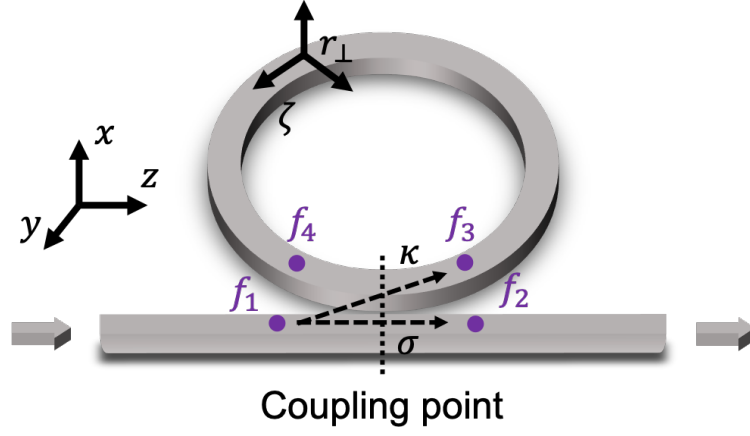$$\text{FSR}_\omega = 2\pi\frac{v_g}{L} \ . \tag{1.62}$$

FIGURE 1.5. Schematic representation of the coupling between a bus waveguide and a ring resonator, showing the self-coupling and cross-coupling coefficients of the point coupler and the involved fields amplitude.

The coupling between the waveguide and the ring can be modelled by a scattering matrix, assuming light coming from the left in the bus waveguide, that links the incoming fields to the coupling point ($f_1$ and $f_4$) with outgoing fields ($f_2$ and $f_3$) through the self-coupling $\sigma$ and cross-coupling $\kappa$ coefficients of the coupler (Fig. 1.5), as

$$\begin{pmatrix} f_2 \\ f_3 \end{pmatrix} = X \begin{pmatrix} f_1 \\ f_4 \end{pmatrix} \tag{1.63}$$

where $X$ is the scattering matrix that can be written as

$$X = \begin{pmatrix} \sigma & i\kappa \\ i\kappa & \sigma \end{pmatrix} \tag{1.64}$$

with the the coupler is assumed lossless with $(\sigma, \kappa) \in [0, 1]$ and hence yielding $\sigma^2 + \kappa^2 = 1$ [12, 27]. We can write the expression for

$$f_4 = f_3 e^{i\tilde{k}L} = f_3 a e^{i\delta} , \tag{1.65}$$

where $1 - a = 1 - e^{-\xi L}$ is the round-trip loss and $\delta = kL$ is the phase acquired in a round-trip, and obtain the system associated to (1.63)

$$\begin{cases} f_2 = \sigma f_1 + i\kappa f_4 \\ f_3 = i\kappa f_1 + \sigma f_4 \\ f_4 = f_3 a e^{i\delta} . \end{cases} \tag{1.66}$$

From this system we can obtain the complex transmission coefficient

$$t = \frac{f_2}{f_1} = \frac{\sigma - ae^{i\delta}}{1 - \sigma ae^{i\delta}} \; .$$
(1.67)

In Fig. 1.6(a) we plot the transmittance $T = |t|^2$ as a function of $k$. It is straightforward to see that if there are no scattering losses ($\xi = 0$) the transmittance is $T = 1$, thus the ring is behaving like an all-pass filter; instead, if $a = \sigma$, at the resonance condition the transmission drops to zero (Fig. 1.6(b)). This last regime is called critical coupling, when all the energy flowing from the waveguide into the resonator does not couple out anymore.

From (1.66) we can also calculate the field enhancement of the ring resonator

$$\text{FE} = \frac{f_4}{f_1} = \frac{i\kappa}{1 - \sigma ae^{i\delta}} \; ,$$
(1.68)

which corresponds to the intensity enhancement

$$|\text{FE}|^2 = \frac{\kappa^2}{1 + \sigma^2 a^2 - 2\sigma a \cos(\delta)} \; .$$
(1.69)

This quantity is plotted in Fig. 1.7(a) as a function of the angular frequency. If we neglect the GVD in the $\delta$ expansion around the resonance frequency $\omega_m$, we can write

$$\cos\left(k(\omega)L\right) \approx \cos\left(k(\omega_m)L + \frac{L}{v_g}(\omega - \omega_m)\right) = 1 - \frac{1}{2}\left(\frac{L}{v_g}\right)^2 (\omega - \omega_m)^2 \; ,$$
(1.70)

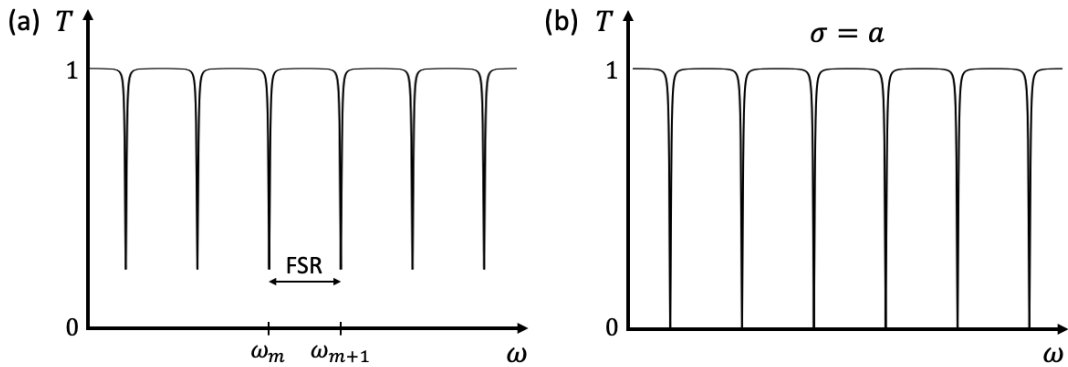since $k(\omega_0)L = m2\pi$, that leads to the expression



FIGURE 1.6. Transmission dips of a ring resonator: (a) the spectral distance between two consecutive resonances is the FSR; (b) at the critical coupling condition ($\sigma = a$) the on-resonance transmission drops to zero.
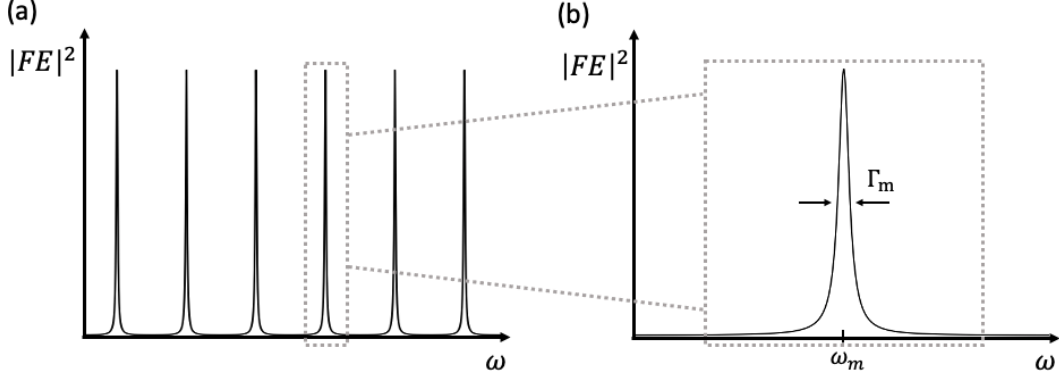
FIGURE 1.7. Intensity enhancement of a ring resonator: (a) comb of equally-spaced resonances and (b) zoom on a single Lorentzian-shaped resonance.

$$|\text{FE}_m(\omega)|^2 = \frac{\kappa^2}{1 + \sigma^2 a^2 - 2\sigma a + \sigma a \left(\frac{L}{v_g}\right)^2 (\omega - \omega_m)^2} =$$

$$\frac{1 - \sigma^2}{(1 - \sigma a)^2 + \sigma a (\frac{L}{v_g})^2 (\omega - \omega_m)^2} \ . \tag{1.71}$$

The maximum of the intensity is reached on resonance, when $\omega = \omega_m$, becoming

$$|\text{FE}_{(max)}|^2 = \frac{1 - \sigma^2}{(1 - \sigma a)^2} \ . \tag{1.72}$$

From this, we can calculate the full width at half maximum (FWHM) $\Gamma_m$ of the $m$-th resonance by setting $|\text{FE}_m(\omega)|^2 = |\text{FE}_{(max)}|^2/2$ at $(\omega - \omega_m) = \Gamma_m/2$, giving

$$\left|\text{FE}_m(\omega_m + \frac{\Gamma_m}{2})\right|^2 = \frac{1 - \sigma^2}{(1 - \sigma a)^2 + \sigma a (\frac{L}{v_g})^2 (\frac{\Gamma_m}{2})^2} = \frac{1 - \sigma^2}{2(1 - \sigma a)^2} \ , \tag{1.73}$$

which results in

$$\Gamma_m = \frac{2(1 - \sigma a)v_g}{\sqrt{\sigma a}L} \ . \tag{1.74}$$

We notice that we can write equation (1.71) as

$$|\text{FE}_m(\omega)|^2 = |\text{FE}_{(max)}|^2 \frac{\frac{\Gamma_m^2}{4}}{\frac{\Gamma_m^2}{4} + (\omega - \omega_m)^2} \ , \tag{1.75}$$

with $|\text{FE}_{(max)}|^2$ given by (1.72), which tells us that the resonances in Fig.1.7 follow a Lorentzian shape (Fig. 1.7(b)).

Equation (1.74) allows us to write the expression for the quality factor $Q$ of the ring resonator, that represents the number of cycles the light travels in the ring before the energy is reduced by a factor $1/e$. It gives an estimate of how long energy flows inside the ring before being coupled out or lost. Therefore, we can consider an *intrinsic* quality factor $Q_I$ that depends only on the losses inside the ring, and a *coupling* quality factor $Q_C$ that takes into account exclusively the energy loss due to the coupling with the bus waveguide. The total quality factor, called *loaded* quality factor $Q_L$, is then

$$\frac{1}{Q_L} = \frac{1}{Q_I} + \frac{1}{Q_C} \ , \tag{1.76}$$

and it is defined by

$$Q_L = \frac{\omega_m}{\Gamma_m} = \frac{\sqrt{\sigma a} L \omega_m}{2(1 - \sigma a) v_g} \ , \tag{1.77}$$

where $\omega_m$ and $\Gamma_m$ are quantities that can be easily extracted from a transmission spectrum.

An important parameter for a resonator is the *finesse* $\mathcal{F}$. This quantity is defined as

$$\mathcal{F} = \frac{2\pi \text{FSR}}{\Gamma_m} = \frac{\pi \sqrt{\sigma a}}{(1 - \sigma a)} \ , \tag{1.78}$$

and links the width of a resonance with its distance from the subsequent one. We can study the system in the high-finesse regime, $\sigma a \approx 1$, and try to link this quantity with the maximum intensity enhancement (1.72). First, we consider the case of negligible losses $(a = 1)$ and write

$$\mathcal{F} \approx \frac{\pi}{1 - \sigma} \ , \tag{1.79}$$

$$|\text{FE}_{(\text{max})}|^2 \approx \frac{1 + \sigma}{1 - \sigma} \approx \frac{2}{1 - \sigma} \ , \tag{1.80}$$

and by comparing these two equations we get

$$|\text{FE}_{(\text{max})}|^2 \simeq \frac{2}{\pi} \mathcal{F} \ . \tag{1.81}$$

Instead, if we consider the critical coupling regime $(\sigma = a)$, we can write

$$\mathcal{F} \approx \frac{\pi}{1 - \sigma^2} \ , \tag{1.82}$$

$$|\text{FE}_{(\text{max})}|^2 \approx \frac{1 - \sigma^2}{(1 - \sigma^2)^2} \approx \frac{1}{1 - \sigma^2} \ , \tag{1.83}$$

and thus get

$$|\text{FE}_{(\text{max})}|^2 \simeq \frac{1}{\pi}\mathcal{F} \; . \tag{1.84}$$

The finesse is a significant parameter of a ring resonator because from a very simple measurement of the FSR and of the FWHM it is possible to acquire information about the field enhancement, a far more hidden quantity that cannot be measured directly in an experiment. Among integrated sources, ring resonators have been widely used, for they are compatible with open-fab industrial production, they have a small footprint, they can provide high generation rates thanks to large field enhancements and they are naturally characterized by a resonance comb, which can be exploited to guarantee energy conservation in resonant parametric processes [28–30]. Ring resonators applications vary from signal processing to optical sensing [31]. These resonators are excellent for on-chip integrated optics [32] and are already used in commercial devices [17, 18].

The simplicity of ring resonators is one of their biggest advantage, but also one of their limits. Despite the numerous properties that we mentioned before, there are some issues that sometimes cannot be overcome. For example, so far we neglected dispersion effect by assuming null GVD, though, it is necessary to understand what effect might be produced. If $\beta_2 > 0$ we are in the so-called normal dispersion regime, while if $\beta_2 < 0$ we are in the regime of anomalous dispersion. The effect of such dispersion is sketched in Fig. 1.8 and it causes an uneven shift of the resonances at different frequencies. It is clear that if we seek for equally-spaced resonances to satisfy energy conservation, GVD can deteriorate the nonlinear process. We can try to compensate for this effect with dispersion engineering by adjusting the geometry of the waveguide, but the tunability is limited.
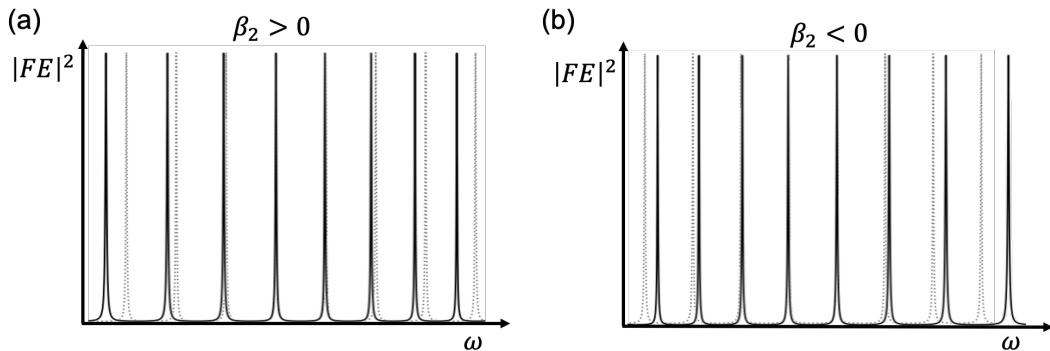


FIGURE 1.8. (a) Normal and (b) anomalous dispersion regimes. The spectra affected by the GVD (solid black lines) are compared with those where $\beta_2 = 0$ (dashed grey lines). The effect is exaggerated.
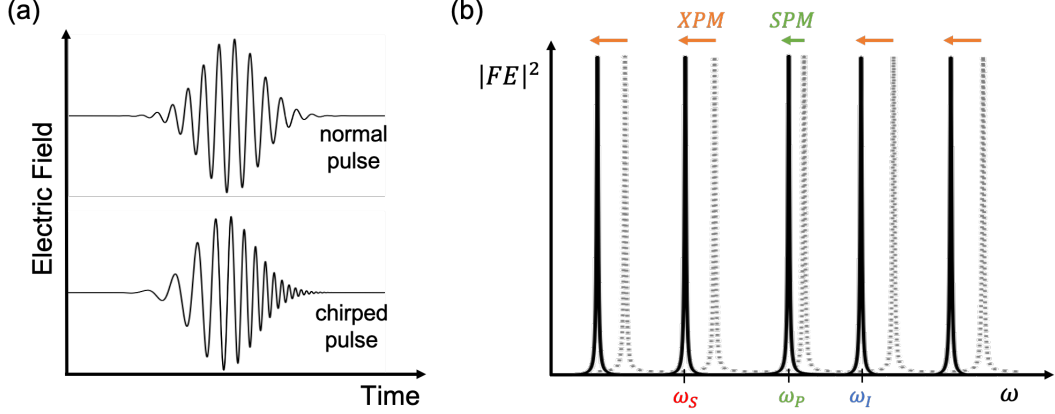
FIGURE 1.9. (a) Kerr effect on a temporal pulse; the result is the so-called chirped pulse. (b) Effect of SPM and XPM on the resonances of a ring. SPM acts only on the pump resonance, resulting in a smaller detuning with respect to the other resonances.

Another problem may arise from the power injected in the system. If it's high enough, the nonlinear Kerr effect, related to the third order nonlinearity, starts to play, modifying the refractive index differently for different resonances (Fig 1.9(a)). In particular, the effect of self-phase modulation (SPM) and cross-phase modulation (XPM)[33] detunes the pump resonance with respect to the other resonances, preventing the energy matching condition (Fig 1.9(b)). This means that, when employing a standard ring resonator, one should design the system taking into account the power at which it will eventually work, for example working in an anomalous dispersion regime to compensate Kerr effect at the target power.

**1.3.1. Dispersion tolerance in a ring resonator.** In a ring resonator, where dispersion engineering is limited, we must consider a trade-off between the quality factor of the resonator, which determines the linewidth of the resonances, and the generation bandwidth, for spectrally distant resonances will more likely fall out of phase matching.

Lets consider SP-SFWM as an example. The phase mismatch, due to dispersion, is $\Delta k_{\mathrm{disp}} = k(\omega_I) + k(\omega_S) - 2k(\omega_P)$. Since we consider an expansion of the wavevector up to the second order (1.60), we get $\Delta k_{\mathrm{disp}} = \beta_2(\omega_I - \omega_P)^2$, where we used $\omega_I + \omega_S = 2\omega_P$. From this value we can define a coherence length

$$L_{\mathrm{coh}} = \frac{\pi}{\Delta k_{\mathrm{disp}}} = \frac{\pi}{\beta_2 \Omega_{\mathrm{gen}}^2} \ , \tag{1.85}$$

where

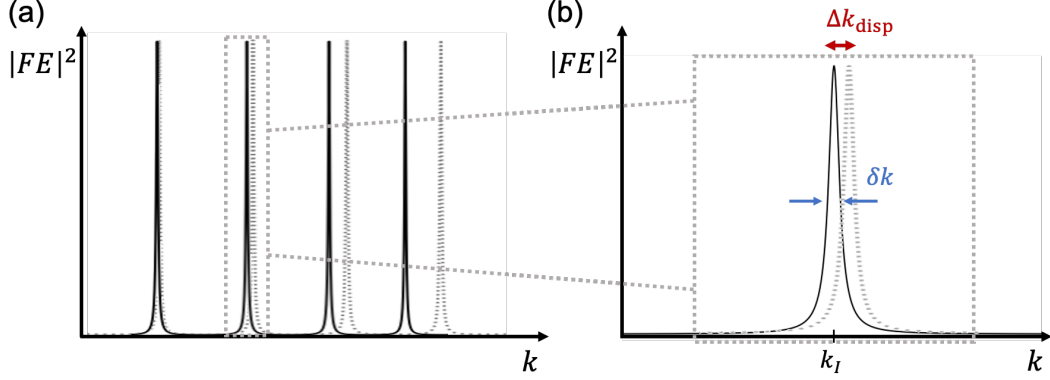$$\Omega_{\mathrm{gen}} = \omega_I - \omega_P > 0 \tag{1.86}$$

FIGURE 1.10. (a) Ring resonator spectrum affected by normal dispersion (the effect is exaggerated). (b) Tolerance between the wavevector HWHM $\delta k/2$ and the phase mismatch due to dispersion $\Delta k_{\mathrm{disp}}$.

is the generation bandwidth, that is the maximum spectral distance between idler (or signal) photon where the phase matching condition is satisfied. The phase mismatch must be

$$\Delta k_{\mathrm{disp}} < \frac{\delta k}{2} \ , \tag{1.87}$$

where $\delta k = \Gamma_I/(v_g)$ is the wavenumber FWHM of the resonance (see Fig. 1.10).

From (1.85) we can calculate the condition the coherence length must follow to get an efficient conversion process

$$L_{\mathrm{coh}} > \frac{2\pi}{\delta k} = \frac{2\pi v_g}{\omega_I} Q_I = 2\pi v_g \tau_{\mathrm{dwell}} \ , \tag{1.88}$$

where we stood out the dependence on the quality factor $Q_I$ and on the dwelling time $\tau_{\mathrm{dwell}}$, i.e. the mean time a photon spends inside the resonator before exiting, of the resonator. As we can expect, the higher the quality factor, and thus the higher the dwelling time, the higher must be the coherence length. We can also rewrite equation (1.88) using (1.85) to highlight the condition over the bandwidth $\Omega_{\mathrm{gen}}$ as

$$\Omega_{\mathrm{gen}}^2 < \frac{\Gamma_I}{2v_g\beta_2} = \frac{\omega_I}{2v_g\beta_2 Q_I} \ . \tag{1.89}$$

| @ 1550 nm | $v_g$ ($\mu$m/ps) | $\beta_2$ (ps$^2$/$\mu$m) | $Q_I$ | $\Omega_{\mathrm{gen}}$ (rad/ps) |
|---|---|---|---|---|
| Si | $\approx 100$ | $\approx 1 \times 10^{-8}$ | $\approx 10^5$ | $\approx 80$ |
| Si$_3$N$_4$ | $\approx 150$ | $\approx 1 \times 10^{-7}$ | $\approx 10^5$ | $\approx 20$ |
| LiNbO$_3$ | $\approx 120$ | $\approx 1 \times 10^{-8}$ | $\approx 10^5$ | $\approx 70$ |

TABLE 1.1. Generation bandwidth $\Omega_{\mathrm{gen}}$ comparison and typical group velocities $v_g$, GVDs $\beta_2$ and quality factors $Q_I$ values of most common platforms, at telecom wavelength $\lambda = 1550$ nm.

In table 1.1 we show some value of the generation bandwidth for typical quantities of the most common platforms, at the fixed angular frequency $\omega_I = 1215 \, \mathrm{rad/ps}$ (1550 nm).

In conclusion, ring resonators are the best way to exploit nonlinear processes in integrated structures, but within certain limitations. Some unwanted effects can be detrimental for the desired process and thus require a different approach. This is the focus of our work, where we study solutions to engineer the resonances to overcome these problems. The idea is to take advantage of the interaction between two different resonators that share a common spatial region.

## 1.4. Towards practical implementation

Ring resonators are practical and efficient platforms, but their simplicity may lead to some limitations. One example can be the coupling of the light from an external bus waveguide into the resonator. In fact, we modelled the coupling through a point coupler where light transfer happens, by definition, in a point. This sometimes isn't a good approximation, for the coupling of well confined modes can take place only over a finite distance. In fact, due to the limited fabrication resolution, the waveguide and the ring could not be closer than a few hundreds of nanometers. The natural solution is to move from a ring resonator to a racetrack resonator, as the one sketched in Fig. 1.11, where the coupling with an external waveguide can easily happen along the straight part of the resonator. The coupling region of length $L_{\mathrm{cp}}$ can be treated as a coupler with effective coefficients $\sigma$ and $\kappa$.

However, this solution does not solve another limitation that we may encounter when dealing with integrated structure, that is the increase of the losses in the transition from a straight waveguide to a bent region of a resonator. There, the mode profile is modified as it experiences a centrifugal-like force, see Fig. 1.12, that moves
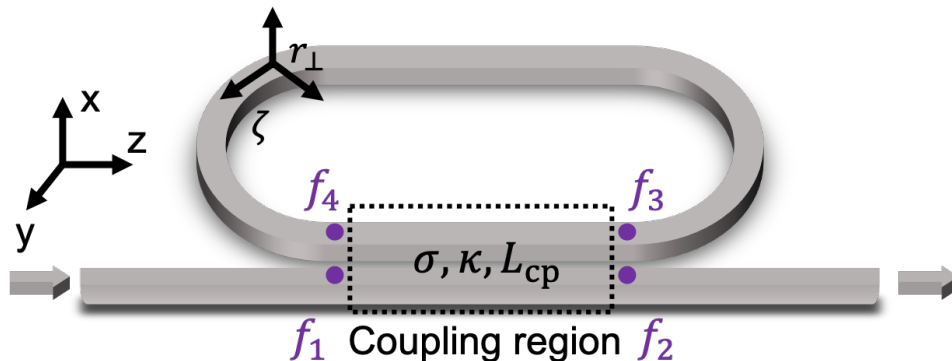


FIGURE 1.11. Sketch of a racetrack resonator and representation of the coupling with the bus waveguide through a finite-length coupler.
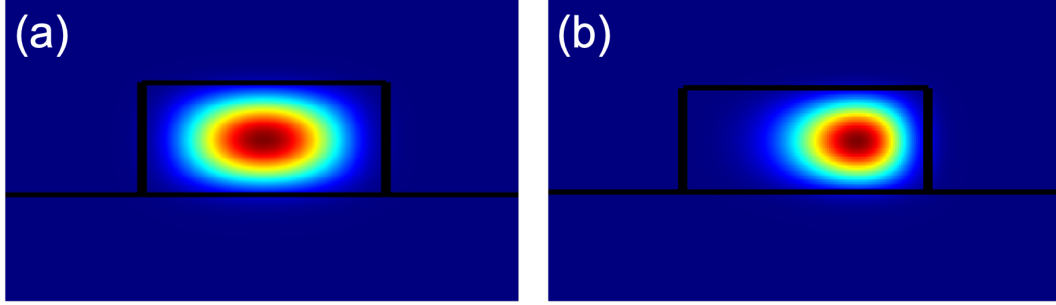
FIGURE 1.12. Simulated mode profile [34] of a field propagating (a) in a straight waveguide and (b) in a bent waveguide.

the mode towards the edge of the waveguide. This abrupt change in the mode profile may lead to intermodal coupling, especially in the case of a multimode waveguide, that can be detrimental for high quality factor resonators. We addressed this problem by studying the Bezier curve [35], a particular kind of bend than allows for a gentler transition from the straight arm to the bend with respect to a standard circumference arc, thanks to a variable curvature radius. A cubic Bezier curve is defined by the parametric equation

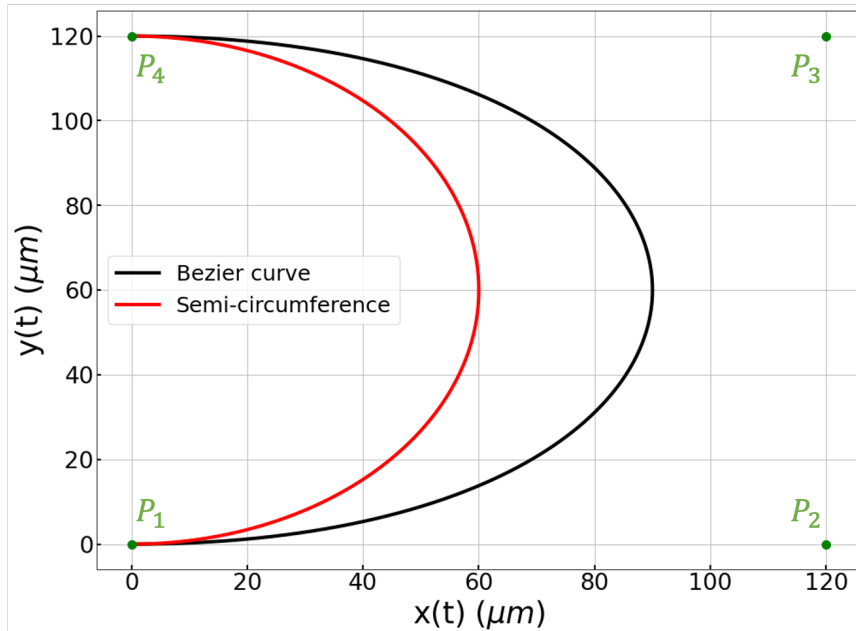$$B(t) = (1-t)^3 P_1 + 3t(1-t)^2 P_2 + 3t^2(1-t)P_3 + t^3 P_4 \,, \tag{1.90}$$



FIGURE 1.13. Comparison between a standard semi-circumference of radius $R = 60 \,\mu$m and a cubic Bezier curve define by the control points $P_1 = (0,0)$, $P_2 = (2R,0)$, $P_3 = (2R,2R)$, and $P_4 = (0,2R)$.

where $t \in [0, 1]$ is the curve parameter and $P_1$, $P_2$, $P_3$, and $P_4$ are the control points. In Fig. 1.13 we compare the Bezier curve (black line), defined by four points at the vertices of a square, with a standard semi-circumference (red line). We can see that in points $P_1$ and $P_4$ the curvature radius is larger with respect to that of the semi-circumference, allowing for a smooth transition. In particular, this Bezier curve is designed such that the curvature radius in points $P_1$ and $P_4$ tends to infinity and decreases until the minimum value of $R_{\min} \approx 0.75R$ where the tangent to the curve is vertical. In the example in Fig. 1.13 we have $R = 60 \, \mu\text{m}$ and $R_{\min} \approx 45 \, \mu\text{m}$. We stress that $R_{\min}$ is smaller than the radius $R$ of the simple circumference, thus, when designing such a structure, this feature has to be considered. One can avoid this issue by designing a more complex curve, composed of different Bezier arcs, but we did not address this problem in this work.

If we consider the coupler we discussed for the racetrack resonator with circular curves, usually the coupling ($\kappa$) is taken to be zero in the bent region. Instead, when designing the Bezier curve we have to consider a non-zero coupling that decreases with the increasing of the banding radius. We studied a model, sketched in Fig. 1.14, to simulate such a coupling, by dividing the Bezier curve in $N$ short segments and considering $N$ short directional couplers (DCs) with different gaps $g_i$, and thus different coupling constants $\kappa_i$, from the minimum value of the actual DC gap $g_{\text{DC}}$ up to the maximum gap $g_{\max}$ after which the coupling can be considered negligible. The relevant features of the Bezier arc that contributes to the coupling are shown in Fig. 1.15, where we represent the geometry of the arc, with its $x$- and $y$-span (panel (a)) and the value of the gap as a function of the $x$ coordinate (panel (b)).

The general properties of a DC will be detailed in chapter 3, since for this model we only need to associate to each coupler a scattering matrix $S_i$ defined as

$$S_i = \begin{bmatrix} \cos(\kappa_i L_i) & -i\sin(\kappa_i L_i) \\ -i\sin(\kappa_i L_i) & \cos(\kappa_i L_i) \end{bmatrix} , \tag{1.91}$$
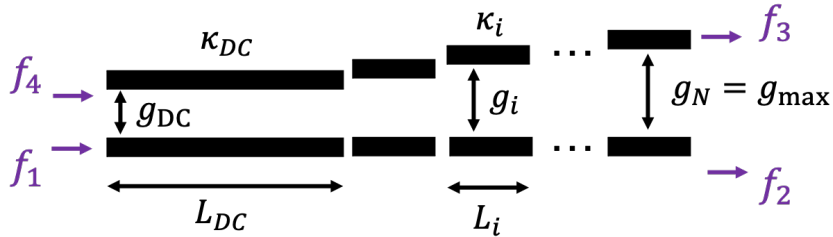


FIGURE 1.14. Sketch of the model for the effective coupling between two Bezier curves. The arcs are divided in $N$ segments each of length $L_i$ and gap $g_i$ from the minimum value $g_{\text{DC}}$ to the maximum value of $g_{\max}$.
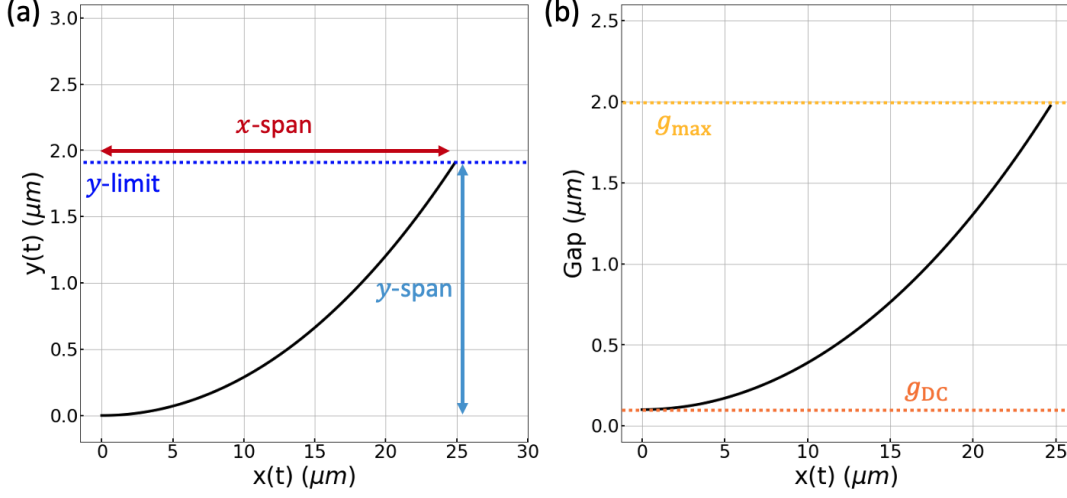
FIGURE 1.15. (a) Bezier arc $x$-span $= 24.9\,\mu$m and $y$-span $= 1.9\,\mu$m, determined by setting $y$-limit $= g_{\max} - g_{\mathrm{DC}}$, where the maximum gap is $g_{\max} = 2\,\mu$m and the minimum gap is $g_{\mathrm{DC}} = 0.1\,\mu$m. (b) Plot of the gap between the waveguides for increasing $x$ coordinate.

where $L_i$ is the length of the $i^{th}$ coupler, determined by dividing the $x$-span of the Bezier arc by the number of couplers $N$; hence, in this model all the $L_i$ are the same, but the theory can be generalized by assuming different values for each DC, as long as their sum equals the total $x$-span of the arc. The larger the number $N$, the more accurate is the model, up to a value where it reaches convergence. The total scattering matrix, that connects in and out fields as

$$\begin{bmatrix} f_2 \\ f_3 \end{bmatrix} = S_{\mathrm{tot}} \begin{bmatrix} f_1 \\ f_4 \end{bmatrix} \ , \tag{1.92}$$

is given by

$$S_{\mathrm{tot}} = S_N \cdot S_{N-1} \cdots S_1 \cdot S_{\mathrm{DC}} \ , \tag{1.93}$$

where

$$S_{\mathrm{DC}} = \begin{bmatrix} \cos(\kappa_{\mathrm{DC}} L_{\mathrm{DC}}) & -i\sin(\kappa_{\mathrm{DC}} L_{\mathrm{DC}}) \\ -i\sin(\kappa_{\mathrm{DC}} L_{\mathrm{DC}}) & \cos(\kappa_{\mathrm{DC}} L_{\mathrm{DC}}) \end{bmatrix} \tag{1.94}$$

is the scattering matrix describing the usual directional coupler with gap $g_{\mathrm{DC}}$, coupling $\kappa_{\mathrm{DC}}$, and length $L_{\mathrm{DC}}$. Finally, in Fig. 1.16 we compare the effective coupling $\kappa_{\mathrm{eff}}$ calculated from the total matrix (1.93) model including the Bezier curve contribution (black solid line) with that of the sole DC when the circumference arc is used (dashed red line), for different lengths of the DC. At $L_{\mathrm{DC}} = 0$ is visible the contribution to the coupling with the bus waveguide given by the sole Bezier arc.

We studied this model for a more practical implementation of an integrated platform because the focus of our work is how to take advantage of the coupling between
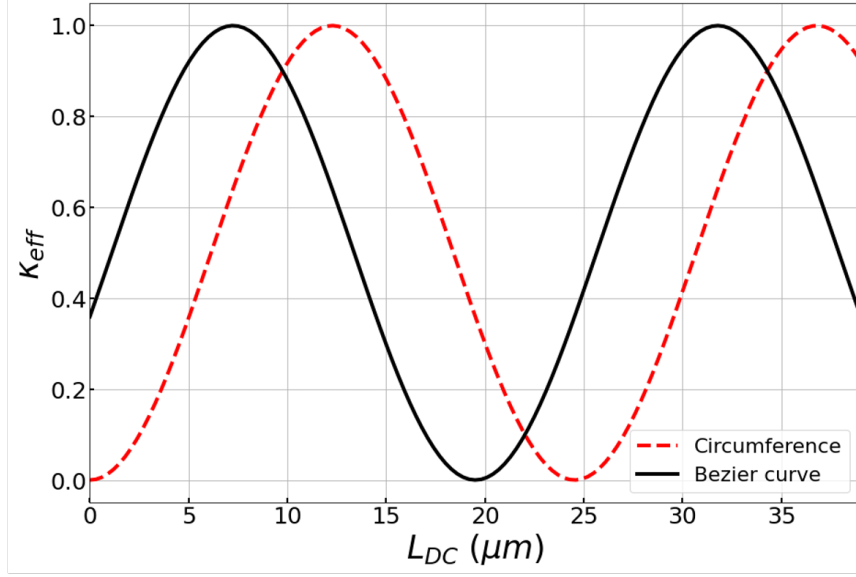
FIGURE 1.16. Comparison between the effective coupling modelled with the Bezier curve (black solid line) and that with a standard circumference arc (dashed red line) as a function of the DC length. The difference between the two plots at $L_{\mathrm{DC}} = 0$ is the contribution to the effective coupling from the Bezier arc.

two resonators, and so we need to gain a deep knowledge of the limitations that one can encounter and the technique that can be applied to overcome them to best exploit the possible configurations.

## 1.5. Linear and nonlinear coupling of two resonators

We are interested in the effect of the interaction of two resonators on their resonance combs. Let's consider two ring resonators of length $L_1$ and $L_2$ placed close to each other, coupled by a point coupler with coupling coefficient $\kappa$, as shown in Fig. 1.17(a). We want to study how the position of their resonances changes depending on the coupling between them. We assume no scattering nor coupling losses. We can identify four fields around the coupler that are connected by the linear system

$$\begin{cases} f_1 = f_2\sqrt{(1-\kappa^2)} + i\kappa f_3 \\ f_2 = f_1 e^{ik(\omega)L_1} \\ f_3 = f_4 e^{ik(\omega)L_2} \\ f_4 = i\kappa f_2 + \sqrt{(1-\kappa^2)}f_3 \end{cases} , \tag{1.95}$$

that can be solved algebraically by finding the solution to

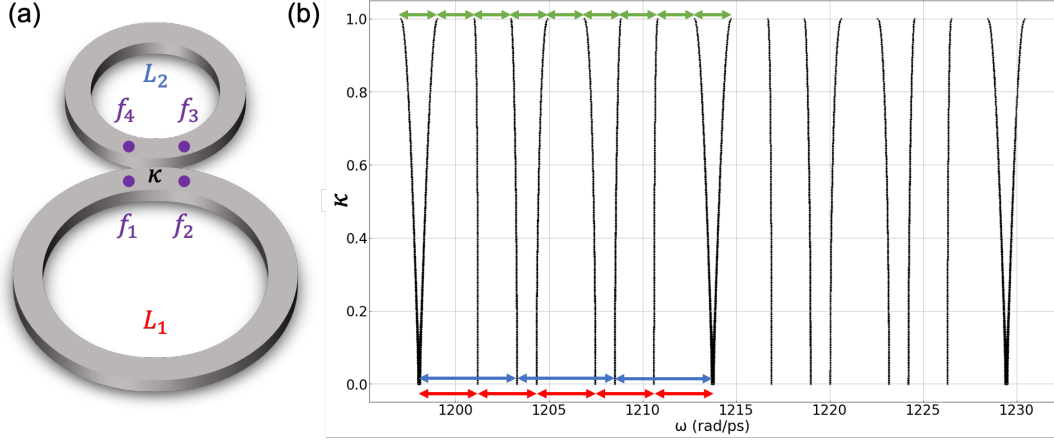$$\mathcal{M}(\omega)\mathbf{f} = \mathbf{0} , \tag{1.96}$$

FIGURE 1.17. (a) Sketch of the system composed of two coupled ring resonators, with $L_1 = 500\,\mu$m and $L_2 = 300\,\mu$m, respectively, and fields around the coupler. (b) Resonances position for different values of the coupling coefficient $\kappa$. When the coupling is zero, two combs of resonances are visible, with $FSR_1$ and $FSR_2$ indicated by red and blue arrows, respectively. When $\kappa = 1$, only one set of resonances is present, with its FSR (green arrows).

where

$$\mathcal{M}(\omega) = \begin{bmatrix} 1 & -\sqrt{(1-\kappa^2)} & -i\kappa & 0 \\ -e^{ik(\omega)L_1} & 1 & 0 & 0 \\ 0 & 0 & 1 & -e^{ik(\omega)L_2} \\ 0 & -i\kappa & -\sqrt{(1-\kappa^2)} & 1 \end{bmatrix} , \tag{1.97}$$

and

$$\mathbf{f} = \begin{bmatrix} f_1 \\ f_2 \\ f_3 \\ f_4 \end{bmatrix} . \tag{1.98}$$

The problem has a non-trivial solution if the determinant of the matrix is zero (Rouché-Capelli theorem). We then look for the solutions of the problem

$$\mathrm{Det}(\omega) = \det |\mathcal{M}(\omega)| = 0 , \tag{1.99}$$

that are the normal modes of the structure.

In Fig.1.17(b), we plot the value of the coupling at the different $\omega$ that satisfy equation (1.99). We find that, at $\kappa = 0$, two sets of resonances are clearly visible and the $FSR_1$ of ring 1 and $FSR_2$ of ring 2 are indicated by red and blue arrows, respectively. At $\kappa = 1$, only one set of resonances is visible, with an FSR, indicated by green arrows, smaller than those of the single ring resonators. This is because,
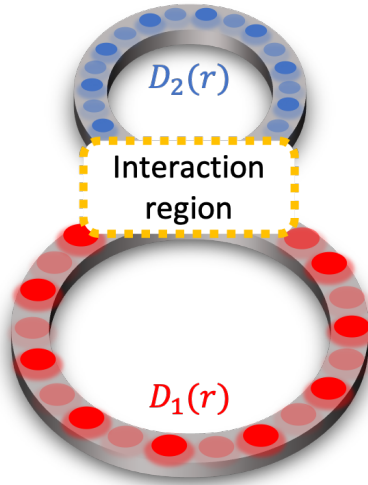
FIGURE 1.18. Schematic representation of two ring resonators that share a common region where the nonlinear interaction can occur. The modes of ring 1 (red) and those of ring 2 (blue) are both present in the interaction region (dotted yellow box) and are orthogonal, in the way specified in (1.101).

actually, there is only one resonator with length $L_1 + L_2$. We underline that the coupling between the two resonators afflicts the resonances, depending on their relative position. In fact, resonances that are closer are shifted further with respect to those that are more spaced. For example, the resonance around $1211\,\mathrm{rad/ps}$ is quite distant from the others and hence it's less shifted and only for high value of $\kappa$. On the other hand, the two almost-degenerate resonances around $1214\,\mathrm{rad/ps}$ are immediately split as the coupling is turned on. This is because the resonators have the same mode, thus

$$\int \boldsymbol{D}_1^*(\boldsymbol{r}) \cdot \boldsymbol{D}_2(\boldsymbol{r}) d\boldsymbol{r} \neq 0 \ , \tag{1.100}$$

and the linear interaction can occur. This behavior recalls the Rabi splitting [36, 37] that takes place, for example, between two degenerate energy levels in a molecule: the energy splitting of the levels is directly proportional to the strength of the interaction. The length of the resonator determines the FSR and thus the recursive overlapping of the resonances. In the example in Fig. 1.17, the ratio between $L_1$ and $L_2$ is 5/3, which is reflected in five $\mathrm{FSR}_1$ and three $\mathrm{FSR}_2$ between two consecutive degenerate resonances (e.g. around $1197\,\mathrm{rad/ps}$ and $1214\,\mathrm{rad/ps}$). This feature can be exploited to engineer some selected resonances of one resonator by properly designing another one that will interact with it. This strategy is what we will investigate in the second chapter of this work, considering the two resonators as the photonic atoms that couple forming a photonic molecule.

The nonlinear coupling of two resonators is a more subtle subject. With this, we mean two (or more) linearly uncoupled resonators that interact only through a

nonlinear interaction. Thus, the question is how such a non-coupling can be achieved, given that the usual way to linearly uncouple two resonators (as those in Fig. 1.17) is to space them apart, but in such case, they would not interact at all. The schematic idea is plotted in Fig. 1.18, showing that the two resonators must have a common region (yellow dotted box) where they share their modes. These modes are orthogonal

$$\int \boldsymbol{D}_1^*(\boldsymbol{r}) \cdot \boldsymbol{D}_2(\boldsymbol{r}) d\boldsymbol{r} = 0 \ , \tag{1.101}$$

preventing light from one resonator to flow into the other, but the nonlinear overlap integral, for example in the case of SFWM

$$\int \Gamma^{(3)}(\boldsymbol{r}) \boldsymbol{D}_1^*(\boldsymbol{r}) \boldsymbol{D}_1^*(\boldsymbol{r}) \boldsymbol{D}_2(\boldsymbol{r}) \boldsymbol{D}_2(\boldsymbol{r}) d\boldsymbol{r} \neq 0 \ , \tag{1.102}$$

is different from zero, allowing the nonlinear interaction to occur. The designing of the uncoupler that can provide such a behavior is the topic of the third chapter of this work.

CHAPTER 2

# Squeezed Light from a Linear Photonic Molecule

In this chapter, we analyze how the linear interaction between two ring resonators can be exploited to engineer the resonances of the composite system. If we consider the two resonators as two atoms, we can call *photonic molecule* the structure composed of the two interacting rings. In the field of quantum technologies, the use of a particular nonclassical state of light, the squeezed state, has proven to be of paramount importance. Squeezed light sources are a fundamental building block of photonic technologies for quantum information processing. Squeezing is an essential resource for quantum sensing [38, 39] and a wide range of quantum computing algorithms [40–42], and much effort has gone into engineering scalable implementations of such sources using integrated photonics. For applications requiring very large numbers of components, high-index-contrast nanophotonic platforms are preferred, as they enable large-scale integration with many hundreds or thousands of elements on a single monolithic chip [43]. In the following we briefly recall what squeezed light is and what technique we adopted to generate such a state of light.

## 2.1. Squeezing

If we consider the position and momentum operators $\hat{x}$ and $\hat{p}$ of an harmonic oscillator of mass $m$, at the angular frequency $\omega$, usually defined as

$$\hat{x} = \sqrt{\frac{\hbar}{2m\omega}}(a^\dagger + a) \qquad (2.1)$$

and

$$\hat{p} = i\sqrt{\frac{\hbar m\omega}{2}}(a^\dagger - a) \ , \qquad (2.2)$$

the Heisenberg uncertainty principle gives

$$\Delta\hat{x}\Delta\hat{p} \geq \frac{\hbar}{2} \ . \qquad (2.3)$$

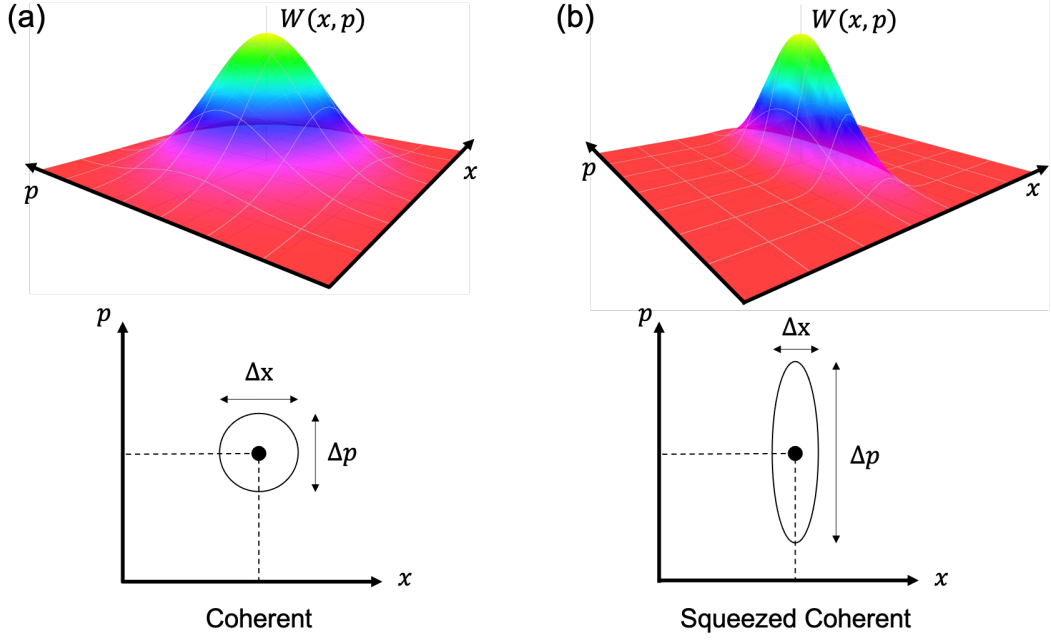In general, a squeezed state can be defined as a state where

FIGURE 2.1. Schematic representation of the Wigner function (top) and of its cross section in the $x$-$p$ plane (bottom) for (a) a coherent state and (b) for a squeezed coherent state.

$$\Delta\hat{x} < \sqrt{\frac{\hbar}{2}} \text{ or } \Delta\hat{p} < \sqrt{\frac{\hbar}{2}} \ , \tag{2.4}$$

that means the standard deviation of one conjugated variable is lower than the shot noise limit. Mathematically, such a state is described by the unitary squeezing operator

$$\hat{S}(\mathfrak{s}) = \exp\left\{\frac{1}{2}\mathfrak{s}^* a^2 - \frac{1}{2}\mathfrak{s}(a^\dagger)^2\right\} \ , \tag{2.5}$$

where $\mathfrak{s}$ is the complex squeezing parameter. An example is schematically pictured in Fig. 2.1, where we compare a standard coherent state $|\alpha\rangle$ with a squeezed coherent state $\hat{S}(\mathfrak{s})|\alpha\rangle$.

We can look at a general phase-dependent quadrature of the field operator, defined as

$$a_\phi(t) = \frac{1}{\sqrt{2}}\left(e^{i\phi}a(t) + e^{-i\phi}a^\dagger(t)\right) \ , \tag{2.6}$$

and see the effect of the squeezing on a vacuum state and on a coherent state, looking at the temporal evolution. We compare the temporal evolution of a vacuum state with that of a squeezed vacuum state in Fig. 2.2. The quadratures plane is represented on the left, with two orthogonal quadratures $a_\phi$ and $a_{\phi+\pi/2}$ and their uncertainties, while
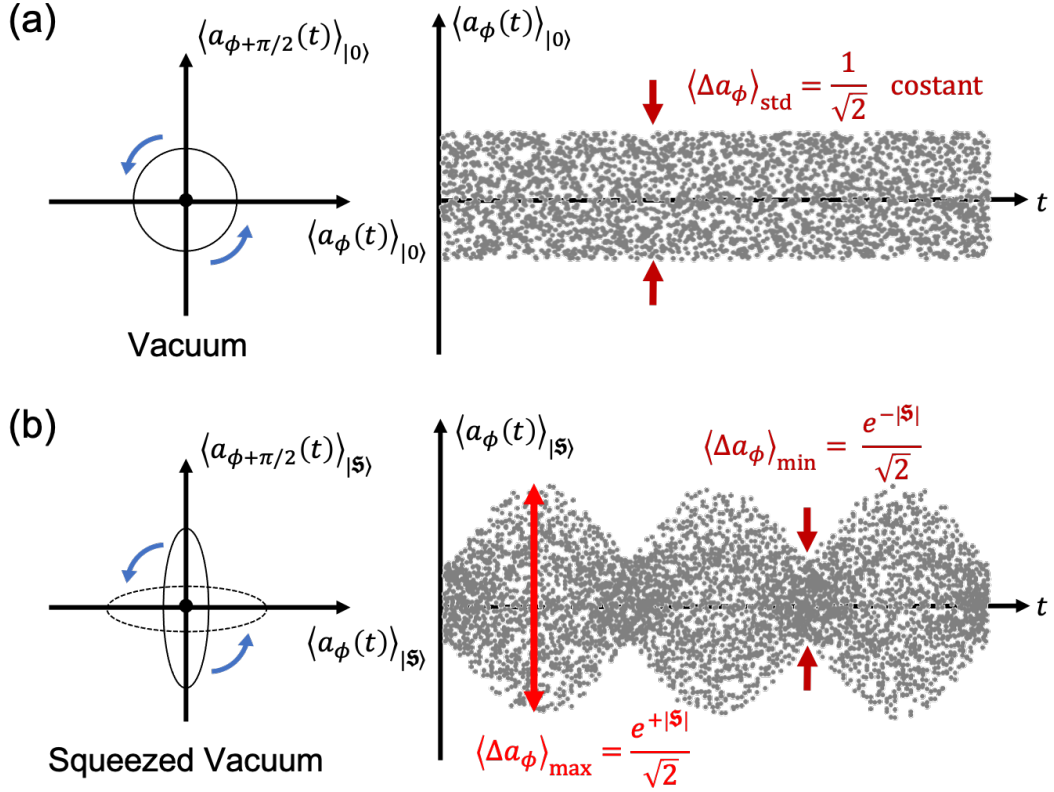
FIGURE 2.2. Schematic representation of the evolution of a state in the the $x$-$p$ plane (left) and corresponding value of the measured quadrature (right) for (a) a vacuum state and (b) for a squeezed vacuum state. The variances and their values are highlighted in the figures.

the evolution of the quadrature $a_\phi$ in time is plotted on the right. The eigenvalues of the quadrature operators are proportional to the electric field. In the case of a vacuum state (Fig. 2.2(a)), we plot

$$\langle a_\phi(t)\rangle_{|0\rangle} = \langle 0| \, a_\phi(t) \, |0\rangle \ , \tag{2.7}$$

and check that the mean value is zero and the uncertainty $\langle \Delta a_\phi \rangle_{\mathrm{std}}$ is constant, as expected. In the case of a squeezed vacuum state (Fig. 2.2(b)), we plot

$$\langle a_\phi(t)\rangle_{|\mathfrak{s}\rangle} = \langle 0| \, \hat{S}^\dagger(\mathfrak{s}) a_\phi(t) \hat{S}(\mathfrak{s}) \, |0\rangle \ , \tag{2.8}$$

and see that, while the mean value is still zero, the uncertainty changes, from a minimum value $\langle \Delta a_\phi \rangle_{\mathrm{min}}$ to a maximum value $\langle \Delta a_\phi \rangle_{\mathrm{max}}$, both dependent on the squeezing parameter $\mathfrak{s}$. Similarly, in Fig. 2.3 are compared the temporal evolution of a coherent state with that of a squeezed coherent state. We plot

$$\langle a_\phi(t)\rangle_{|\alpha\rangle} = \langle \alpha| \, a_\phi(t) \, |\alpha\rangle \ , \tag{2.9}$$
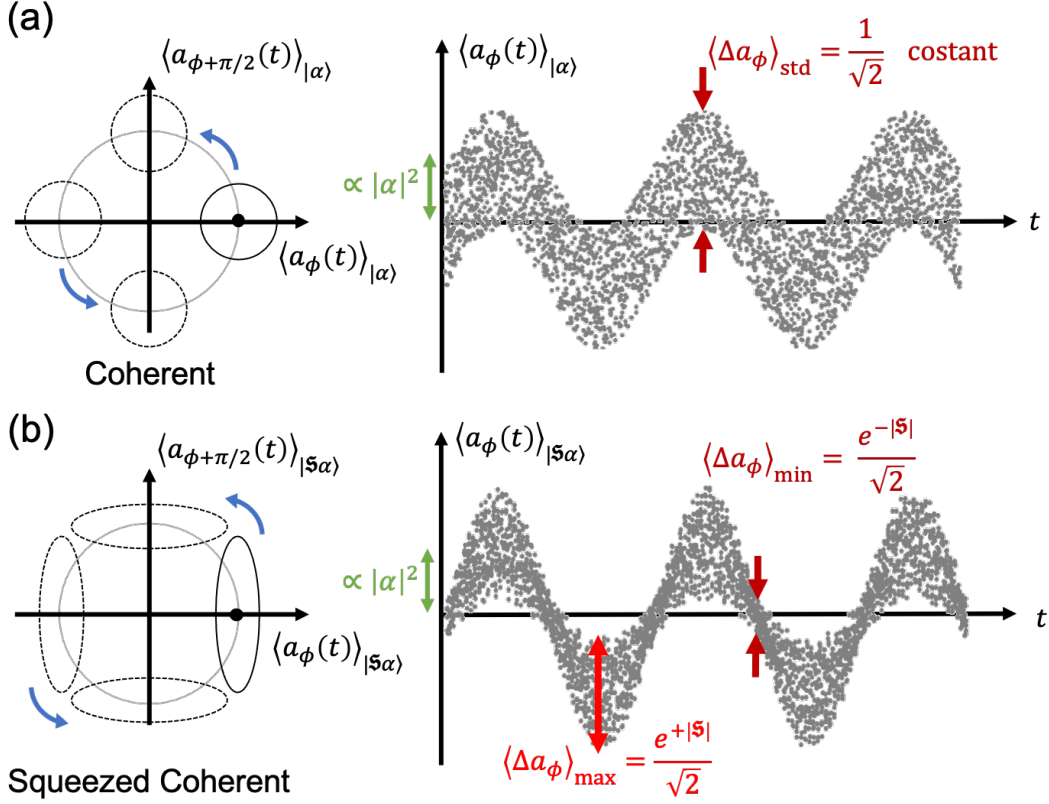
FIGURE 2.3. Schematic representation of the evolution of a state in the the $x$-$p$ plane (left) and corresponding value of the measured quadrature (right) for (a) a coherent state and (b) for a squeezed coherent state. The variances and their values are highlighted in the figures.

in the case of a coherent state (Fig. 2.3(a)) and

$$\langle a_\phi(t)\rangle_{|\mathfrak{s}\alpha\rangle} = \langle\alpha|\,\hat{S}^\dagger(\mathfrak{s})a_\phi(t)\hat{S}(\mathfrak{s})\,|\alpha\rangle \ , \tag{2.10}$$

in the case of a squeezed coherent state (Fig. 2.3(b)). The results are similar to those of Fig. 2.2, with the same behavior of the uncertainties but with a mean value proportional to $|\alpha|^2$.

The usual way to measure a squeezed state of light is through homodyne detection [44], sketched in Fig. 2.4. This setup measures the electric field, or quadrature-operator expectation values, of the incident light as functions of the measurement phase angle. It is a particularly important technique for the study of squeezed light, for its sensitivity to the phase $\phi$ of the signal field allows unambiguous identifications of squeezed light to be made. The light beam to be measured, the signal, is incident on one arm of the beam splitter (BS), while the other arm carries a strong coherent light beam, the local oscillator (LO); at the outputs of the BS there are two photodetectors (PDs). The quantity to be measured is the difference between the numbers
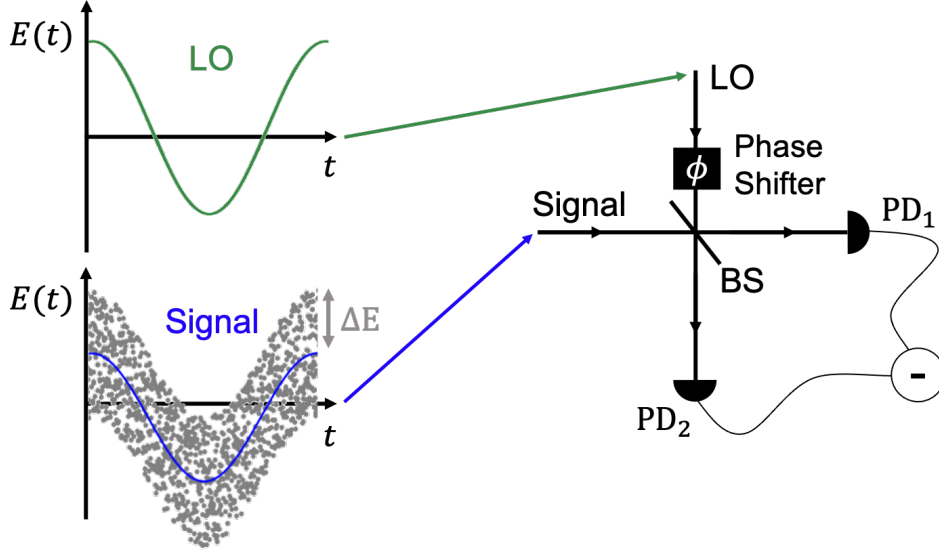
FIGURE 2.4. Homodyne detection scheme. Signal and LO enter the two arms of the BS and photons are detected by two PDs at the output ports. The phase $\phi$ of the LO can be tuned as preferred thanks to a phase shifter. The measured quantity is the difference between the numbers of photons arriving at the two detectors during the measurement time.

of photons arriving at the two detectors during the measurement time. The most sensitive measurements are made by balanced homodyne detection, where a 50:50 BS is used. The LO needs to be much more intense than the signal field and its effect is to produce measurements proportional to the signal field.

By comparing the two photon state expression of eq. (1.31) with that of the squeezing operator of eq (2.5), we find that the link between the squeezing parameter and the number of generated pairs is

$$\mathfrak{s} = 2\beta \ , \tag{2.11}$$

which suggests that the more efficient the pair generation is, the higher the level of squeezing will be. Commonly, the level of squeezing is indicated by the squeeze factor $\mathfrak{f}$ [45], which is defined by

$$\mathfrak{f} = -10 \operatorname{Log}\left( \frac{\langle \Delta a_\phi \rangle^2}{\langle \Delta a_\phi \rangle^2_{\mathrm{std}}} \right) \ , \tag{2.12}$$

and is expressed in dB, where $\langle \Delta a_\phi \rangle^2$ and $\langle \Delta a_\phi \rangle^2_{\mathrm{std}}$ are the variances of the measured squeezed state and of the standard coherent or vacuum state with minimum uncertainty, respectively. A $3\,\mathrm{dB}$ level of squeezing denotes that the variance of one quadrature is half that of the non-squeezed state. When a squeezed state experiences optical loss, it remains squeezed but the squeeze factor is reduced. Also the state's purity is reduced, i.e. the product of the quadrature uncertainties increases above the minimum value. To maximize the benefit from squeezed states in applications,

strongly squeezed states need to be generated and optical loss minimized. The first signature of squeezed light was observed in a groundbreaking experiment using four-wave mixing in an atomic vapor of sodium atoms [46]. In bulk systems, the current record level of squeezing is 15 dB [47]. It would be desirable, though, to obtain an integrated squeezing source on chip, and to do so a lot of effort has been made. We now show the technique we studied that can be applied to obtain a vacuum-squeezed state of light.

## 2.2. Dual-pump SFWM and parasitic processes

A number of solutions to generated a squeezed state of light has already been proposed. Within the domain of nanophotonic structures, bright intensity-difference squeezing in a silicon nitride ring resonator driven above the parametric oscillation threshold has been demonstrated [26]. Subsequently, a two-ring structure was used to enable tuning of the level of squeezing by varying the effective resonator coupling condition [48]. Single-ring resonators driven below threshold have yielded two-mode (nondegenerate) quadrature squeezing and photon number difference squeezing [49]. Micromechanical resonators have generated small levels of squeezing over a few MHz of bandwidth [50]. Some squeezing in a single-mode degenerate configuration has also been reported with microrings using a single-pump [51], but this suffers from strong excess noise contributions arising from non-parametric effects such as thermorefractive fluctuation [52]. Aside from limiting the amount of available squeezing, the presence of excess noise is especially undesirable for quantum computing applications, as such noise degrades the purity of the quantum states employed. No nanophotonic device has yet been demonstrated which efficiently produces quadrature squeezed vacuum in a single, degenerate spectral mode, uncontaminated by excess noise from both non-parametric and unwanted parametric processes. A promising candidate has been proposed based on dual-pump spontaneous four-wave mixing (DP-SFWM) in microring resonators [53, 54]. Microring resonators are also desirable for the broadband
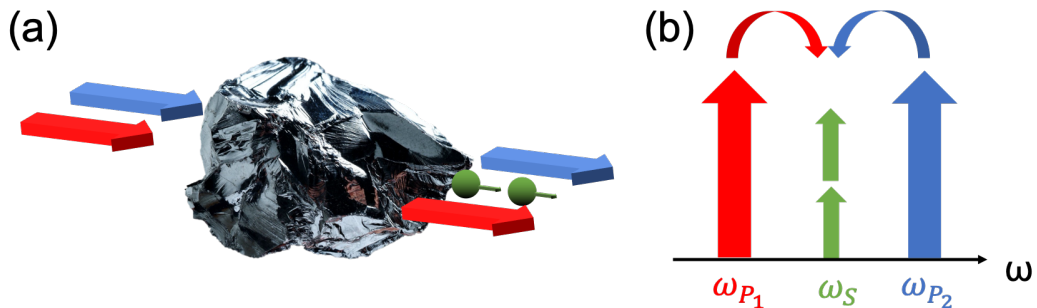


FIGURE 2.5. Schematic representation of (a) DP-SFWM by a $\chi^{(3)}$ medium (e.g. Silicon) and (b) frequencies involved in the process.
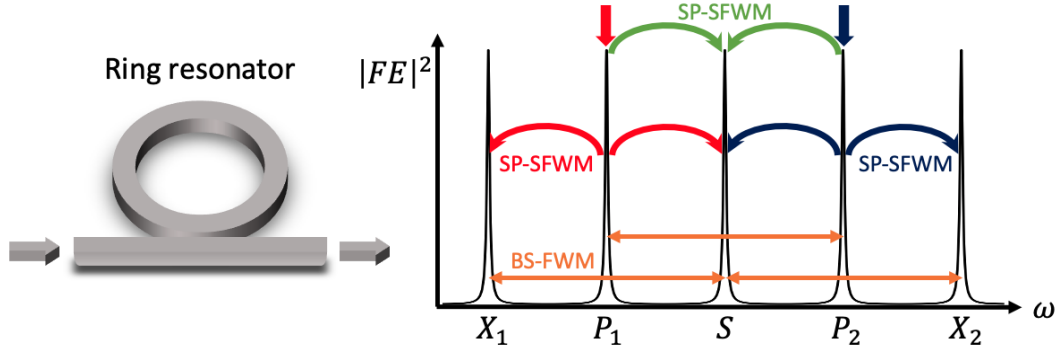
FIGURE 2.6. Intensity enhancement inside a single-ring resonator, showing both DP-SFWM (green arrows) and parasitic processes of SP-SFWM (red and blue arrows) and BS-FWM (orange arrows) that occur when two resonances $P_1$ and $P_2$ are pumped.

nature of the squeezing they can produce [55]. DP-SFWM process, schematically represented in Fig. 2.5, is a third order nonlinear process like SP-SFWM but where there are two pump fields that are injected at two different frequencies and the pair of photon is generated in a single, degenerate spectral mode, denoted as signal. By using pumps very well separated in frequency from the squeezed mode, noise contributions from non-parametric effects like thermorefractive fluctuations can be avoided. However, in such a system a number of unwanted parametric effects [56] add noise to the squeezing band, irreversibly corrupting the output. The primary culprit for such unwanted noise is SP-SFWM [57] driven by each individual pump; further degradation is caused by Bragg-scattering four-wave mixing (BS-FWM) [58], which can transfer energy away from the squeezed mode. A schematic of the four-wave mixing processes that can occur while attempting DP-SFWM in a standard ring resonator is pictured in Fig. 2.6. Here, the target process of DP-SFWM from modes $P_1$ and $P_2$ to $S$ is shown with green arrows, while the parasitic processes of SP-SFWM with red and blue arrows, and BS-FWM with orange arrows. The unwanted processes of SP-SFWM from $P_1$ and $P_2$ generate excess noise in the $S$ mode, contaminating the output, while BS-FWM transfers photons away from the $S$ mode as photons are exchanged between the two pumps. The resonances $X_1$ and $X_2$, due to the evenly-spaced resonances in the ring comb, are those responsible for the parasitic processes that compromise the quality of the generated state and are those that have to be removed.

Without suppression of parasitic effects, it was shown that only $0.8\,\mathrm{dB}$ of squeezing would have been achievable. To overcome this, some suppression of parasitic processes was achieved by detuning the pumps from resonance, with $1.34\,\mathrm{dB}$ of degenerate squeezing observed and $3.09\,\mathrm{dB}$ of squeezing inferred on-chip [59]. The schematic idea of the parasitic-process suppression is pictured in Fig. 2.7. Here, we see that shifting the pump resonances, necessarily less than one linewidth, away from the $S$ mode can
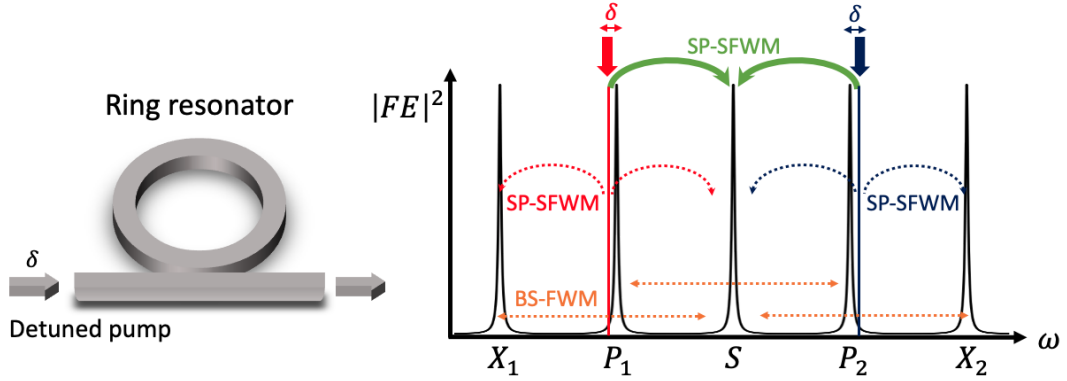
FIGURE 2.7. Schematic representation of the detuning strategy in a ring resonator. Modes $P_1$ and $P_2$ are exited slightly off-resonance to avoid the energy conservation to be satisfy for SP-SFWM between modes $P_1$, $S$, $X_1$ and $P_2$, $S$, $X_2$.

eliminate the energy match for the single pump process to occur in modes $X_1$ and $X_2$. However, this strategy suffers from a significant trade-off between squeezing and pump power efficiency, as detuning the pumps reduces their resonance enhancement in the ring, compromising the efficiency of the desired squeezing process. The strategy of directly engineering the resonances can bypass the detuning approach by strongly suppressing unwanted parasitic nonlinear effects without significantly compromising the generation efficiency.

## 2.3. The snowman

The structure we studied is composed of two strongly-coupled ring resonators [60], as sketched in Fig. 2.8(a). The principal ring, where the generation happens, is coupled to a bus waveguide for pump injection and photons extraction. The auxiliary ring is used to engineer particular resonances of the principal one. We leverage a design based on photonic molecules: these devices are composed of two or more optical resonators, arranged such that some of the modes of each resonator are coupled to those of the other. Such structures have been used for emulating the behavior of two-level systems [61], lasing [62], and on-demand optical storage and retrieval [63]. Coupled resonators have also been used for dispersion engineering of integrated devices [64, 65], enhancing their performance for nonlinear optical applications. In ring resonators, both SP-SFWM and BS-FWM effects are strongly enhanced by the presence of resonances that are otherwise not relevant to the desired dual-pump squeezing dynamics. To suppress these unwanted processes, it suffices to design a structure for which the two resonances labelled $X_1$ and $X_2$ are removed or suitably corrupted, without significantly degrading the properties of the resonances used for the two pumps and the signal, labeled $P_1$ and $P_2$, and $S$, respectively. To that end, tuning the auxiliary ring such that the $X_1$ and $X_2$ resonances of the principal ring nearly coincide in
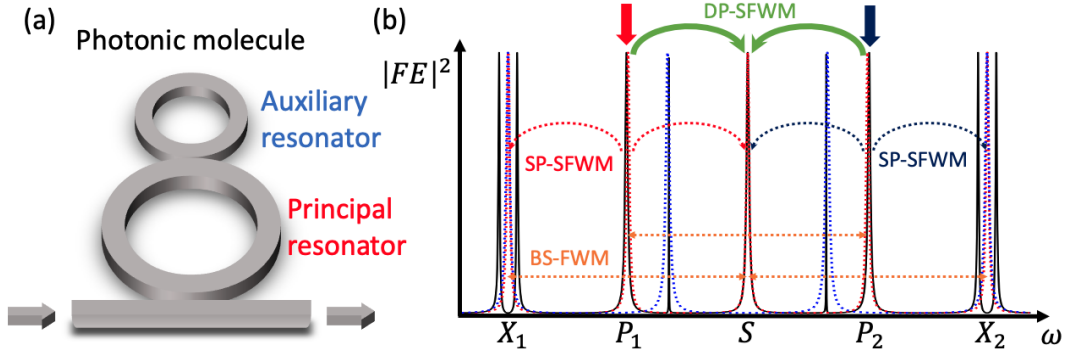
FIGURE 2.8. (a) Sketch of the photonic molecule structure, with the principal and auxiliary ring resonators. (b) Intensity enhancement of the two-ring photonic molecule. The resonances of the sole principal and auxiliary resonators are plotted in dashed-red and dashed-blue lines, respectively. The comb of the photonic molecule is represented in solid black line, showing the splitting and detuning of the hybridized $X_1$ and $X_2$ resonances that arises from the strong linear coupling between the principal and auxiliary resonator, which leads to the suppression of the parasitic processes (dashed arrows).

frequency with resonances of the auxiliary resonator, gives rise to two new hybridized resonances, strongly split and detuned from their original frequencies (Fig. 2.8(b)). The unwanted parametric processes involving the original $X_1$ and $X_2$ resonances are thereby highly suppressed. Since this modification to the $X_1$ and $X_2$ resonances can occur without having a significant impact on the $P_1$, $P_2$, and $S$ resonances, strong enhancement of the desired squeezing process is maintained. Thus, the free spectral range of the auxiliary resonator is chosen to be four-third of that of the principal resonator, so that only every fourth mode of the principal resonator is hybridized.

The device is fabricated on a commercially available stoichiometric silicon nitride ($Si_3N_4$) strip waveguide platform offered by Ligentec SA. The waveguide cross-section is $1500\,nm \times 800\,nm$ (width $\times$ thickness) and is fully cladded in $SiO_2$. This platform and cross-section are selected for low propagation loss, lack of two-photon absorption, and high third-order optical nonlinearity. Independent microheaters are overlaid to provide thermal tuning of each resonator. The principal resonator is designed to have radius $R = 114\,\mu$m, and the auxiliary resonator to have radius $0.75 \times R$, leading to free spectral ranges of $200\,GHz$ for the principal resonator, and $267\,GHz$ (approximately one-third larger) for the auxiliary resonator. The principal resonator is strongly over-coupled to the bus waveguide, resulting in an escape efficiency of $\sim 90\%$ in the wavelength range of interest; such over-coupling is important to limit the amount of loss experienced by the squeezed light on-chip. A micrograph of the device and the linear transmission spectrum measurements of the fundamental transverse electric resonances in the wavelength range of interest were performed by the Xanadu Quantum Technology group in Toronto (CA) and are exhibited in Fig. 2.9(a) and 2.9(b), respectively. The auxiliary resonator microheater is tuned to achieve spectral
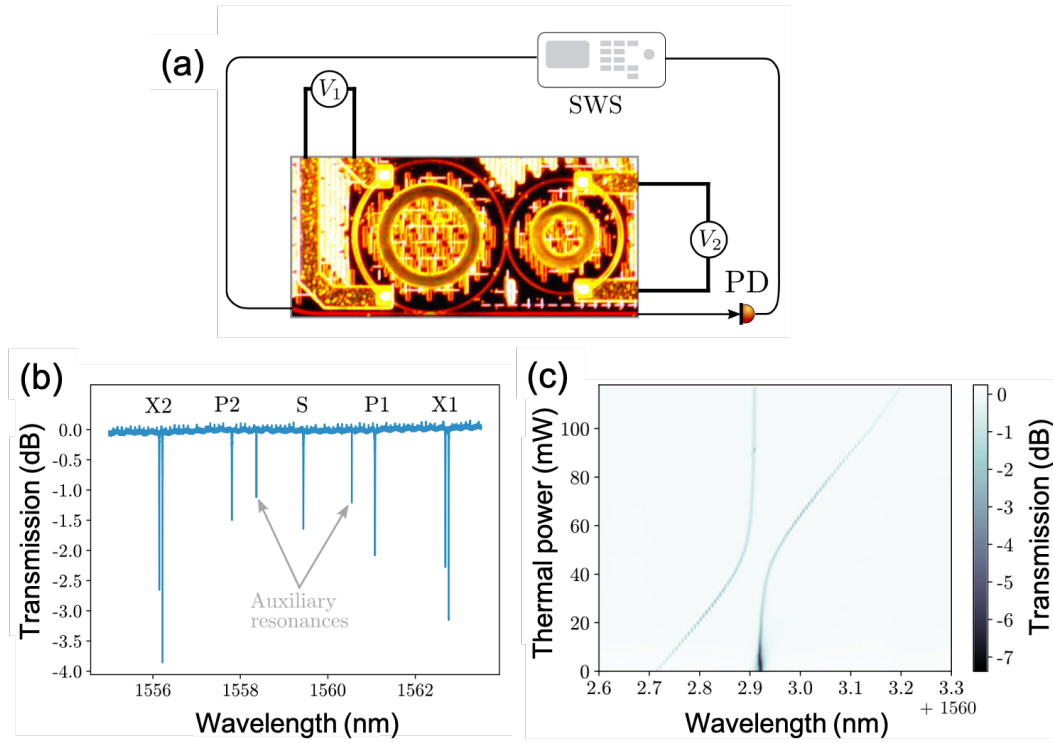
FIGURE 2.9. (a) Micrograph of the photonic molecule structure and simplified schematic of the apparatus for linear characterization. The principal resonator is on the left, coupled at the bottom to a bus waveguide. The smaller ring on the right acts as the auxiliary resonator. Microheaters overlaid apply voltages $V_1$ and $V_2$ to the principal and auxiliary heaters, respectively. A swept wavelength source (SWS) and photodiode (PD) measure the transmission spectrum of the device. (b) Measured TE polarization transmission spectrum of the device in the wavelength range of interest, with resonators tuned to hybridize the unwanted resonances $X_1$ and $X_2$. Also evident are two resonances of the auxiliary resonator, which are indirectly weakly coupled to the bus waveguide via the principal resonator. (c) Transmission spectrum near the $X_1$ resonance doublet of the device as the power dissipated by the auxiliary microheater is scanned. The resonance doublet exhibits the classic "avoided crossing" behavior associated with a pair of hybridized modes of a photonic molecule. Images taken from [60].

alignment of the resonances associated with the auxiliary and principal resonator, leading to the formation of hybrid, split resonances $X_1$ and $X_2$. The three resonances of interest of the principal resonator are preserved, displaying un-split Lorentzian lineshapes with loaded quality factors of $\sim 3 \times 10^5$. The transmission spectrum of the device for a range of different auxiliary microheater settings is plotted in Fig. 2.9(c) for wavelengths near the $X_1$ resonance. As the auxiliary resonances are tuned, the resonance doublet exhibits the classic avoided crossing behavior of coupled modes in a photonic molecule as the coupling strength (in this case determined by the detuning between $X_1$ resonances of the auxiliary and principal resonators) is varied (we saw this splitting behavior in Fig. 1.17 of chapter 1).
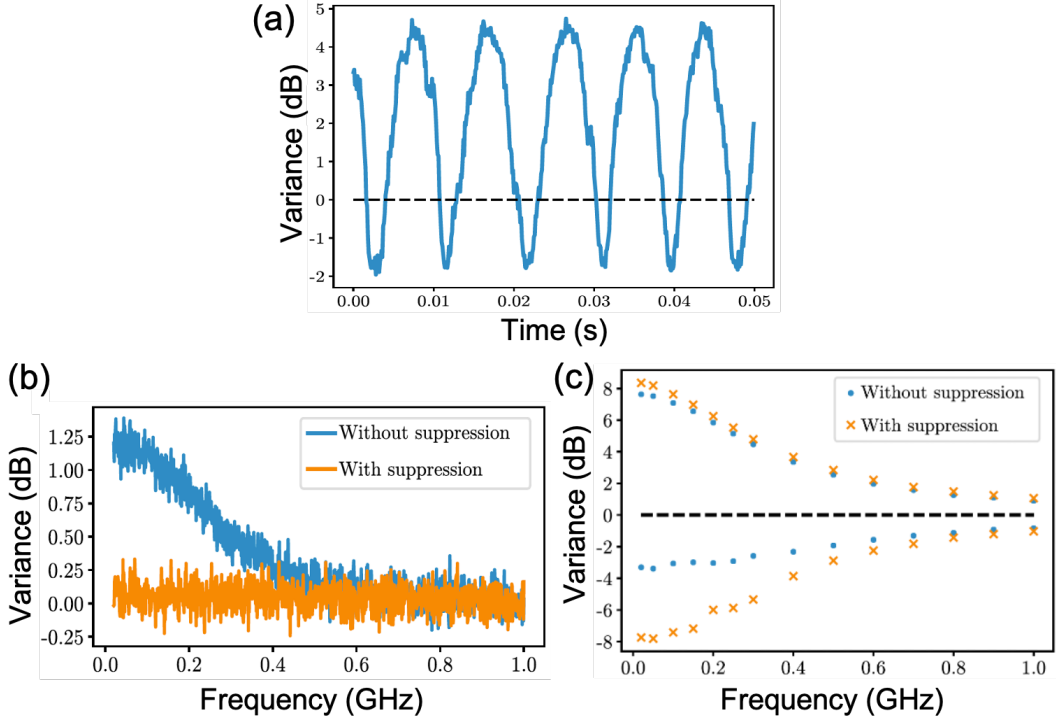
FIGURE 2.10. (a) Quadrature variance at 20 MHz sideband frequency (blue trace) normalized to shot noise, plotted as a function of time as the LO phase is ramped. The black dashed line is the shot noise level. (b) Single-pump parametric fluorescence spectrum (normalized to shot noise) in the $S$ mode, measured using homodyne detection with one pump turned off. The blue trace is taken with the auxiliary resonator tuned such that the $P_1$, $S$, and $X_1$ resonances are not significantly coupled to the principal resonator, effectively disabling the noise suppression, resulting in the contamination of the signal mode with broadband unwanted noise. The orange trace is taken with the auxiliary resonator tuned to split the $X_1$ and $X_2$ resonances, suppressing the noise to less than 0.1 dB above shot noise over the entire measurement band. For both traces the pump power was 75 mW, and the noise observed is phase-insensitive, as expected for single-pump parametric fluorescence. (c) On-chip squeezing and anti-squeezing spectra with noise suppression enabled (orange crosses) and disabled (blue points). The pump power was adjusted from 70 mW for the suppression-enabled case to 90 mW for the suppression-disabled case to keep the anti-squeezing approximately fixed, compensating for small changes in the overall four-wave mixing efficiency associated with tuning the auxiliary resonator. Squeezing is strongly diminished with noise suppression disabled. Images taken from [60].

A representative quadrature variance trace at 20 MHz sideband frequency is shown in Fig. 2.10(a) as the local oscillator phase is ramped. The directly measured squeezing was 1.65(1) dB. As the total collection and detection efficiency was 38(2)% (factoring in all losses experienced by the squeezed light except the resonator escape efficiency), this corresponds to ~8(1) dB of squeezing available at the device output on-chip. This is consistent with the maximum amount of squeezing possible from this device: as the principal resonator escape efficiency is ~ 90%, the maximum amount of squeezing on-chip is limited to 10 dB. For comparison, the level of squeezing required for fault-tolerant continuous variable quantum computation was recently shown to

be $\sim 10\,\mathrm{dB}$ [66]. To assess the importance of the auxiliary resonator in suppressing unwanted processes, the parametric fluorescence noise spectrum generated in the $S$ mode was measured with only the pump at $P_1$ turned on, with $70\,\mathrm{mW}$ on-chip power. The results are shown in Fig. 2.10(b) for two different voltages applied to the auxiliary resonator. When the auxiliary resonator is tuned such that the $X_1$ resonance is no longer hybridized, a strong noise contribution (more than $1.2\,\mathrm{dB}$ above shot noise) on all quadratures is observed. This excess noise is reduced to $< 0.1\,\mathrm{dB}$ above shot noise when the auxiliary resonator is appropriately tuned. In the absence of the auxiliary resonator, several dB of excess noise would therefore be present in the $S$ mode, severely degrading the purity and achievable squeezing in the generated quantum state. This effect can also be directly seen in Fig. 2.10(c), in which the on-chip squeezing and anti-squeezing spectra are shown with noise suppression enabled (orange crosses) and disabled (blue points). For fair comparison, the power was adjusted from $70\,\mathrm{mW}$ for the data with suppression enabled to $90\,\mathrm{mW}$ for the data with suppression disabled, in order to maintain a fixed degree of anti-squeezing. This adjustment in power was necessary to compensate for the small perturbations in the effective quality factors and resonance frequencies of the principal ring that arise from tuning the auxiliary resonator. The suppression of unwanted parametric processes is crucial to demonstrate strong single-mode squeezed light sources based on four-wave mixing. This is possible by designing a nanophotonic molecule to selectively suppress unwanted parasitic processes without significantly affecting squeezing efficiency. These results highlight the significant control that can be achieved over quantum nonlinear optical processes by exploiting nanophotonic platforms, and remove a significant barrier impeding progress towards scaling up devices for photonic quantum information processing.

Depending on the kind of problem that one has to overcome and on the degree of control that one wants to achieve on the photonic system, strong coupling may not be the best strategy. In the next chapter we will see the counterpart of this approach, which is the linear uncoupling.

CHAPTER 3

# Photon Pairs from Linearly Uncoupled Resonators

In this chapter, we investigate a completely different strategy to gain the desired control on the resonance comb of a structure. The goal is to exploit the linear uncoupling of two resonators that still are coupled through a nonlinear interaction. This idea was first proposed by Menotti et al. [67] a few years ago for studying SFWM in a two-racetrack resonators system. In this kind of structure, each normal mode can be associated with one resonator, and energy passes from one mode to the other only thanks to the presence of a nonlinear interaction. This can occur because two or more normal modes that are nonlinearly coupled overlap in part of the structure. Having the resonators linearly uncoupled facilitates the engineering of their spectral properties and resonant field enhancement. This is particularly useful for nonlinear optical processes, which typically require several conditions to be met, from those necessary to guarantee the process efficiency (e.g. phase-matching) to those needed to suppress the notorious parasitic processes. In such structures, the strength of the nonlinear interaction is usually reduced compared to what it would be if the modes were sharing the full structure, like for SFWM involving the modes of a single ring resonator. This is why this strategy is more suitable for application in the field of quantum communication, e.g. quantum keys distribution, where the focus is on the on-demand production of entangled pairs of photons rather than a high conversion efficiency, but it can be applied also where an effective precise suppression of the parasitic processes is needed, like the generation of squeezed states.

## 3.1. Linearly uncoupled resonators

We begin by considering structures of the general form sketched in Fig. 3.1, composed of two racetrack resonators of length $L_1$ and $L_2$ and a coupling region, the "coupler", between them. Each resonator is also point-coupled to a bus waveguide, where $\sigma_{1,m(2.m)}$ is the usual waveguide self-coupling coefficient, described in chapter 1, between the bus waveguide and the Resonator 1 (2) at frequencies in the neighborhood of its $m$-th resonance, with $0 \leq \sigma_{1,m(2.m)} \leq 1$. We assume the bus waveguides and the waveguides of the resonators to be the same and single mode at the frequencies of interest. We are interested in couplers that can be designed so that in the linear regime there is actually *no* coupling. That is, linearly propagating light enters the coupler from one resonator and exits into the *same* resonator.
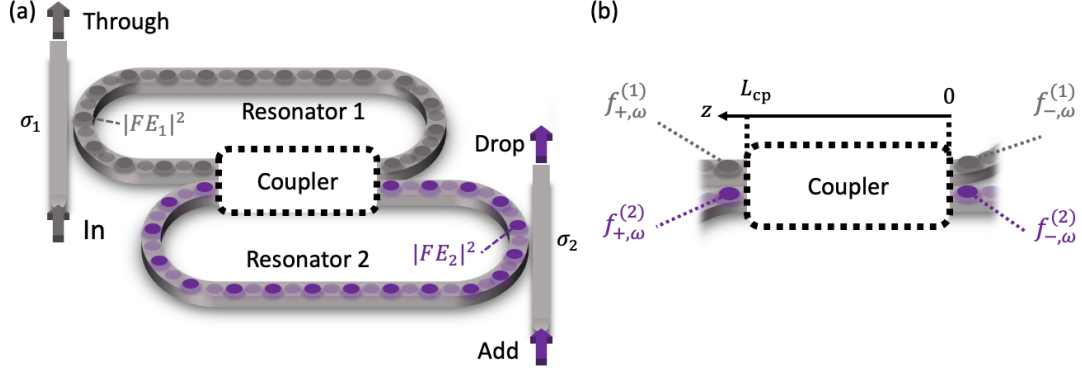
FIGURE 3.1. (a) Sketch of the double racetrack resonator structure, with the resonant fields inside Resonator 1 (grey) and Resonator 2 (purple), and (b) detail of the coupler, with the incoming and outgoing fields.

We want to describe the coupler with the same scattering matrix $X$ (1.64) we used in chapter 1. This unitary matrix links the input fields $f_{-,\omega}^{(1)}$ and $f_{-,\omega}^{(2)}$ at the beginning of the coupler ($z = 0$) to the output fields $f_{+,\omega}^{(1)}$ and $f_{+,\omega}^{(2)}$ at the end of it ($z = L_{\mathrm{cp}}$) as

$$\begin{pmatrix} f_{+,\omega}^{(1)} \\ f_{+,\omega}^{(2)} \end{pmatrix} = X \begin{pmatrix} f_{-,\omega}^{(1)} \\ f_{-,\omega}^{(2)} \end{pmatrix} = \begin{pmatrix} X_{11} & X_{12} \\ X_{21} & X_{22} \end{pmatrix} \begin{pmatrix} f_{-,\omega}^{(1)} \\ f_{-,\omega}^{(2)} \end{pmatrix}, \tag{3.1}$$

where $f_{\pm,\omega}^{(i)}$ is the field circulating in the $i$-th resonator at angular frequency $\omega$. If we want the two resonators to be uncoupled, in a realistic situation the terms $X_{12}$ and $X_{21}$ should be as close as possible to zero. Naturally, one could achieve high linear isolation of the two racetracks by designing a coupler with very distant waveguides, but this would also prevent any nonlinear interaction between them. Instead, one can construct the coupler such that the modes of the two resonators share a spatial region inside of it, and yet the two resonators are uncoupled in the linear regime. In such a situation, each resonator has a well-defined set of resonances that are associated with light confinement mainly in it and thus its linear properties are similar to those of the ring resonator described in chapter 1.

To characterize this structure in the linear regime, in Fig. 3.2 we plot the transmission and the intensity enhancement as a function of frequency for various in/out port configurations (see Fig. 3.1). We assume a realistic case in which the two resonators are just nearly linearly uncoupled, and consider a frequency range $|\omega - \omega_{i,m}| \ll v_g/L_i$. Then, one can easily identify modes associated primarily with one or the other of the two resonators, and find more than $30\,\mathrm{dB}$ on-resonance isolation between the two resonators. In a practical realization of such devices, a striking advantage of this configuration is that one can control the relative position of the two resonance combs by means of electric heaters [68], or any other mechanism that induces an effective
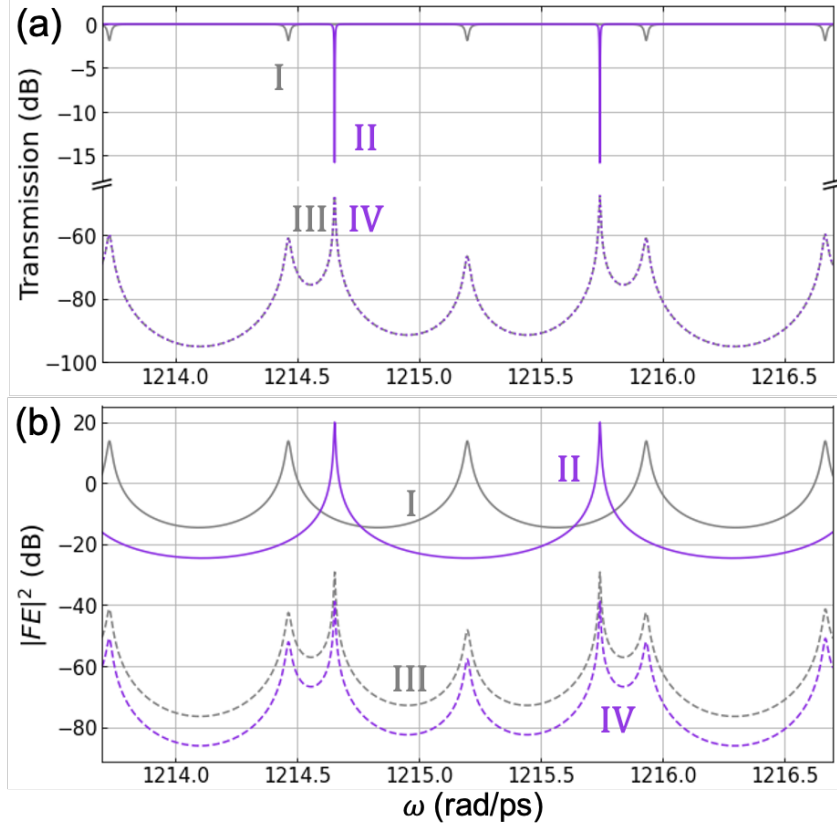
FIGURE 3.2. (a) Transmission spectra for "In" to "Through" (I), "Add" to "Drop" (II), "In" to "Drop" (III), and "Add" to "Through" (IV). (b) Corresponding intensity enhancement. The dips in the lines I and II of plot (a), which occurs at the resonance frequencies, correspond to the intensity enhancement peaks of lines I and II shown in plot (b). We assumed $L_1 = 641 \, \mu m$, $L_2 = 432 \, \mu m$, $\sigma_1 = 0.933$, $\sigma_2 = 0.993$, $\xi = 0.23 \, \text{cm}^{-1}$ (corresponding to $1 \, \text{dB/cm}$), and a value of the coupling coefficient $X_{12} = X_{21} = -i0.00161$, the last to ensure that the resonators are nearly linearly uncoupled.

refractive index change in one of the resonators in a region far from the coupler. In the limit where the "coupler" in fact provides no coupling between the resonators in the linear regime, when low intensity light is injected into the $i^{th}$ resonator through the corresponding bus waveguide, the intensity enhancement in the resonator of light at frequencies close to that of the $m^{th}$ resonance is described by equation (1.69).

Note that the field distribution inside the coupler is not relevant to the establishment of linear uncoupling, as long as it is guaranteed that light entering from one resonator is redirected into the same one. However, if one is interested in achieving nonlinear coupling between the two resonators, the field distribution inside the coupling region is crucial, as the strength of the nonlinear interaction depends on the spatial integral of the involved fields, which can be nonvanishing only in the coupling region. The coupler can be realized in several ways, and the use of the device for implementing different nonlinear optical processes can be considered. In

this work we study two possibilities for the structure: a directional coupler (DC) and a Mach-Zehnder interferometer (MZI). Also, we consider the use of the device for implementing parametric fluorescence, where pump light is injected in the "In" port at a resonance frequency of Resonator 1, and signal and idler light is generated at resonance frequencies of Resonator 2 and exits through the "Drop" port.

**3.1.1. Directional coupler.** We first consider the structure where the coupler is a DC with length $L_{\mathrm{DC}}$, as sketched in Fig. 3.3. The linear coupling between the two waveguides forming the DC can be described in the framework of standard coupled mode theory [12], in which the coupling constant $\kappa_{\mathrm{DC}}$ depends on the linear overlap integral of the transverse field profile of the waveguide modes, which is a function of distance along the coupling region. We restrict ourselves to a frequency range sufficiently small that $\kappa_{\mathrm{DC}}$ can be considered frequency independent. Then, when $L_{\mathrm{DC}} = n\pi/\kappa_{\mathrm{DC}}$, with $n$ a positive integer, the DC cross transmission is zero, yielding a high isolation of the two resonators in the linear regime [67]; in the absence of coupling to the bus waveguides, the energy of the resonant modes of the structure would be mainly confined to one resonator or the other.

We now take a closer look to the field distribution inside the DC, as sketched in Fig. 3.3. Following equation (1.17), one can write the displacement field associated with each channel as

$$\mathbf{D}_{ch,\omega}(\mathbf{r}) = \sqrt{\frac{\hbar\omega}{4\pi}} f_{ch,\omega}(z)\mathbf{d}_{ch}(x,y)e^{ik(\omega)z}, \tag{3.2}$$

where $ch = $ up, lo, with "up" ("lo") referring to the channel belonging to Resonator 1(2) as shown in Fig. 3.1, and $\mathbf{d}_{ch}(x,y)$ is the displacement field distribution in the plane transverse to the propagation direction, properly normalized [16]. As we take all the waveguides involved in the structure to be the same, we can assume that
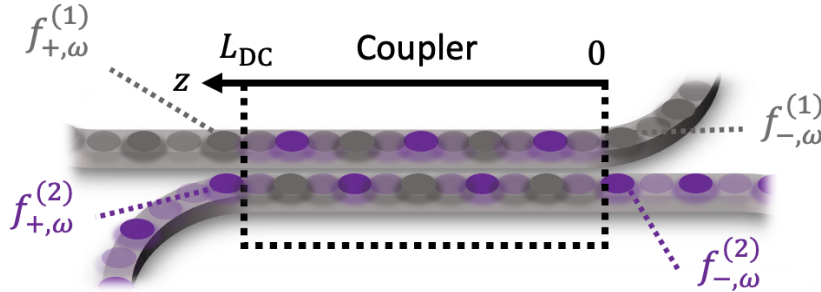


FIGURE 3.3. (a) Sketch of the double racetrack resonator structure, with the resonant fields inside Resonator 1 (grey) and Resonator 2 (purple), and (b) detail of the coupler, with the incoming and outgoing fields.

$\mathbf{d}_{ch}(x, y)$ is the same for all the channels under consideration and also that it can be approximated as independent of $\omega$. Finally, $f_{ch,\omega}(z)$ is a slowly varying envelope function that takes into account for the field distribution along $z$; this function does not depend on the intensity of the light circulating in the structure but rather on the geometry of the coupler. We have

$$\begin{cases} f_{\text{up},\omega}^{\text{DC}}(z) = f_{\text{up},\omega}(0) \cos(|\kappa_{\text{DC}}|z) - i f_{\text{lo},\omega}(0) \sin(|\kappa_{\text{DC}}|z) \\ f_{\text{lo},\omega}^{\text{DC}}(z) = -i f_{\text{up},\omega}(0) \sin(|\kappa_{\text{DC}}|z) + f_{\text{lo},\omega}(0) \cos(|\kappa_{\text{DC}}|z) \; , \end{cases} \tag{3.3}$$

with $f_{\text{up(lo)},\omega}(0)$ determined by the appropriate boundary conditions: $f_{\text{up(lo)},\omega}(0) = f_{-,\omega}^{(1,2)}$, and $f_{\text{up(lo)},\omega}(L_{\text{DC}}) = f_{+,\omega}^{(1,2)}$. Then the coefficients of the scattering matrix (1.64) are found to be

$$X_{11} = \cos|\kappa_{\text{DC}}|L_{\text{DC}}), \tag{3.4}$$

$$X_{12} = -i \sin(|\kappa_{\text{DC}}|L_{\text{DC}}), \tag{3.5}$$

$$X_{21} = -i \sin(|\kappa_{\text{DC}}|L_{\text{DC}}), \tag{3.6}$$

$$X_{22} = \cos(|\kappa_{\text{DC}}|L_{\text{DC}}), \tag{3.7}$$

where note that overall phase $e^{ik(\omega)L_{\text{DC}}}$ due to the field propagation in the DC is included in the fast varying component of (3.2).

In Fig. 3.4 we show the field profile inside the DC for two different coupling configurations. We first consider the field distribution $|f_{up}(z)|^2$ in the upper channel
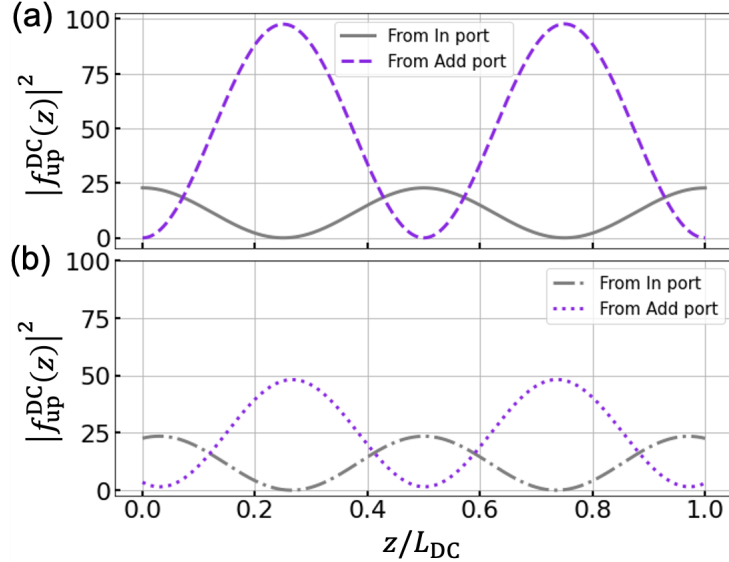


FIGURE 3.4. Intensity distribution in the upper channel of the DC for two different values of the coupling coefficient, namely (a) $\kappa_{\text{DC}} = 0.064\,\mu\text{m}^{-1}$ (perfect uncoupling) and (b) $\kappa_{\text{DC}} = 0.068\,\mu\text{m}^{-1}$ (residual coupling).

in the case of perfect linear uncoupling (see Fig. 3.4(a)). We assume a typical value of $\kappa_{\mathrm{DC}} = 0.064\,\mu\mathrm{m}^{-1}$, and we take $L_{\mathrm{DC}} = 2\pi/\kappa_{\mathrm{DC}} = 98.2\,\mu\mathrm{m}$. Light is injected into the "In" port (solid grey line) on resonance with Resonator 1 at $\omega_{\mathrm{In}} = 1215.20\,\mathrm{rad/ps}$ ($\lambda_{\mathrm{In}} = 1550.07\,\mathrm{nm}$) and into the "Add" port (dashed violet line) on resonance with Resonator 2 at $\omega_{\mathrm{Add}} = 1214.67\,\mathrm{rad/ps}$ ($\lambda_{\mathrm{Add}} = 1550.75\,\mathrm{nm}$) (see Fig. 3.2). As expected, in this situation, at the beginning ($z = 0$) and at the end ($z = L_{\mathrm{DC}}$) of the DC, $|f_{\mathrm{up}}^{\mathrm{In}}(z)|^2$ is maximum, while $|f_{\mathrm{up}}^{\mathrm{Add}}(z)|^2$ is zero.

We now consider a small deviation from this ideal situation; we take the same $L_{\mathrm{DC}} = 98.2\,\mu\mathrm{m}$, but a larger coupling constant $\kappa_{\mathrm{DC}} = 0.068\,\mu\mathrm{m}^{-1}$. This would arise, for example, if the waveguides were slightly closer to each other than in the ideal situation. We plot the corresponding intensity distribution in Fig. 3.4(b). Unlike the ideal situation, here the intensity of the light injected into the "Add" port is slightly different from zero at the end of the waveguide, and that of the light injected into the "In" port is not quite at the maximum there, indicating a small linear coupling between the two resonators. More surprisingly, while the field intensity for the light associated with the mode of Resonator 1 is essentially unchanged, that associated with the mode of Resonator 2 is half of that shown in Fig. 3.4(a). Such a remarkable difference demonstrates that the presence of some coupling between two resonators, as occurs if the DC is not ideal, does not affect all the modes in the same way. If we look at Fig. 3.2, we notice that the resonance associated with Resonator 2 at 1214.67 rad/ps is close to a resonance of Resonator 1, and thus even a small variation of the DC cross-coupling coefficient, such as the one considered here, can lead to a strong reduction of the field intensity in Resonator 2. In contrast, the Resonator 1 resonance at 1215.20 rad/ps is spectrally far from other resonances, which minimizes the linear coupling to those other modes.

These results show that a DC can be used to achieve the spatial overlap of modes belonging to linearly uncoupled (a) or nearly-uncoupled (b) resonators. The approach is conceptually very simple and can be realized in compact structures. However, one can identify two potential problems with this implementation. The first is that the DC properties critically depend on the value of $\kappa_{\mathrm{DC}}$, which can be considered frequency independent only in a limited bandwidth, typically only a few tens of nanometers at telecom wavelengths [69]. The second is that the field distributions of the modes belonging to different resonators are in quadrature along the DC, as shown in Fig. 3.4, and thus any nonlinear interaction between them is expected to be small. In the following we introduce a different structure to overcome these limitations.

### 3.1.2. Mach-Zehnder interferometer.

We now consider the Mach-Zehnder interferometer, sketched in Fig. 3.5, which is composed of two waveguides that are connected by two point couplers (PCs). The PCs are characterized by self-coupling coefficients $\sigma_{sx}$ and $\sigma_{dx}$, and cross-coupling
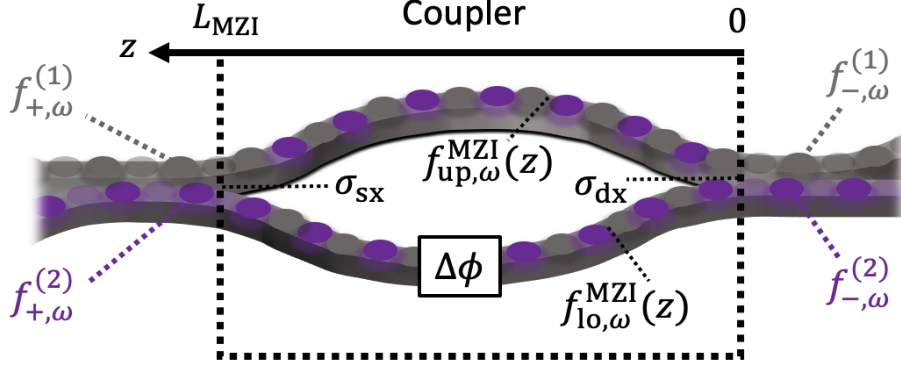
FIGURE 3.5. Sketch of the Mach-Zehnder interferometer and a schematic representation of the overlap of the fields in the channels.

coefficients $\kappa_{sx}$ and $\kappa_{dx}$, respectively. We take the coefficients to be real and positive; then from energy conservation $\sigma^2_{sx(dx)} + \kappa^2_{sx(dx)} = 1$, and the splitting ratios of the PCs are defined as $(100\sigma^2_{sx(dx)}):(100\kappa^2_{sx(dx)})$. It follows that this system can be described by the scattering matrix (1.64), with

$$X_{11} = \sigma_{sx}\sigma_{dx} - \kappa_{sx}\kappa_{dx}e^{i\Delta\phi}, \tag{3.8}$$

$$X_{12} = i\left[\sigma_{sx}\kappa_{dx} + \kappa_{sx}\sigma_{dx}e^{i\Delta\phi}\right], \tag{3.9}$$

$$X_{21} = i\left[\kappa_{sx}\sigma_{dx} + \sigma_{sx}\kappa_{dx}e^{i\Delta\phi}\right], \tag{3.10}$$

$$X_{22} = -\kappa_{sx}\kappa_{dx} + \sigma_{sx}\sigma_{dx}e^{i\Delta\phi}, \tag{3.11}$$

where $\Delta\phi$ is the optical phase difference between the two arms of the interferometer. Note that again the overall phase $e^{ik(\omega)L_{\mathrm{MZI}}}$ due to the field propagation in the interferometer is included in the fast varying component of (3.2). In practise, the interferometer acts as coupler, characterized by an effective straight-through coefficient

$$\sigma_{\mathrm{MZI}} = X_{11} = \sigma_{\mathrm{dx}}\sigma_{\mathrm{sx}} - \kappa_{\mathrm{dx}}\kappa_{\mathrm{sx}}e^{i\Delta\phi} , \tag{3.12}$$

which identifies the fraction of field amplitude in Resonator 1 that is transferred back into it. In Fig. 3.6, we show the modulus squared of $\sigma_{\mathrm{MZI}}$, in the special case of $\sigma_{dx} = \sigma_{sx} = \sigma$, for different values of $\Delta\phi$. Interestingly, when $\Delta\phi = (2m+1)\pi$ (solid black line), the coefficient $\sigma_{\mathrm{MZI}} = 1$ for any value of $\sigma$. Therefore one can exploit interference at the output of the interferometer to achieve linear uncoupling of the two resonators. The curve shows that for a symmetric interferometer this is very robust: perfect linear uncoupling is obtained as long as the PCs are identical.

We now turn to the field inside each arm of the interferometer, again described by Eq. (3.2). Here the slowly varying envelope function $f^{\mathrm{MZI}}_{\mathrm{up(lo)},\omega}(z)$ in the upper (lower)
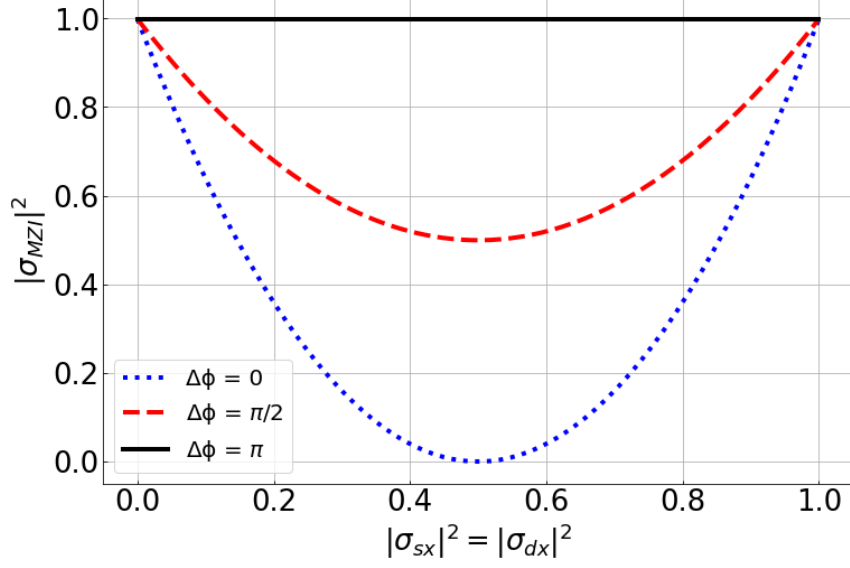
FIGURE 3.6. Effective straight-through coefficient $\sigma_{\text{MZI}}$ of the interferometer for different phases $\Delta\phi$ as function of the coupling coefficients of the two PCs assumed identical.

arm of the interferometer is $z$-independent and given by

$$
\begin{cases}
f_{\text{up},\omega}^{\text{MZI}} = \sigma_{\text{dx}} f_{-,\omega}^{(1)} + i\kappa_{\text{dx}} f_{-,\omega}^{(2)}, \\
f_{\text{lo},\omega}^{\text{MZI}} = \left[ i\kappa_{\text{dx}} f_{-,\omega}^{(1)} + \sigma_{\text{dx}} f_{-,\omega}^{(2)} \right] e^{i\Delta\phi} ,
\end{cases}
\tag{3.13}
$$

where $f_{-,\omega}^{(i)}$ is the field enhancement of the $i^{th}$ resonator, defined in eq. (1.69), and the slowly varying envelope functions at the end of the MZI in Resonator 1 and Resonator 2 are given by

$$
\begin{aligned}
f_{+,\omega}^{\text{In}} = & \left[ \sigma_{sx}\sigma_{dx} - \kappa_{sx}\kappa_{dx} e^{i\Delta\phi} \right] f_{-,\omega}^{\text{In}} + \\
& i \left[ \sigma_{sx}\kappa_{dx} + \kappa_{sx}\sigma_{dx} e^{i\Delta\phi} \right] f_{-,\omega}^{\text{Add}}
\end{aligned}
\tag{3.14}
$$

and

$$
\begin{aligned}
f_{+,\omega}^{\text{Add}} = & \left[ -\kappa_{sx}\kappa_{dx} + \sigma_{sx}\sigma_{dx} e^{i\Delta\phi} \right] f_{-,\omega}^{\text{Add}} + \\
& i \left[ \kappa_{sx}\sigma_{dx} + \sigma_{sx}\kappa_{dx} e^{i\Delta\phi} \right] f_{-,\omega}^{\text{In}} ,
\end{aligned}
\tag{3.15}
$$

respectively. We note that, unlike the DC structure, $f_{+,\omega}^{(1,2)} \neq f_{\text{up(lo)},\omega}^{\text{MZI}}(L_{\text{MZI}})$ and $f_{-,\omega}^{(1,2)} \neq f_{\text{up(lo)},\omega}^{\text{MZI}}(0)$, because of the field discontinuity introduced at each point coupler.

Although the linear uncoupling provided by the MZI is not sensitive to the splitting ratio of the PCs, as long as they are identical, this parameter plays an important

role when we focus on maximizing the nonlinear interaction. Considering the symmetry of the structure, if we assume to work in a frequency band narrow enough that the coupling can be considered frequency-independent, the best configuration would be to have PCs with a (50):(50) splitting ratio. This would lead to a splitting of both pump and generated fields in both arms of the MZI, maximizing the overlap of the fields and thus the nonlinear interaction. Instead, if the splitting ratio were (100):(0), the pump would be confined in the upper arm, while signal and idler would be in the lower arm of the interferometer. Similarly, if the splitting ratio were (0):(100), the situation would be the reverse. Thus in both cases the nonlinear interaction would vanish. In a more complicated situation, with pump, signal and idler at very different frequencies, the frequency dependence of the PCs could not be ignored, and one would have to design the structure accounting for different coupling ratios for the different fields, with the goal of directing them to the same arm of the interferometer.

One can identify two advantages of the MZI coupler over the DC. The first is that the performance of the MZI coupler is less affected than that of the DC by the frequency dependence of the coupling coefficients, and thus by the splitting ratio, since perfect linear uncoupling holds for the MZI coupler with identical PCs. So a linear uncoupling over a bandwidth of the order of hundreds of nanometers is possible in the telecom band [70]. The second advantage is a higher photon conversion efficiency for the MZI coupler than for the DC; the field distribution in each arm of the interferometer is the same as that of an isolated channel, and thus the slowly varying envelope function component is not oscillating.

### 3.2. Linear uncoupling with third-order nonlinearity

The couplers that are the focus of this chapter – the DC and the MZI coupler – fall in the category of couplers composed of two channels. Within this general framework we take $z$ to identify the propagation direction, with $x$ and $y$ being the transverse coordinates. Crucial to the calculations is the description of the overlap of the fields in the coupling region, identified by the overlap integral. This quantity, which depends on the nonlinear process under study and on the geometry of the coupling region, plays a central role in determining the efficiency of the nonlinear process. Second and third order nonlinearities have to be treated separately, because the couplers respond differently. This is because, in general, in SFWM the fields involved are around the same frequency, while with SPDC the pump field and the generated fields are spectrally distant.

**3.2.1. Comparing SFWM generation rates.** In chapter 1 we derived a general expression for the SFWM number of generated pairs per pump pulse (1.53)

$$|\beta|^2 = \frac{\hbar^2 |\alpha|^4}{8\pi^2} \frac{\gamma_{\mathrm{NL}}^2}{\omega_P^2} \int d\omega_1 d\omega_2 \, \omega_1 \omega_2 \times$$

$$\left| \int d\omega_3 \phi_P(\omega_3) \phi_P(\omega_4) \sqrt{\omega_3 \omega_4} \, \mathcal{J}(\omega_1, \omega_2, \omega_3, \omega_4) \right|^2 , \qquad (3.16)$$

where $|\alpha|^2$ is the average number of pump photons per pulse, $\gamma_{\mathrm{NL}}$ is the nonlinear power factor, $\phi_P(\omega)$ is the pump profile, and

$$\mathcal{J}(\omega_1, \omega_2, \omega_3, \omega_4) = \sum_{ch} \mathcal{J}_{ch}(\omega_1, \omega_2, \omega_3, \omega_4) \qquad (3.17)$$

is the coupler spatial integral of the $z$-dependent functions of the four fields involved in the process, where

$$\mathcal{J}_{ch}(\omega_1, \omega_2, \omega_3, \omega_4) = \int_0^{L_{ch}} dz \, f_{ch,\omega_1}^*(z) f_{ch,\omega_2}^*(z) f_{ch,\omega_3}(z) f_{ch,\omega_4}(z) e^{i\Delta k z} , \qquad (3.18)$$

is the integral in each channel of the coupler, with $\Delta k = k(\omega_1) + k(\omega_2) - k(\omega_3) - k(\omega_4)$. The shape of the field enhancement $f_{ch,\omega}(z)$ depends on the coupler under consideration. In general, eq. (3.16) needs to be evaluated numerically, but in order to calculate an explicit expression we work in the continuous wave (CW) regime by taking a narrow pump pulse $\phi_P(\omega)$ (see [71] for details), obtaining a photon pair generation rate

$$R_{\mathrm{pair}} = \frac{|\beta|^2}{\Delta T} = \frac{1}{4\pi} \left( \frac{\gamma_{\mathrm{NL}} P_P}{\omega_P} \right)^2 \int d\omega_1 \omega_1 (2\omega_P - \omega_1)$$

$$\times |\mathcal{J}(\omega_1, 2\omega_P - \omega_1, \omega_P, \omega_P)|^2 , \qquad (3.19)$$

where $P_P = \hbar \omega_P |\alpha|^2 / \Delta T$ is the injected pump power and $\Delta T$ the pump temporal duration, taken to go to infinity along with the average number of pump photons in the pulse so that $P_P$ is held constant. We can estimate the pairs production rate for each structure once the expression of the overlap integral is evaluated. Again, in general the integral in (3.19) needs to be evaluated numerically, but with the approximation of Lorentzian shape of the intensity enhancement, described by eq. (1.71), we can write an analytic expression for the pair generation rate. In fact, with this approximation the integral (3.18) for a single channel can be written as

$$|\mathcal{J}(\omega_1, 2\omega_P - \omega_1, \omega_P, \omega_P)|^2 = |\mathcal{F}_{\mathrm{max}}|^2 \mathcal{L}(\omega_1, 2\omega_P - \omega_1) |\mathcal{J}_{\mathrm{spatial}}|^2 , \qquad (3.20)$$

where

$$|\mathcal{F}_{\max}|^2 = |\mathrm{FE}_{(\max)2,S}|^2 |\mathrm{FE}_{(\max)2,I}|^2 |\mathrm{FE}_{(\max)1,P}|^4 \ , \tag{3.21}$$

is the product of the maximum values of the intensity enhancement in Resonators 1 and 2 of each resonance involved in the process, given by eq. (1.72),

$$\mathcal{L}(\omega_1, 2\omega_P - \omega_1) = \left[ \frac{\frac{\Gamma_{2,S}^2}{4}}{\frac{\Gamma_{2,S}^2}{4} + (\omega_1 - \omega_S)^2} \frac{\frac{\Gamma_{2,I}^2}{4}}{\frac{\Gamma_{2,I}^2}{4} + (\omega_1 - \omega_S)^2} \right] + $$
$$\left[ \frac{\frac{\Gamma_{2,S}^2}{4}}{\frac{\Gamma_{2,S}^2}{4} + (\omega_1 - \omega_I)^2} \frac{\frac{\Gamma_{2,I}^2}{4}}{\frac{\Gamma_{2,I}^2}{4} + (\omega_1 - \omega_I)^2} \right] \tag{3.22}$$

is the product of the Lorentzian shape of the signal and idler resonances centered at $\omega_S$ and $\omega_I$ respectively. Here $\Gamma_{2,m=S,I}$ is given by eq. (1.74), while the absolute value squared of the pump shape is assumed to be proportional to a Dirac delta function, given the CW regime; $\mathcal{J}_{\mathrm{spatial}}$ is the spatial part of the integral, which depends only on the geometry of the system. We can perform the integral over the frequency-dependent factor, common for all the possible geometries, which results in (see appendix A for detailed calculation)

$$\int d\omega_1 \omega_1 (2\omega_P - \omega_1) \mathcal{L}(\omega_1, 2\omega_P - \omega_1) \approx \pi \frac{\Gamma_{2,S}\Gamma_{2,I}}{(\Gamma_{2,S} + \Gamma_{2,I})} (\omega_S \omega_I) \ . \tag{3.23}$$

With this in hand, we can write (3.19) as

$$R_{\mathrm{pair}} = \frac{1}{4\pi} \left( \frac{\gamma_{\mathrm{NL}} P_P}{\omega_P} \right)^2 |\mathcal{F}_{\max}|^2 \pi \frac{\Gamma_{2,S}\Gamma_{2,I}}{(\Gamma_{2,S} + \Gamma_{2,I})} (\omega_S \omega_I) |\mathcal{J}_{\mathrm{spatial}}|^2 \ . \tag{3.24}$$

The expression for $\mathcal{J}_{\mathrm{spatial}}$ needs to be evaluated for each structure. In the following this we do and then compare our results for the DC and MZI coupling structures with that of a standard ring resonator, assuming in all calculations that we satisfy the phase matching condition, $\Delta k = 0$, to good approximation.

3.2.1.1. *Ring resonator.* In the case of a simple ring resonator of length $L = 2\pi R$, the spatial integral is

$$\mathcal{J}_{\mathrm{spatial}}^{\mathrm{ring}} = \int_0^L e^{i\Delta k z} dz = L e^{i\frac{\Delta k L}{2}} \mathrm{sinc}\left( \frac{\Delta k L}{2} \right) \approx L \ , \tag{3.25}$$

and hence the generation rate (3.24) is

$$
\begin{aligned}
R_{\text{pair}}^{\text{ring}} =& |\text{FE}_{(\text{max}),S}|^2 |\text{FE}_{(\text{max}),I}|^2 |\text{FE}_{(\text{max}),P}|^4 \\
& \times \left( \frac{\gamma_{\text{NL}} P_P}{\omega_P} \right)^2 \frac{\Gamma_S \Gamma_I}{(\Gamma_S + \Gamma_I)} (\omega_S \omega_I) \frac{L^2}{4} \quad,
\end{aligned}
\tag{3.26}
$$

with $\Gamma_{m=S,I}$ the linewidth of the signal and idler resonances. This can be expressed as a function of the loaded and coupling quality factors ($Q_m$ and $Q_{C,m}$ respectively) using $\Gamma_m = \omega_m / Q_m$ and

$$
|\text{FE}_{(\text{max}),m}|^2 = \frac{1 - \sigma_m^2}{(1 - \sigma_m a_m)^2} = \frac{4 v_g}{L \omega_m} \frac{Q_m^2}{Q_{C,m}} \quad,
\tag{3.27}
$$

from [67], giving

$$
\begin{aligned}
R_{\text{pair}}^{\text{ring}} =& \left( \frac{\gamma_{\text{NL}} P_P}{\omega_P} \right)^2 \left( \frac{4 v_g}{L} \right)^4 \frac{Q_P^4 Q_S^2 Q_I^2}{Q_{C,P}^2 Q_{C,S} Q_{C,I}} \frac{\omega_S \omega_I}{\omega_P^2} \frac{L^2/4}{\omega_S Q_I + \omega_I Q_S} \\
=& \frac{4^3 \gamma_{\text{NL}}^2 P_P^2 v_g^4 \omega_S \omega_I}{L^2 \omega_P^4 (\omega_S Q_I + \omega_I Q_S)} \frac{Q_P^4 Q_S^2 Q_I^2}{Q_{C,P}^2 Q_{C,S} Q_{C,I}} \quad.
\end{aligned}
\tag{3.28}
$$

We assume to work over a frequency range small enough that we can take $\omega_P \approx \omega_S \approx \omega_I = \omega$ and $Q_P \approx Q_S \approx Q_I = Q$, which allows us to reduce (3.26) to a simplified form. For no losses ($Q_{C,m} = Q_m$), we find

$$
R_{\text{pair}}^{\text{ring}} = (\gamma_{\text{NL}} P_P)^2 \frac{32 v_g^4}{\omega^3} \frac{Q^3}{L^2} \quad,
\tag{3.29}
$$

retrieving the SFWM generation rate expression found earlier [25], while for critical coupling ($Q_{C,m} = 2 Q_m$) we find

$$
R_{\text{pair}}^{\text{ring}} = (\gamma_{\text{NL}} P_P)^2 \frac{2 v_g^4}{\omega^3} \frac{Q^3}{L^2} \quad.
\tag{3.30}
$$

3.2.1.2. *Directional Coupler.* If we consider the DC structure and assume perfect uncoupling in the linear regime, the spatial integral is in the form of (detailed calculation in appendix A)

$$
\mathcal{J}_{\text{spatial}} \approx -\frac{L_{\text{DC}}}{4} \left[ 1 - \text{sinc}(4 \kappa_{\text{DC}} L_{\text{DC}}) \right] \quad,
\tag{3.31}
$$

which lead to a generation rate of

$$
\begin{aligned}
R_{\text{pair}}^{\text{DC}} =& \left( \frac{\gamma_{\text{NL}} P_P}{\omega_P} \right)^2 |\text{FE}_{(\text{max})2,S}|^2 |\text{FE}_{(\text{max})2,I}|^2 |\text{FE}_{(\text{max})1,P}|^4 \\
& \times \frac{\Gamma_{2,S} \Gamma_{2,I}}{\Gamma_{2,S} + \Gamma_{2,I}} (\omega_S \omega_I) \frac{L_{\text{DC}}^2}{64} \left[ 1 - \text{sinc}(4 \kappa_{\text{DC}} L_{\text{DC}}) \right]^2 \quad.
\end{aligned}
\tag{3.32}
$$

Again, we can express this formula in terms of quality factors, and find

$$R_{\text{pair}}^{\text{DC}} = \frac{4\gamma_{\text{NL}}^2 P_P^2 v_g^4 \omega_S \omega_I}{\omega_P^4 (\omega_S Q_I + \omega_I Q_S)} \frac{Q_P^4 Q_S^2 Q_I^2}{Q_{C,P}^2 Q_{C,S} Q_{C,I}}$$

$$\times \left(\frac{L_{\text{DC}}}{L_1 L_2}\right)^2 [1 - \text{sinc}(4\kappa_{\text{DC}} L_{\text{DC}})]^2 \ . \tag{3.33}$$

3.2.1.3. *Mach-Zehnder Interferometer.* For the MZI coupler structure with perfect uncoupling in the linear regime, taking $\sigma_{\text{dx}} = \sigma_{\text{sx}} = 1/\sqrt{2}$, i.e. (50):(50) beam splitters, the spatial integral results in

$$\mathcal{J}_{\text{spatial}} \approx -\frac{L_{\text{MZI}}}{2} \ , \tag{3.34}$$

(detailed calculation in appendix A), which leads to a generation rate of

$$R_{\text{pair}}^{\text{MZI}} = \left(\frac{\gamma_{\text{NL}} P_P}{\omega_P}\right)^2 |\text{FE}_{(\text{max})2,S}|^2 |\text{FE}_{(\text{max})2,I}|^2$$

$$\times |\text{FE}_{(\text{max})1,P}|^4 \frac{\Gamma_{2,S} \Gamma_{2,I}}{\Gamma_{2,S} + \Gamma_{2,I}} (\omega_S \omega_I) \frac{L_{\text{MZI}}^2}{16} \ , \tag{3.35}$$

and in terms of quality factors

$$R_{\text{pair}}^{\text{MZI}} = \frac{16 v_g^4 \gamma_{\text{NL}}^2 P_P^2 \omega_S \omega_I}{\omega_P^4 (\omega_S Q_I + \omega_I Q_S)} \frac{Q_P^4 Q_S^2 Q_I^2}{Q_{C,P}^2 Q_{C,S} Q_{C,I}} \left(\frac{L_{\text{MZI}}}{L_1 L_2}\right)^2 \ . \tag{3.36}$$

3.2.1.4. *Comparison.* We can have a better insight of the generation efficiency of our two structures if we directly compare it with the ring resonator. For the DC structure, the sinc function in (3.32) makes a negligible contribution for our typical parameters of interest, and we can write

$$R_{\text{pair}}^{\text{DC}} \approx \left(\frac{L L_{\text{DC}}}{4 L_1 L_2}\right)^2 R_{\text{pair}}^{\text{ring}} \ , \tag{3.37}$$

and assuming $L_1 = L_2 = 2L$, which means having two racetracks with the same bending radius of the ring, and taking the optimal length of the DC, i.e., $L_{\text{DC}} = \pi R$ as shown in [67], the expression becomes

$$R_{\text{pair}}^{\text{DC}} \approx \frac{1}{1024} R_{\text{pair}}^{\text{ring}} \ . \tag{3.38}$$

We can do the same calculations for the MZI structure, where

$$R_{\text{pair,ext}}^{\text{MZI}} \approx \left(\frac{L L_{\text{MZ}}}{2 L_1 L_2}\right)^2 R_{\text{pair}}^{\text{ring}} \ , \tag{3.39}$$

and assuming $L_1 = L_2 = 2L$ and $L_{\text{MZ}} = \pi R$ we get

$$R_{\text{pair}}^{\text{MZI}} \approx \frac{1}{256} R_{\text{pair}}^{\text{ring}} \ . \tag{3.40}$$
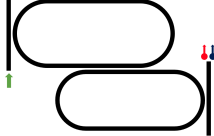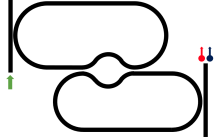
| Structure | Spatial integral | Overall finesse factor | Pair generation rate |
|---|---|---|---|
|  | $\mathcal{J}_{\text{spatial}}^{\text{ring}} \approx L$ | $\mathcal{F} \propto (L)^{-4}$ | $R_{\text{pair}}^{\text{ring}}$ (3.28) |
|  | $\mathcal{J}_{\text{spatial}}^{\text{DC}} \approx \frac{1}{4}L_{\text{DC}}$ | $\mathcal{F} \propto (L_1 L_2)^{-2}$ | $\frac{1}{1024}R_{\text{pair}}^{\text{ring}}$ (3.38) |
|  | $\mathcal{J}_{\text{spatial}}^{\text{MZI}} \approx \frac{1}{2}L_{\text{MZI}}$ | $\mathcal{F} \propto (L_1 L_2)^{-2}$ | $\frac{1}{256}R_{\text{pair}}^{\text{ring}}$ (3.40) |

TABLE 3.1. Rate comparison between the ring resonator, the DC-resonator and the MZI-resonator. The other quantities of interest are the spatial integral and the resonators' finesse.

An overview of our estimates is reported in Table 3.1, along with the main quantities of interest of each structure. Although these two rates are substantially reduced from that of the standard ring, the significant benefit obtained is that we can implement independent control on each comb of resonances, and achieve several dB of pump filtering from the generated fields.

### 3.2.2. SFWM and DC structure.

The first situation we want to address is DP-SFWM in the double-racetrack resonators structure where the coupling is realized through the DC. As we already described in chapter 2, the major problem with DP-SFWM are the parasitic processes. Before, we exploited strong coupling to selectively remove target resonances and suppress those processes. To study this, we first show in Fig. 3.7 the photon generation rates due to the DP-SFWM and SP-SFWM processes in an integrated silicon microring resonator (like the one sketched in Fig. 2.6). As expected, the generation rate for the DP-SFWM is unchanged as long as the product of the two pump powers is held fixed, while the generation rate of the SP-SFWM processes scales quadratically with the appropriate pump powers [25]. The generation rates of the parasitic processes, given by the sum of the two SP-SFWM rates, can be even one order of magnitude larger than the generation rate of the DP-SFWM process, with a maximum signal-to-noise ratio (SNR) of only about 2 when the two pump powers are equal.

Here, we show how with the advantage of the linear uncoupling strategy we can move the position of the resonances we're interested in, and place them in the right configuration to allow for the dual-pump to occur, eliminating the parasitic processes. With the two-racetracks system, we can tune the two independent sets of resonances
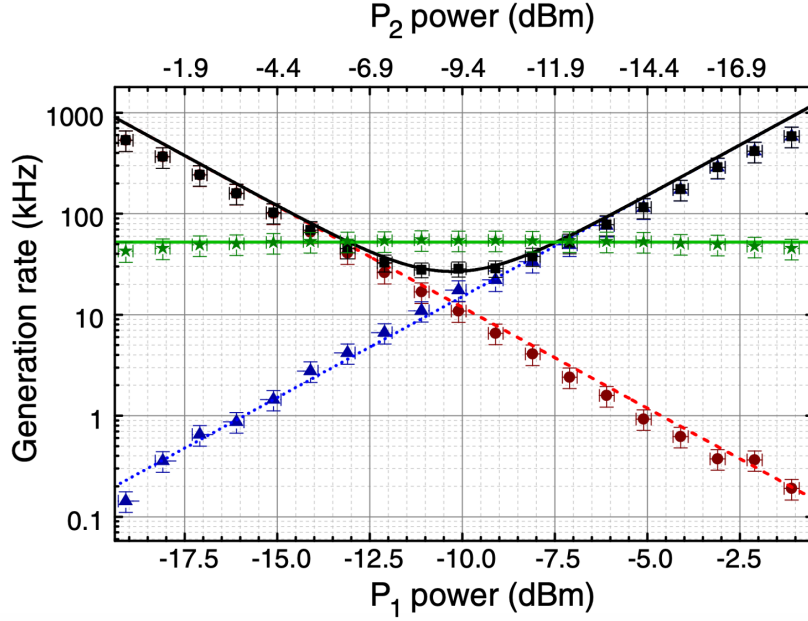
FIGURE 3.7. Measurement and theoretical model of the pair generation rate in a single silicon microring resonator when the product of the powers of the two pumps is fixed for SP-SFWM pumped at $\omega_{P_1}$ (blue triangles and line) and $\omega_{P_2}$ (red circles and line), their sum (black squares and line), and DP-SFWM (green stars and line) (image taken from [69]).

to selectively enhance or suppress different nonlinear phenomena. In Fig. 3.8 we represent a sketch of the realization of DP-SFWM in such a system. Two laser pumps are tuned to resonances of the first resonator, leading to the generation of photon pairs within a target resonance of the second resonator. Yet SP-SFWM processes are expected to be suppressed, for the overall field enhancement at $\omega_{X_1} = 2\omega_{P_1} - \omega_S$ and $\omega_{X_2} = 2\omega_{P_2} - \omega_S$ is strongly reduced by the absence of the three resonances satisfying energy conservation.

We had the possibility to actually fabricate the designed structure and to perform the experiment o the collaboration with the experimental group at the University of Pavia and at CEA-LETI in Grenoble (FR). The device is presented in Fig. 3.9(a): two Silicon racetrack resonators, with a waveguide cross section of $600\,\mathrm{nm} \times 220\,\mathrm{nm}$ to optimize the nonlinear effective area [72] and minimize propagation losses, with lengths $L_1 = 372\,\mu\mathrm{m}$ and $L_2 = 366\,\mu\mathrm{m}$, are located side by side, forming a DC of length $L_{\mathrm{DC}} = 92\,\mu\mathrm{m}$, chosen to minimize cross transmission and achieve isolation of the two resonators. Thus, one set of modes is associated with Resonator 1, and another with Resonator 2. In Fig. 3.9(b) we show the optical characterization, where the two independent sets of resonances are clearly observed by injecting light from a laser in ports $T_1$ or $T_2$ and detecting the optical response at the ports $T_6$ and $T_3$, respectively. The free spectral ranges at $1550\,\mathrm{nm}$ are $\mathrm{FSR}_1 \simeq 1.566\,\mathrm{nm}$ and $\mathrm{FSR}_2 \simeq 1.595\,\mathrm{nm}$. The loaded quality factors are around $6 \times 10^4$ and $3 \times 10^5$, with
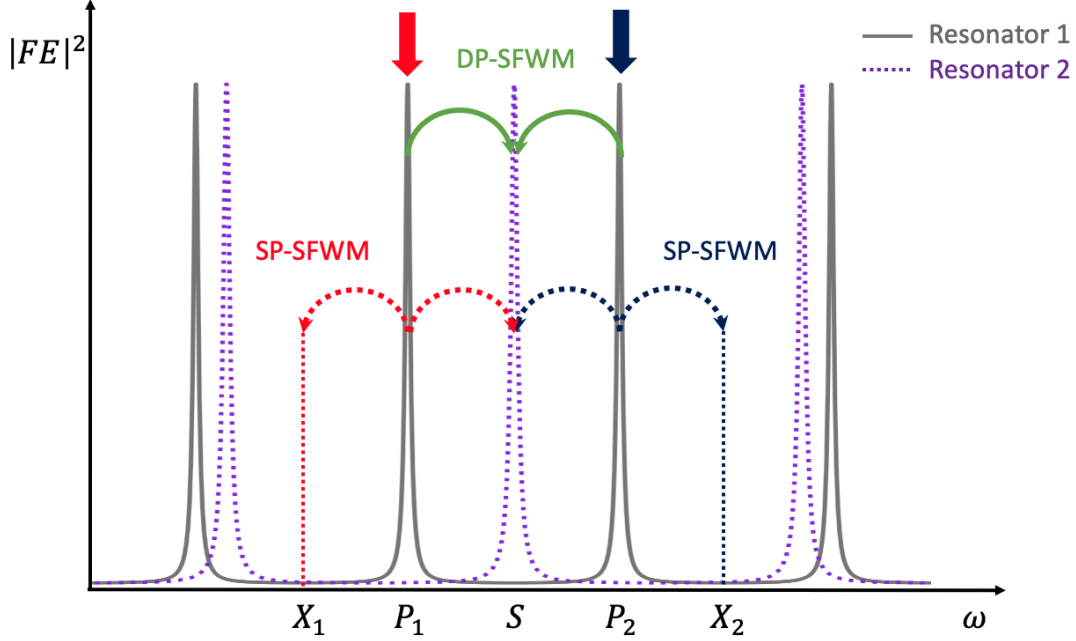
FIGURE 3.8. Sketch of the SP-SFWM and DP-SFWM processes occurring in the device when two laser pumps are aligned with two resonances ($P_1$ and $P_2$). Single-pump processes which generate photons in the $S$ mode are suppressed due to the weak field enhancement experienced at the spectral position where energy conservation is preserved ($X_1$ and $X_2$).

the difference due to the number of waveguides coupled to the racetracks (two to Resonator 1 and one to Resonator 2), which have the same intrinsic quality factors of about $6 \times 10^5$. The optical isolation is at least $20\,\mathrm{dB}$ over a 40-nm bandwidth, as observed from the transmission spectrum $\mathrm{T}_1 \to \mathrm{T}_3$.

We now consider the $S$ mode, where photons can be generated through SP-SFWM only if another photon is generated to guarantee the conservation of energy. In particular, if the resonance at $\omega_{P_1}$ is pumped by the laser, it can generate a photon pair with one photon at $\omega_S$ and one at $\omega_{X_1}$, such that $\omega_{X_1} = 2\omega_{P_1} - \omega_S$. A similar argument holds for photons generated at $\omega_{X_2}$ when pumping at $\omega_{P_2}$. Thanks to the linear uncoupling, the two sets of resonances can be controlled independently, allowing us to remove the resonances from $X_1$ and $X_2$. In practice, this control is achieved by means of two electric heaters. We begin by verifying the capability of our structure to suppress SP-SFWM. To do that, we calculate the variation of the efficiency of the process by tuning the two sets of resonances, which leads to a modification of the nonlinear coupling of the modes. We start by considering one pump resonance of Resonator 1 in the middle of two resonances of Resonator 2. This configuration guarantees the maximum efficiency for the SP-SFWM. Then, we detune the comb of Resonator 1 by a certain amount and calculate the generation rate at each step (Fig. 3.10(a)). Experimentally, this is realized by adjusting the driving voltage of
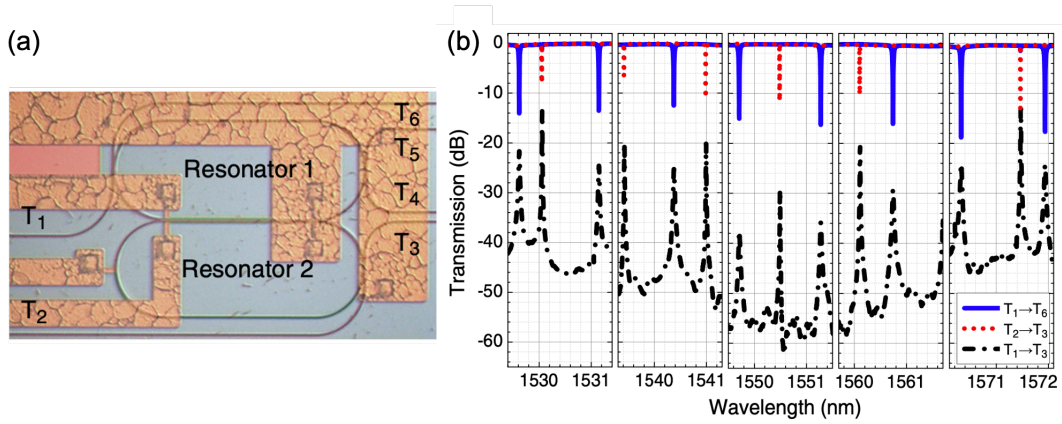
FIGURE 3.9. (a) Optical image of the device with two linearly uncoupled racetracks. A second image of the device without the electrical circuits has been superimposed to show the position of waveguides, which are covered by the metal. (b) Linear characterization of the device over different ranges of wavelengths for different in and out ports configurations (images taken from [69]).

the heater of Resonator 1 to shift its resonances, by tuning the pumping laser to maintain the alignment, and by collecting the coincidences from the two resonances of Resonator 2. The result is shown in Fig. 3.10(b), where with the solid red line we plot the model for the generation rate derived in eq. (3.32) (normalized to its maximum) that fits the data (black crosses) measured in the experiment. This result shows that by tuning the two sets of resonances one can manipulate the nonlinear coupling of the modes of the resonators and, consequently, the generation of pairs due to the nonlinear processes occurring in the device. In the experiment, a detuning of around 65 pm (around 13 times the linewidth of the resonances of Resonator 2) led to a suppression of around three orders of magnitude with respect to perfect nonlinear coupling.

With the possibility of attenuating the parasitic processes demonstrated, we were able to perform the dual-pump SFWM experiment. The laser pumps are aligned with two resonances of Resonator 1 ($\omega_{P_1} = 1206.89 \, \text{rad/ps}$ and $\omega_{P_2} = 1222.85 \, \text{rad/ps}$), which are equally spaced in frequency from the resonance $\omega_S = 1214.88 \, \text{rad/ps}$ of Resonator 2. This configuration is associated with a detuning of the resonances for the single-pump process of about $|\delta| = 160 \, \text{pm}$, that results in an estimated attenuation of the SP-SFWM processes of about $-37.7 \, \text{dB}$, that is below the background noise. Photons generated in the $S$ mode are sent to a (50):(50) beam splitter and detected by two photodetectors ($D_1$ and $D_2$, respectively), while photons associated with SP-SFWM are collected from mode $X_1$ and $X_2$ and detected by two others photodetectors ($D_3$ and $D_4$, respectively). The analysis of the coincidences on the detectors allows for the recognition of the pairs generated through the different processes. In particular, the DP-SFWM should lead to a temporal correlation between

the detection events at $D_1$ and $D_2$. Similarly, the single-pump processes should result in coincident detection between the events at $D_3$ and $D_1/D_2$ for single-pump in mode $P_1$, and the events at $D_4$ and $D_1/D_2$ for single-pump in mode $P_2$. We show the result of the coincidence experiment in Fig. 3.11. The red peak shows that photons arriving on $D_1$ and $D_2$ are emitted at the same time since their arrival time is correlated: this clearly demonstrates that they are emitted through DP-SFWM since any other process that can generate photons in the $S$ mode cannot be characterized by this temporal correlation. We measure a coincidence rate equal to $164.2 \pm 0.4\,\mathrm{Hz}$, which corresponds to an internal generation rate in the second resonator equal to $62 \pm 6\,\mathrm{kHz}$, and the coincidence to accidental ratio (CAR) is $1190 \pm 10$. The coincidence rate is estimated by integrating the peak within the entire window (and subtracting the noise), while the CAR is measured by taking into account the FWHM of the peak. From the histograms in Fig. 3.11 it is also possible to evaluate the photon pairs generated through SP-SFWM, which lead to coincidence events between $D_1$ and $D_2$ with $D_3$ or $D_4$. As can be seen, no peaks are clearly visible. In fact, the dark counts, the noise from the environment, and other parasitic processes occurring in the setup (such as Raman emission from optical fibers) hide the signal given by time-correlated photons. This is due to the severe attenuation of the processes. Nevertheless, we can estimate from the model that we should expect a SNR of about $21 \times 10^3$, corresponding to an improvement of about four orders of magnitude over that of a single ring system where dispersion engineering cannot be exploited. While the effectiveness of this strategy depends on the specific application and the technological platform, this is one of the strongest suppression of parasitic processes reported in the literature for DP-SFWM in an integrated structure.
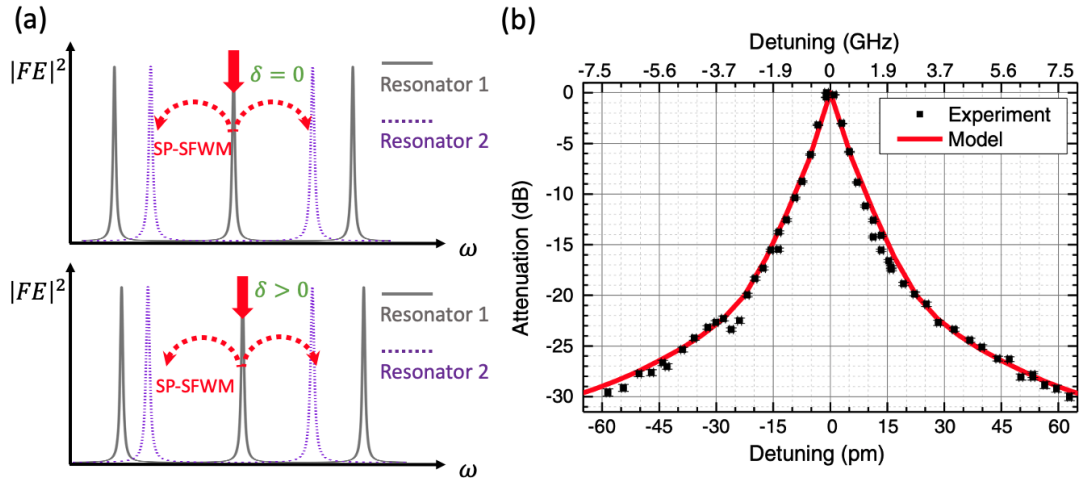


FIGURE 3.10. (a) Scheme of the single pump process with the aligned resonances configuration (top) and detuned configuration (bottom). (b) Plot showing the attenuation of SP-SFWM as a function of the detuning of the resonances of the two resonators (image taken from [69]).
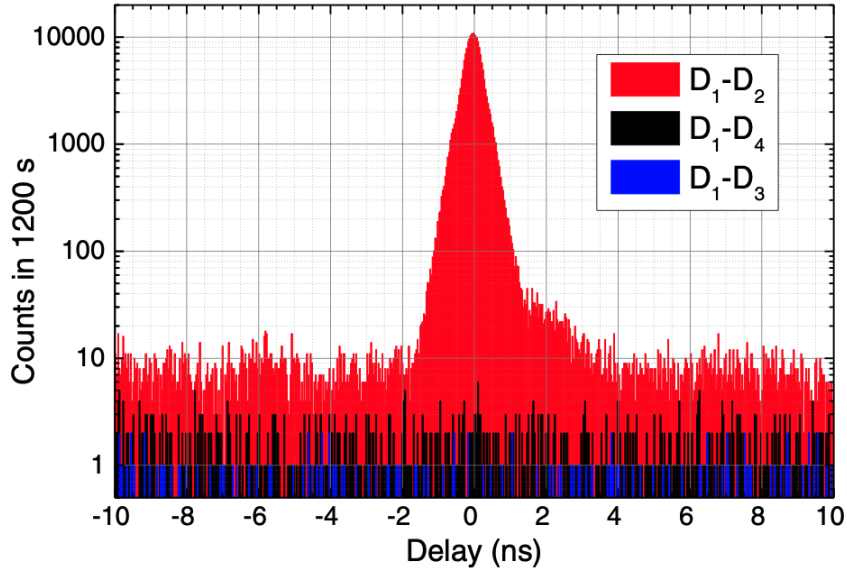
FIGURE 3.11. Histograms representing the coincidence events detected. The red, black, and blue histograms represent the coincidences due to DP-SFWM (events on $D_1$ and $D_2$), SP-SFWM on mode $P_2$ (events on $D_1$ and $D_4$), and SP-SFWM on $P_1$ (events on $D_1$ and $D_3$), respectively (image taken from [69]).

These results demonstrate that the use of linearly uncoupled resonators allows for the effective control of the nonlinear interaction between optical modes, leading to the ability to enhance or suppress the generation of photon pairs through SFWM. As already mentioned in the DC section (and clearly pointed out in [67]), the efficiency of the parametric process in this kind of devices is reduced from what could be achieved with a simple microring since here the nonlinear interaction occurs only in the directional coupler region shared by the two rings. This decreases both the overlap integral of the fields and the interaction length. This would be a limitation in the framework of squeezed-light sources, where high generation efficiency is required. However, a small interaction length and material nonlinearity can be compensated for by taking advantage of the field enhancement in high-quality resonators, and by increasing the pump intensity in the absence of nonlinear losses, as in $Si_3N_4$ resonators [73, 74]. This device is anyway a promising platform for the implementation of continuous-variable quantum computing, since the main sources of noise, due to SP-SFWM, can be effectively suppressed. With the experiment, we could test the model and confirm the achievement of a SNR of about four orders of magnitude.

**3.2.3. SFWM and MZI structure.** Although the linearly uncoupled resonators with the DC can provide a quite compact system that greatly suppresses parasitic processes, the design and fabrication of such systems can be challenging, for in a DC the splitting ratio critically depends on its length and on the distances between the
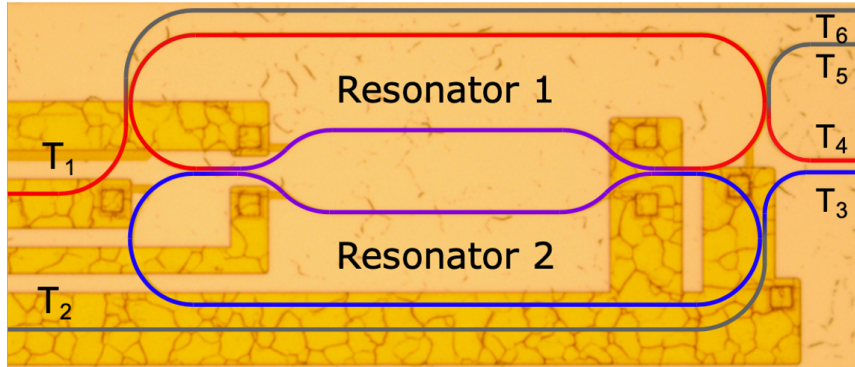
FIGURE 3.12. Optical image of the device composed of two resonators placed side-by-side forming a Mach-Zehnder interferometer. The optical waveguides of the device, which are partially covered by the metal circuits, have been highlighted with coloured lines: the region where the optical modes propagate are highlighted in red for Resonator 1 and in blue for Resonator 2, while the purple line highlights the section where the nonlinear interaction takes place (image taken from [70]).

two waveguides. In addition, the DC response is usually frequency dependent, with the desired behavior achieved in a limited bandwidth, typically a few tens of nanometers at telecom wavelengths [69]. Moreover, the generation efficiency compared to what one usually obtains with a standard ring resonator is considerably reduced. The reasons are the shorter interaction length and the smaller overlap integral in the interaction region. We then look for a strategy to improve the generation efficiency. One could think of increasing the length of the coupler to enhance the nonlinear interaction, but it was calculated that, for SFWM, the length of the DC has an optimum value, which depends on the overall length of the resonator [67]. Thus, we can move to a different strategy and explore the potential of the uncoupling through a MZI. In fact, as we discussed earlier, the fields propagation in the two arms of the interferometer is that of an isolated channel waveguide, hence it does not suffer from the field profile oscillation. This solution can provide significant improvements in terms of linear isolation of the two resonators, operation bandwidth, and SFWM efficiency.

We had the chance to perform the experiment on this structure as well. The fabricated device is shown in Fig. 3.12, realized by placing the two racetrack resonators side-by-side to form the MZI. The couplers at the beginning and at the end of the interferometer are realized with two identical directional couplers (DCs) with proper length and distance to get a (50):(50) splitting ratio. The phase difference introduced by the MZI is obtained by designing the two arms of the interferometer with two different lengths, and can be calculated as

$$\Delta\phi = k\Delta L_{\text{MZI}} \ , \tag{3.41}$$

where $\Delta L_{\text{MZI}}$ is the MZI path difference and $k = \omega_0 n_{\text{eff}}/c + \Delta\omega/v_g$ the wavevector, considering only the linear term in the expansion (1.60), where we call $\Delta\omega = \omega - \omega_0$

the bandwidth. A fine tuning on the value of $\Delta\phi$ is obtained by means of an electrical heater. As previously discussed, when $\Delta\phi = (2m+1)\pi$, with $m$ integer, light entering from the upper (lower) MZI input port is entirely redirected to the upper (lower) output port, so that the two racetracks are perfectly linearly uncoupled. We recall that the (50):(50) splitting ratio is not crucial in obtaining the uncoupling as long as the two DCs are identical and the phase is $\Delta\phi = (2m+1)\pi$ (Fig. 3.6). However, it is the best configuration to work with when the resonances involved in the process are about the same frequency, in order to maximize the conversion efficiency. The reason is again the frequency-dependent behavior of the DCs forming the MZI. In the situation of very distant resonances, when each field couples at a different rate than the others, one should engineer the couplers to direct the fields necessary to the process into the same arm of the interferometer.

The first advantage we get from exploiting the MZI structure is the larger linear isolation bandwidth. This can be calculated from equation (3.12), with $\Delta\phi$ given by eq. (3.41). If one works at the shortest useful path difference, which corresponds to $\Delta\phi = \pi$, in a single-mode silicon waveguide, with $\omega_0 = 1215\,\mathrm{rad/ps}$ ($\lambda_0 = 1550\,\mathrm{nm}$), $n_{\mathrm{eff}} = 2.4$, and $n_g = 4$, one can expect a MZI straight transmission of more that 99% over a bandwidth of around $50\,\mathrm{rad/ps}$ ($\approx 190\,\mathrm{nm}$), where for the DCs we assumed



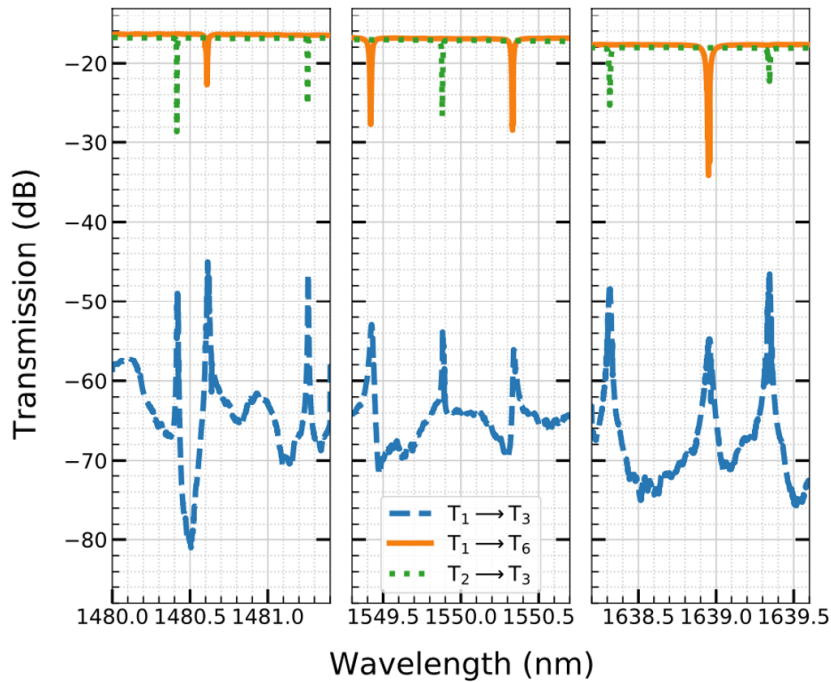FIGURE 3.13. Linear characterization of the device in three selected spectral ranges. The transmission $T_1 \to T_6$ is plotted with solid orange line and the transmission $T_2 \to T_3$ with dotted green line, allowing one to observe the resonances associated to the two resonators. The dashed blue line is obtained by characterizing the device through $T_1 \to T_3$ transmission (image taken from [70]).

the coupling coefficients $\sigma_{dx} = \sigma_{sx} = \cos(\kappa_{DC}L_{DC}) = 1/\sqrt{2}$. The second advantage is the higher generation rate following from the fields distribution inside the coupler. As shown in section 3.2.1, where we compared the rate in the different structures, the generation efficiency gains a factor of 4 with respect to the DC case.

The experiment was conducted on a device fabricated from a silicon-on-insulator silica-cladded waveguide having a cross section of $600 \times 220\,\mathrm{nm}^2$, chosen to minimize the nonlinear effective area and, at the same, the propagation losses. The two resonators have lengths $L_1 = 639\,\mu\mathrm{m}$ and $L_2 = 632\,\mu\mathrm{m}$, and the DCs have a (50):(50) splitting ratio. The two arms of the interferometer have lengths $L_{A1} = 194\,\mu\mathrm{m}$ and $L_{A2} = 194.25\,\mu\mathrm{m}$ to guarantee the linear isolation of the resonators near 1550 nm and to maximize the operation bandwidth, as discussed above. To assess the presence of the modes associated to the two resonators, we performed a linear characterization of the device, shown in Fig. 3.13, by injecting light from a CW tunable laser into ports $T_1$ and $T_2$ of the sample, and detecting the optical response at ports $T_6$ and $T_3$, shown with solid orange and dotted green lines, respectively. The two sets of
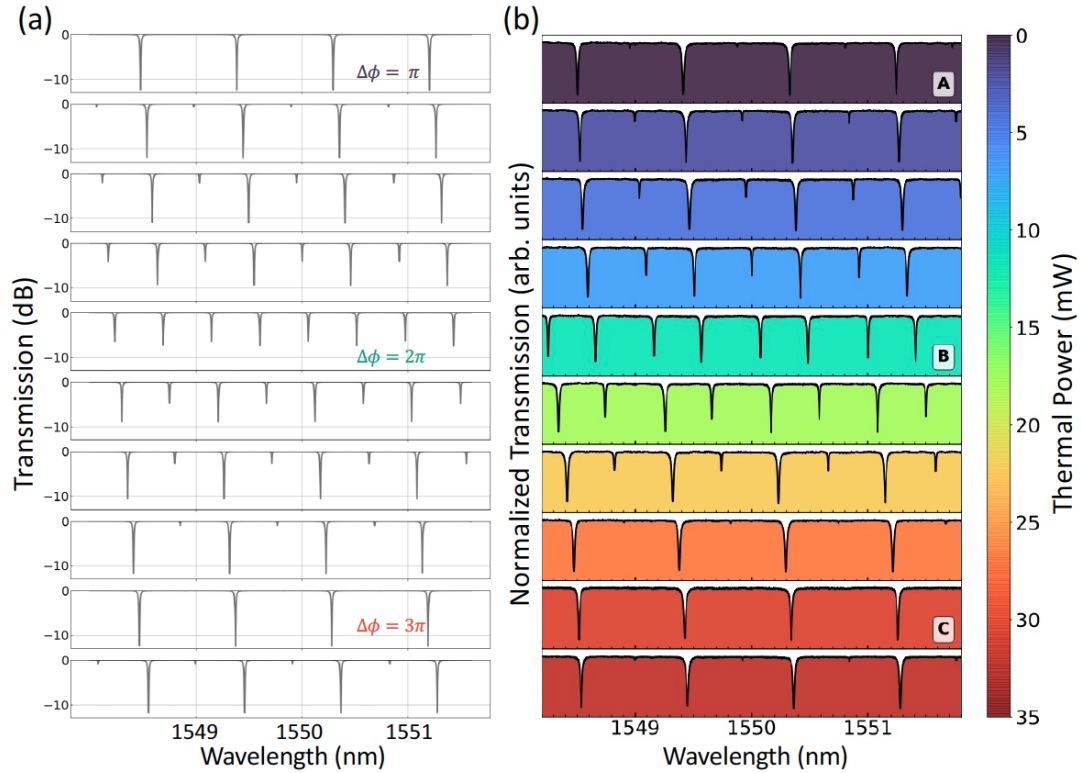


FIGURE 3.14. (a) Plot of the simulated transmission spectra of Resonator 1 (from port $T_1$ to port $T_6$) for different values of the phase $\Delta\phi$ introduced by the MZI. (b) Experimental plots of the spectra obtained by coupling the laser to port $T_1$ and collecting the light from port $T_6$. Each panel is associated with a different value of the voltage applied to the heater on top of one arm of the Mach-Zehnder (image taken from [70]).

resonances (having different FSRs and finesse) can be clearly observed. Then, we evaluated the coupling between the resonators. To do that, we injected the light to port $T_1$ while measuring the response at $T_3$, plotted with the blue dashed line. We performed the characterization over the full bandwidth of the tunable laser source (from 1480 nm to 1640 nm, covering the C- and L-band and part of the S- band), proving that an isolation of more than 30 dB can be achieved over the whole range ($\approx 160$ nm). This demonstrates the significant improvement with respect to previous results obtained with directional coupler's isolation, where the bandwidth was about only tens of nanometers.

We also studied the control on the coupling by tuning the MZI phase thanks to the thermal heater; the results are plotted in Fig. 3.14. By adjusting the phase difference $\Delta\phi$ we can switch from the linear uncoupled situation to a strong coupled system. In fact, from the simulation of the transmission spectra from port $T_1$ to port $T_6$ of Resonator 1, plotted in Fig. 3.14(a), we can see that for $\Delta\phi = \pi$ and $\Delta\phi = 3\pi$ only the comb of resonances belonging to Resonator 1 is visible; this means that no light is coupled into Resonator 2. Conversely, for $\Delta\phi = 2\pi$ the two resonators are maximally coupled, and the visible spectrum is that of a resonator with a total length $L_{\text{tot}} = L_1 + L_2$. This behavior is reproduced also experimentally (Fig. 3.14(b)), where 15 mW of electrical power are sufficient to switch from the configuration with no coupling (panels A and C) to that with maximally-coupled resonators (panel B).

In Fig. 3.15 we studied the pair generation efficiency, plotting the rate as a function of the optical pump power. The orange dotted line results from the theoretical model (3.36), when considering the nominal parameters of the structure and the resonant quality factor obtained from the linear characterization [75]. We also characterized the nonlinearity of the device by performing a SFWM experiment. First, we adjusted the position of the resonances of Resonator 2, by means of the corresponding heater, such that two resonances (signal and idler) of Resonator 2 are equally spaced in frequency with respect to a resonance (pump) of Resonator 1 (following the scheme depicted in Fig. 3.10(a), top panel). In this condition, due to the nonlinear interaction occurring in the MZI, triply resonant SFWM can take place, by pumping the device with a CW laser through port $T_1$, tuned at the pump resonant frequency, and detecting the coincidence rate of the generated signal and idler photons in port $T_3$. The data are obtained from the measured coincidence rate by taking into accounts the linear losses of the set-up and the detection efficiency of the detectors. The data are in very good agreement with the theory and, as expected, the generation rate grows quadratically with the pump power. The measured generation rate is lower than the theoretical value when the pump power exceeds 1 mW. This is likely due to two-photon absorption [76], which has not been included in our model.
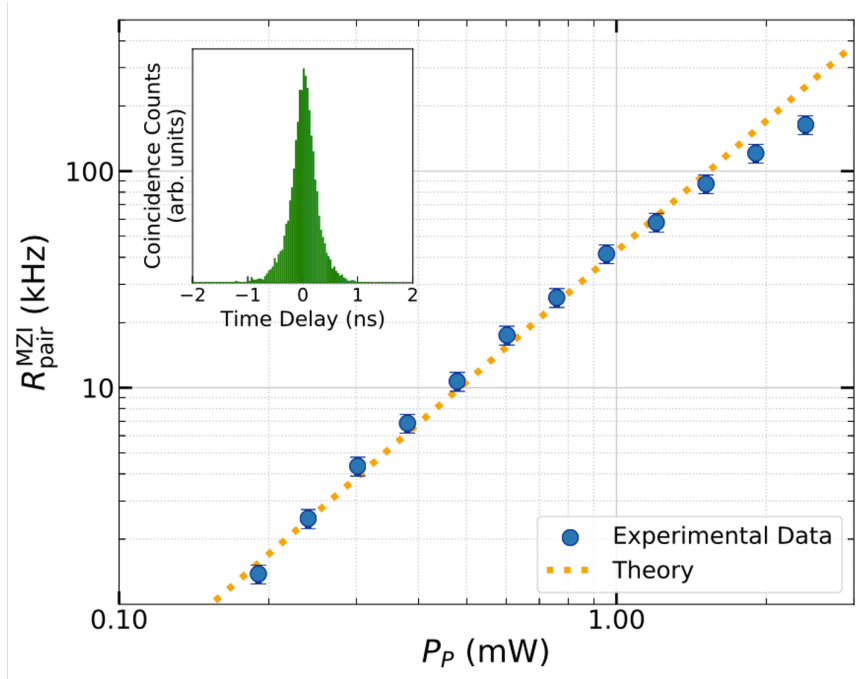
FIGURE 3.15. Power scaling of the SFWM coincidences. A time-tagging unit is used to correlate the arrival times of the idler and signal photons generated through SFWM. In this way, a histogram of the coincidences is obtained (as shown in the inset), and the rate of the events are obtained by integrating the peak over a sufficiently wide window (4 ns) and subtracting the histogram background (image taken from [70]).

In conclusion, SP- and DP-SFWM can be exploited in linearly uncoupled resonators, gaining control over the linear and nonlinear properties of the structure thanks to the presented strategy. Uncoupling through the DC results in a compact and easy-to-design structure but less robust against fabrication imperfection; on the other hand, the use of a MZI, although the more subtle design and larger footprint, enables a more efficient conversion, with a significantly larger isolation bandwidth. This approach is versatile, as it allows one to precisely control the isolation between the resonators and reconfigure the device to compensate for fabrication imperfections, for example by means of thermal heater.

## 3.3. Linear uncoupling with second-order nonlinearity

With standard ring resonators a careful dispersion engineering of the waveguide modes is usually required to balance chromatic material dispersion. While this approach is very effective for some material platforms and certain types of nonlinear interactions, it can be challenging for others, especially when one operates in a wide frequency range. Indeed, in this case solely dispersion engineering is not sufficient to guarantee the desired arrangement of the resonances. The strategy of the linearly uncoupled resonators immediately comes in handy, for it allows for efficient nonlinear

processes with limited dispersion engineering. This concept stands out as a powerful approach in all systems where material dispersion cannot be solely compensated by a proper design of the waveguide cross section.

Recent progresses in the fabrication of photonic integrated devices using material platforms characterized by a relatively large second-order nonlinearity, such as thin-film lithium niobate (TFLN) [13, 77] or (aluminum)gallium-arsenide-on-insulator [78], suggest the possibility of exploring the above-mentioned approach also in the framework of doubly resonant SPDC. Unlike SFWM, this process involves a very large frequency range, typically spanning from the fundamental frequency $\omega_{\mathrm{F}}$ to the second harmonic $\omega_{\mathrm{SH}} = 2\omega_{\mathrm{F}}$, with $\omega_{\mathrm{SH}}$ being the pump frequency. In ring resonators, dispersion engineering is critical to achieve doubly resonant condition, with the design tolerance being inversely proportional to the quality factors of the resonances involved in the nonlinear process. In addition, self- and cross-phase modulation, as well as the photorefractive effect [79], may limit the power range in which a device can operate. In principle these problems can be addressed through a fine tuning of the relative position of the resonances by means of thermal [80] or electro-optic elements [81]. However, the effectiveness of this strategy depends on the material platform and waveguide design, and it may come at the price of working at slightly different wavelengths than initially planned. In this scenario, we shall see that the use of linearly uncoupled resonators is quite useful, for it relaxes dispersion engineering efforts significantly, with doubly resonant condition achieved without relying only on dispersion engineering but rather exploiting the independent tuning of the two resonators.

**3.3.1. SPDC and DC structure.** The strategy of uncoupling two resonators thanks to a properly-designed DC can be exploited also with second-order nonlinear processes. Here, the main challenge is the very different spectral region of the pump and the generated photons, for the coupler will respond differently for the two different frequencies. We studied the situation of degenerate SPDC in a double-racetrack structure on a TFLN platform. In designing this system we considered a trapezoidal TFLN rib waveguide that can be fabricated by partial etching of a 300 nm thick X-cut LiNbO$_3$ (LN) film on a silica substrate. The waveguide features a sidewall angle $\theta = 61°$, which is the typical value for LN waveguides etched in Ar plasma and is cladded by a 750 nm thick electrically-cured hydrogen silsesquioxane (HSQ) cladding. As a case study, we choose the same material stack used in [82] to show the monolithic integration of electro-optically tunable circuits and superconducting nanowire single-photon detectors (SNSPDs) in TFLN waveguides. Hence, this structure represents a practical solution for the realization of fully integrated quantum photonic circuits where non-classical states of light can be simultaneously generated, manipulated, and detected.
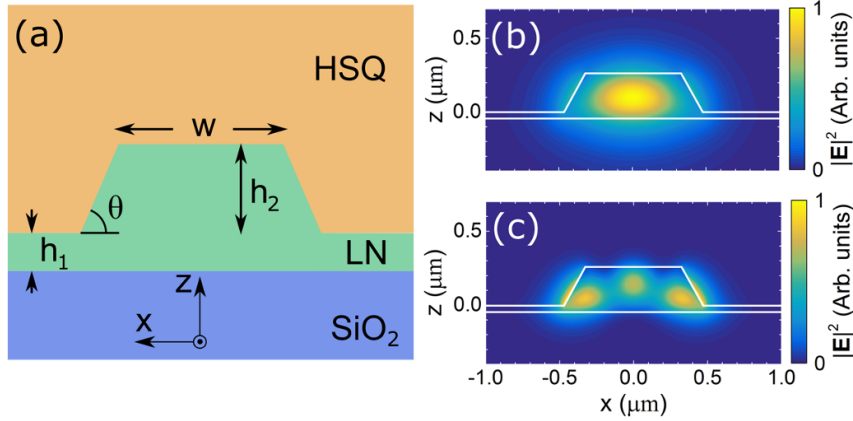
FIGURE 3.16. (a) Sketch of the TFLN waveguide cross section and the field profile of the phase-matched (b) TE0 mode at $\omega_F$ and (c) TE2 mode at $\omega_{SH}$ (images taken from [83]).

First we engineer the dispersion through the geometry of the waveguide. Its cross section is sketched in Fig. 3.16(a): it has a top width $w = 660\,\text{nm}$, an etching depth $h_2 = 255\,\text{nm}$, and a residual LN film of thickness $h_1 = 45\,\text{nm}$ at the base. When propagation is along the $y$ direction, the geometry of the waveguide is engineered to guarantee phase matching for the degenerate SPDC with a photon from the TE2 mode at the pump frequency $\omega_{SH} = 2\omega_F$ ($\lambda_{SH} = 775\,\text{nm}$) down-converted into two photons at the fundamental frequency $\omega_F$ ($\lambda_F = 1550\,\text{nm}$) in the TE0 mode. Yet, as we shall see in the following, exact phase matching is not required in this structure. The simulated [34] electric field intensity distributions for the TE0 and TE2 modes are shown in Figs. 3.16(b) and 3.16(c), respectively.

The whole structure, shown in Fig. 3.17, is composed of two racetrack resonators positioned side by side at a distance $d_{DC}$ along the straight section, forming the DC of length $L_{DC}$, shown in Fig. 3.18. The first racetrack has a straight arm of length $L_1 = 554.8\,\mu\text{m}$ and a bending radius $R_1 = 50\,\mu\text{m}$. In the upper straight section the waveguide width increases linearly from $w$ to $\overline{w} = 665\,\text{nm}$ and then decreases from $\overline{w}$ to $w$, forming a symmetric taper of total length $2L_T = 459.0\,\mu\text{m}$. This perturbation in the racetrack geometry is introduced so that phase matching is not satisfied in the taper region and Resonator 1 can support a resonant mode at $\omega_F$ without supporting any resonant modes at $\omega_{SH}$. The reason for this choice is that the DC can be designed to uncouple perfectly only at one of the two frequencies of interest, thus if at the fundamental harmonic the two resonators are linearly uncoupled, at the second harmonic there will be some residual linear coupling that can affect the down-conversion process; the study of the taper realization will be explained later. The second racetrack has a straight section of length $L_2 = 553.0\,\mu\text{m}$ and bending radius $R_2 = R_1$. These parameters are chosen to guarantee that Resonator 2 supports an odd-order resonant
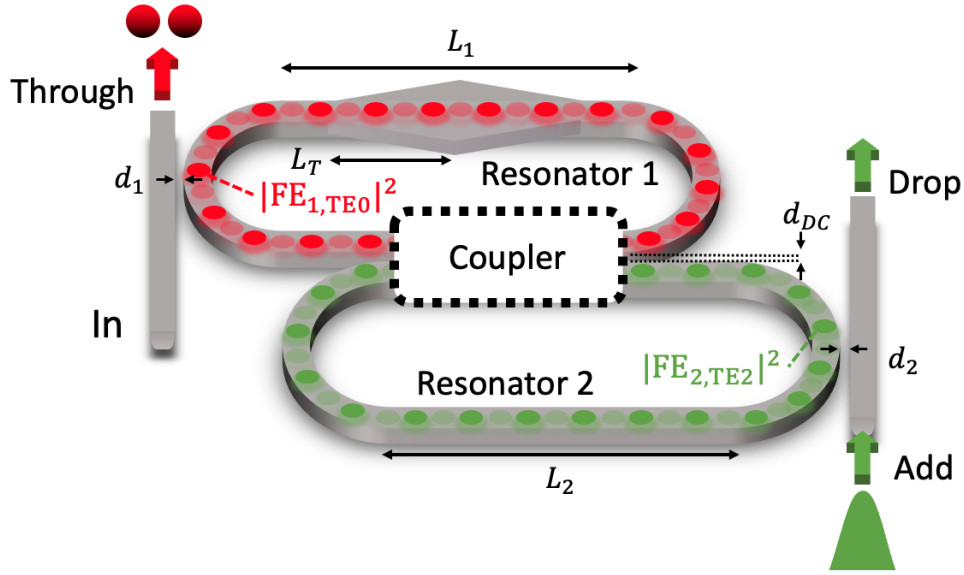
FIGURE 3.17. Sketch of the structure, with taper region in the upper arm of Resonator 1 and bus waveguides for pump injection and photon pairs extraction.  Red blobs indicate the mode TE0 propagating in Resonator 1 at $\omega_\mathrm{F}$, while green ones are for the TE2 mode in Resonator 2 at $\omega_\mathrm{SH}$.

mode at $\omega_{SH}$, thus no resonant mode at $\omega_F$.  Additionally, the two resonators are point-coupled with two bus waveguides positioned at distance $d_1$ and $d_2$, respectively, which correspond to the coupling constants $\sigma_1$ and $\sigma_2$.  These waveguides are used for the pump injection and the collection of the generated photons, as indicated in Fig. 3.17. Efficient light coupling with the chip at both $\omega_F$ and $\omega_{SH}$ can be obtained by means of grating couplers featuring a negative diffraction angle and a self-focusing effect of the diffracted beam [84].

Knowing the behavior of the DC at the two different frequencies is fundamental to study the pair generation process.  The strength of the nonlinear interaction depends
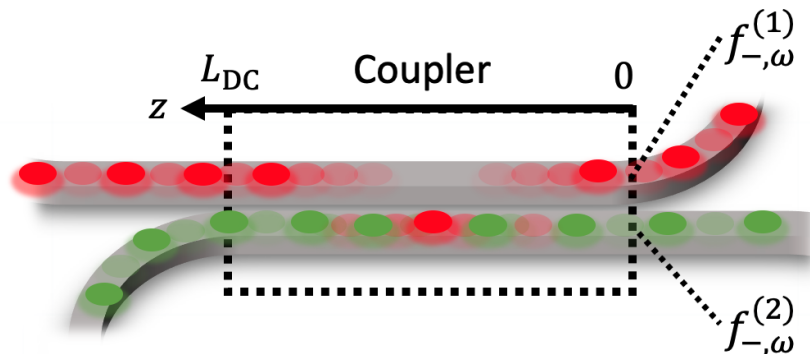


FIGURE 3.18. Sketch of the fields propagating in the directional coupler.  As can be seen, only the field at the fundamental frequency oscillates in the lower channel where the two fields overlap.

on the field distribution inside the DC, which is determined by $L_{DC}$ and $d_{DC}$. In Fig. 3.19 we plot the DC coupling length $L_c = \pi/\kappa_c$, with $\kappa_c$ the coupling coefficient, as a function of $d_{DC}$ for the TE0 mode at the fundamental frequency and for the TE2 mode at the second harmonic. In general, the coupling lengths at $\omega_F$ and $\omega_{SH}$ are different, due to the different field distribution of the two modes. In particular, $L_c$ grows faster for the second-harmonic mode, because of the stronger light confinement in the waveguide at $\omega_{SH}$. We choose to work with $d_{DC} = 1225\,\text{nm}$, for which the coupling length at $\omega_{SH}$ is more than three times that at $\omega_F$ (see Fig. 3.19). Thus, by taking $L_{DC} = L_c = 552\,\mu\text{m}$, one ensures perfect linear uncoupling at $\omega_F$. This choice is a trade-off between having small resonators with a high finesse and working with a sufficiently long DC in which SPDC can take place. With this length of the coupler, at the SH there is a small coupling between the two resonators. As we sketched in Fig. 3.18, the field at $\omega_F$ circulating in Resonator 1 oscillates between the two channels of the DC, while that at $\omega_{SH}$ circulating in Resonator 2, due to the very small coupling coefficient, does not propagate in the upper channel of the coupler. We immediately see a difference with respect to the case of SFWM with the DC structure: the fields overlap only in one channel of the coupler. With this system, we are dealing with a very large frequency range, thus the linear uncoupling of the two resonators at



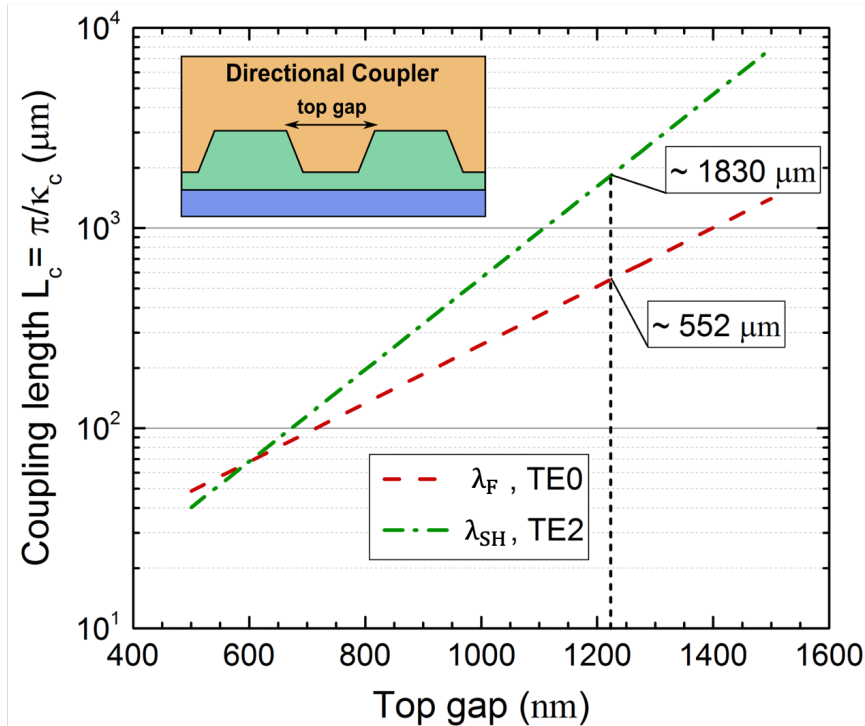FIGURE 3.19. Coupling length for a round-trip power transfer between two identical waveguides at $\omega_{\text{F}}$ (dashed red) and $\omega_{\text{SH}}$ (dot-dashed green). The working point is also indicated. Inset: cross section of the DC (image taken from [83]).

both frequencies is challenging to obtain. In particular, for our parameter choice, the DC cross-transmission coefficient is small but not zero at $\omega_{SH}$, therefor we need to limit the coupling of the two resonators in some way. The strategy is to remove the resonance at $\omega_{SH}$ in Resonators 1 via the aforementioned adiabatic taper. The increasing width of the waveguide produces an uneven shift of the comb of Resonator 1, for different frequencies acquire a different phase while propagating the taper. This prevents resonant splitting due to strong linear coupling of the two resonators at the pump frequency.

The success of the uncoupling can be viewed from the linear spectra of the structure. In Fig. 3.20(a) and (b) we show the resulting field intensity enhancement in
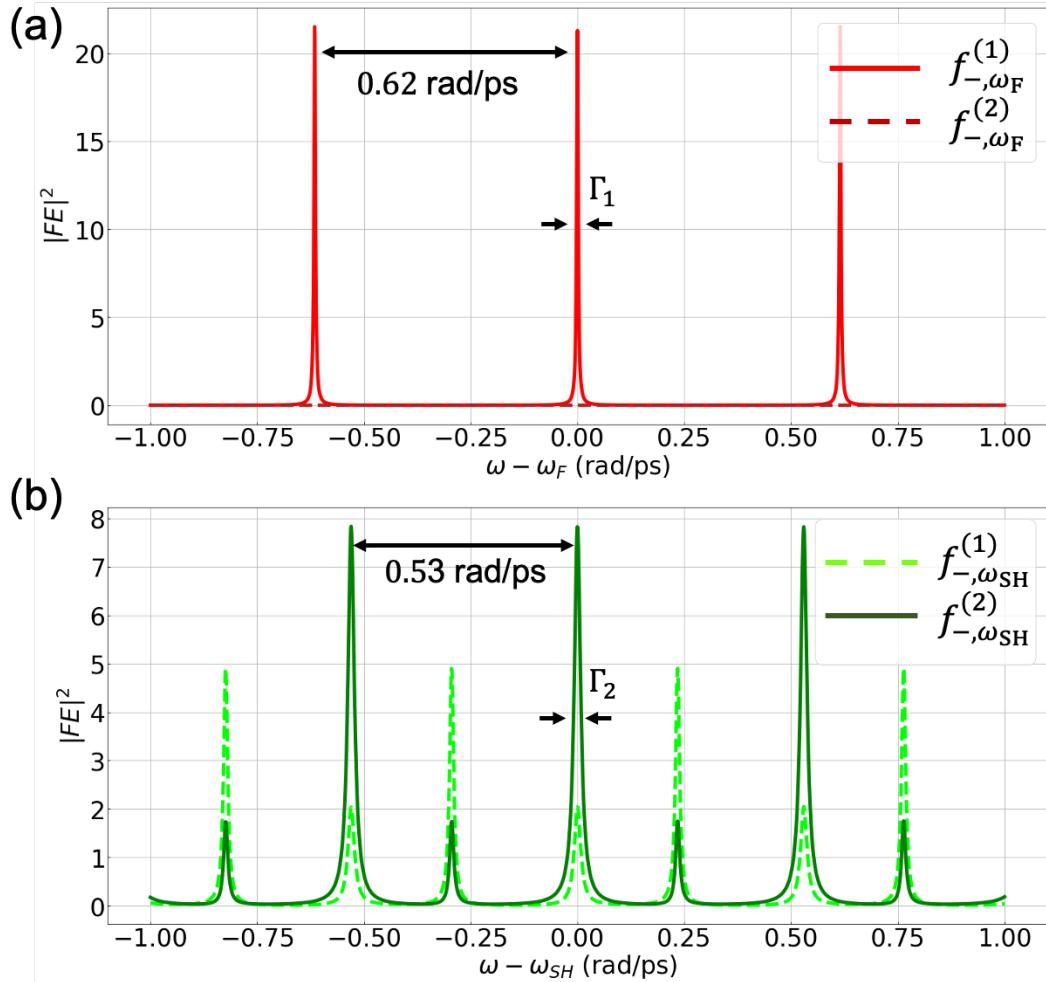


FIGURE 3.20. Intensity enhancement of the fields in the two separate racetracks (a) at the fundamental frequency and (b) at the second harmonic frequency. Notice the perfect isolation of the resonators at $\omega_F$ and the effect of the small pump leak in Resonator 1 at $\omega_{SH}$.

the two resonators as a function of the frequency detuning from $\omega_F$ and $\omega_{SH}$, respectively. In our structure, at $\omega_F$ light is circulating only in Resonator 1, while at $\omega_{SH}$ one finds light in both resonators. However, the two combs of resonances that can be identified in Fig. 3.20(b) are independent and correspond to the resonant frequency of Resonator 1 and Resonator 2, respectively. Finally, we set the coupling coefficient $\sigma_1 = 0.995$ and $\sigma_2 = 0.93$. These parameters control the coupling of the two resonators with the corresponding bus waveguides. Unlike in a single point-coupled ring, in our structure the coupling condition can be adjusted for the two combs of resonances independently, thus one has a large flexibility in controlling the field enhancement and the quality factors at $\omega_F$ and $\omega_{SH}$. In determining these values we assumed reasonable propagation losses $\alpha_F = 1\,\mathrm{dB/cm}$ [77] and $\alpha_{SH} = 3\,\mathrm{dB/cm}$. These values result in a full width half maximum of $\Gamma_1 = 4\,\mathrm{rad/ns}$ and $\Gamma_2 = 18\,\mathrm{rad/ns}$, corresponding to $Q_1 \approx 290000$ and $Q_2 \approx 135000$, respectively.

**3.3.2. SPDC and MZI structure.** Like we did for SFWM, we can exploit the advantage of using the MZI also for SPDC. We can combine the tapering strategy for removing the unwanted resonance with the higher generation efficiency of the MZI structure. Again, the interferometer can be realized by means of two DCs that split the fundamental frequency in both arms. The SH field would then be either confined in only one arm of the interferometer or circulating in both of them with different intensities, depending on the chosen length of the DCs. In any case, SPDC can take place since both fields are present in the same region. Considering the same waveguide geometry described for the previous case, here we show a simulation of the MZI structure where the two identical DCs are designed to split the field at the fundamental harmonic in both arms of the interferometer. This is obtained by setting the DC to have coupling coefficient $\kappa_F = 0.0097\,\mu\mathrm{m}^{-1}$, thus a coupling coefficient $\kappa_{SH} = 0.004\,\mu\mathrm{m}^{-1}$, and length $L_{DC} = 80.9\,\mu\mathrm{m}$. This corresponds to having, over the
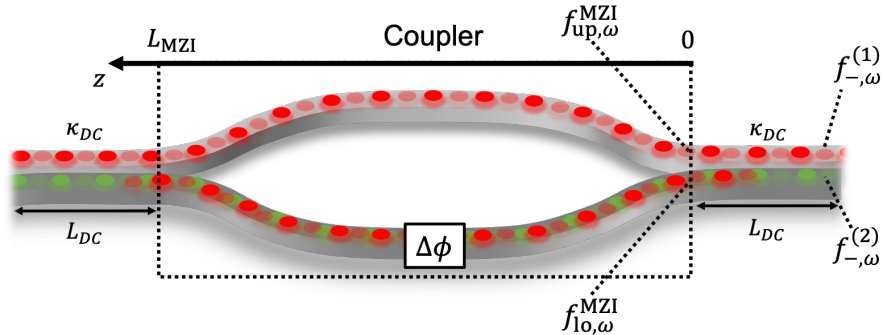


FIGURE 3.21. Sketch of the MZI coupler realized with two DCs. At $\omega_{SH}$ light is confined in the lower arm of the interferometer, while at $\omega_F$ the DCs are designed to (50):(50) split the field in both arms.

length $L_{DC}$, a (50):(50) split at the fundamental frequency and $\approx$ (90):(10) split at the SH.

The structure we simulated is similar to that sketched in Fig. 3.17, where the coupler is the MZI sketched in Fig. 3.21. The two resonators have the same straight length $L_1 = L_2 = 561.9\,\mu$m but different radii $R_1 = 70.0\,\mu$m and $R_2 = 71.1\,\mu$m, while the MZI has a length $L_{MZI} = 400\,\mu$m. In the upper straight section of Resonator 1 is built the same symmetric taper previously discussed. When treating SPDC process with the MZI, we have to care about the different frequencies involved. In fact, the phase of the interferometer should be set to realize destructive interference between the fields at $\omega_F$, therefor, since we have $\omega_{SH} = 2\omega_F$, the SH will always experience constructive interference. This highlights the importance of the small coupling that
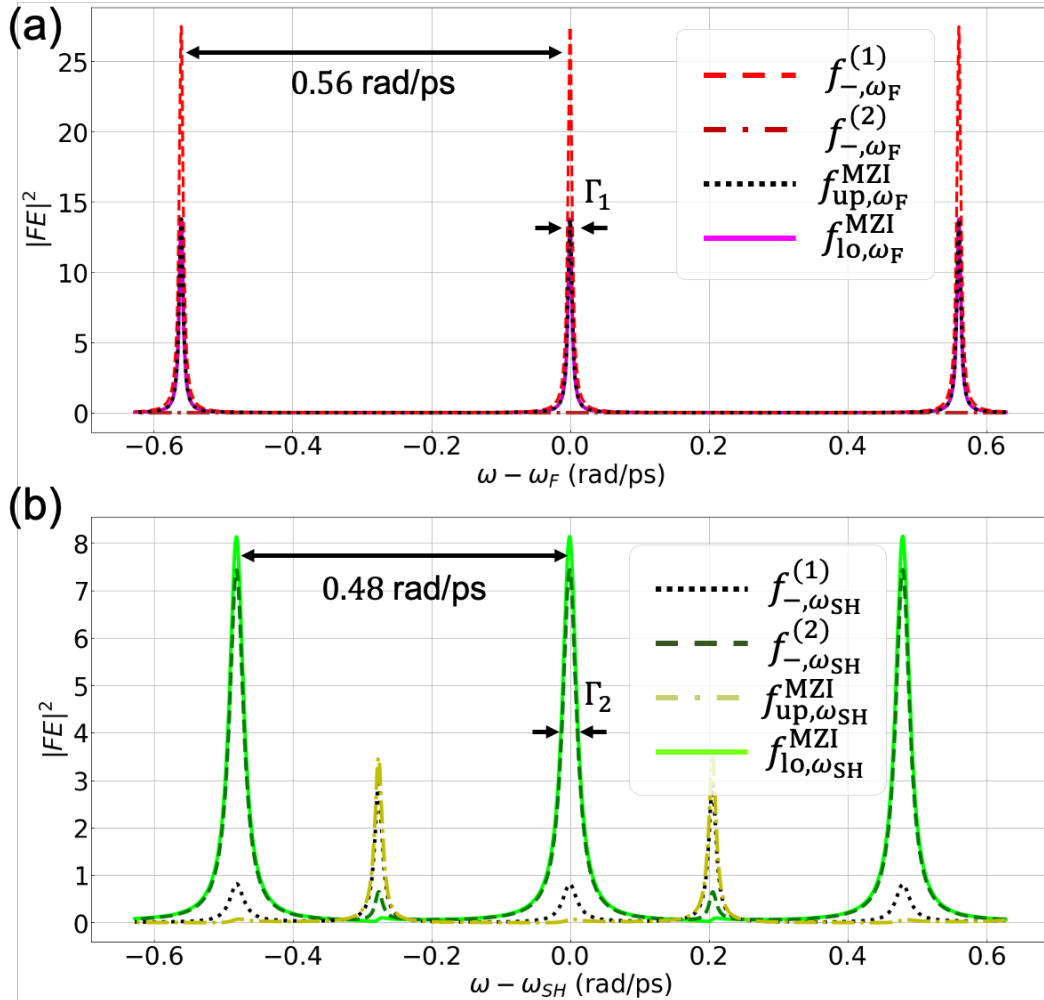


FIGURE 3.22. Intensity enhancement of the fields in the two separate racetracks and inside the arms of the MZI (a) at the fundamental frequency and (b) at the second harmonic frequency.

the DC have at $\omega_{\text{SH}}$ and the taper to remove the corresponding resonance in Resonator 1. The correct behavior of the MZI can be investigated by plotting the intensity enhancement outside and inside of it, as we do in Fig. 3.22. We can see in Fig. 3.22(a) that the field at $\omega_{\text{F}}$ is circulating only in Resonator 1 (red dashed line) and not in Resonator 2 (brown dashed-dot line), as we expect from the correct behavior of the MZI. Instead, inside the interferometer, we see that the field is half of the intensity in both arms (black dotted and magenta solid lines). Similarly, in Fig. 3.22(b) we see that the field at $\omega_{\text{SH}}$ is circulating only in Resonator 2 (green dashed line) and not in Resonator 1 (black dotted line), but inside the MZI the field circulates only in the lower arm (lime solid line). Due to the leakage effect, we can see some small resonances appearing, as well as a slightly higher value of the field inside the arm of the MZI with respect to that outside. Both these effects are though negligible and do not affect the functionality of the structure. Here, we set the coupling coefficients $\sigma_1 = 0.99$ and $\sigma_2 = 0.94$, that result in a full width half maximum of $\Gamma_1 = 5\,\text{rad/ns}$ and $\Gamma_2 = 17\,\text{rad/ns}$, corresponding to $Q_1 \approx 245000$ and $Q_2 \approx 145000$, respectively.

## 3.4. Generation rate and spectral properties

As an example, we demonstrate that one can take advantage of the peculiar features of the double-racetrack resonators system to generate nearly uncorrelated photon pairs by SPDC. If we consider the DC case, the expression for the biphoton wavefunction describing the generated photon pairs can be calculated from equation (1.45) by considering the asymptotic fields in the coupler (3.2). The result is

$$
\phi_{\text{SPDC}}(\omega_1, \omega_2) = i\frac{\alpha}{\beta}\overline{\chi}^{(2)}\sqrt{\frac{\hbar\omega_S\omega_I\omega_P}{8\pi\varepsilon_0\varepsilon_r^3\mathcal{A}_{\text{eff}}^{\text{SPDC}}\,v_{g,S}(\omega_1)v_{g,I}(\omega_2)v_{g,P}(\omega_1+\omega_2)}}
$$
$$
\times\,\phi_P(\omega_1+\omega_2)\mathcal{J}_{ch}\left(\omega_1, \omega_2, \omega_1+\omega_2\right)\ ,
\tag{3.42}
$$

where $\overline{\chi}_2$ is the typical value of the second-order nonlinearity of LN, $\mathcal{A}_{\text{eff}}^{\text{SPDC}}$ is the nonlinear effective area for SPDC [16], and $\phi_{\text{P}}(\omega_1+\omega_2)$ is the pump spectral profile. Finally, $\mathcal{J}_{ch}(\omega_1+\omega_2, \omega_1, \omega_2)$ is the field spatial integral in the lower channel of the DC describing the second-order nonlinear interaction. Its expression, adapting (3.18) to the SPDC case, is

$$
\mathcal{J}_{ch}\left(\omega_1, \omega_2, \omega_1+\omega_2\right) = \int_0^{L_{\text{DC}}} f_{ch,\omega_1}^*(z)f_{ch,\omega_2}^*(z)f_{ch,\omega_1+\omega_2}(z)e^{i\Delta kz}\ ,
\tag{3.43}
$$

with $f_{ch,\omega}(z)$ given by (3.3) and $\Delta k = k_P(\omega_1+\omega_2) - k_S(\omega_1) - k_I(\omega_2)$. Here, we are analyzing degenerate SPDC, thus we take $\omega_S = \omega_I = \omega_{\text{F}}$ and $\omega_P = \omega_{\text{SH}}$, and call TE0 the modes $S$ and $I$, and TE2 the mode $P$. Then, we consider a more general

expression for (3.42)

$$\phi_{\mathrm{SPDC}}(\omega_1, \omega_2) = i\frac{\alpha}{\beta}\overline{\chi}^{(2)}\sqrt{\frac{\hbar\omega_{\mathrm{F}}^2\omega_{\mathrm{SH}}}{8\pi\varepsilon_0 n_{\mathrm{F}}^4 n_{\mathrm{SH}}^2 \mathcal{A}_{\mathrm{eff}}^{\mathrm{SPDC}}\, v_{g,\mathrm{F}}(\omega_1)v_{g,\mathrm{F}}(\omega_2)v_{g,\mathrm{SH}}(\omega_1+\omega_2)}}$$

$$\times\, \phi_P(\omega_1+\omega_2)\mathcal{J}_{ch}\left(\omega_1, \omega_2, \omega_1+\omega_2\right)\ , \tag{3.44}$$

where we took the dielectric function $\varepsilon_r$ to be frequency dependent and thus writing $\varepsilon_r(\omega_{\mathrm{F}}) = n_{\mathrm{F}}^2$ and $\varepsilon_r(\omega_{\mathrm{SH}}) = n_{\mathrm{SH}}^2$, where clearly $n_F$ and $n_{SH}$ are the mode effective indices of the waveguide at $\omega_F$ and $\omega_{SH}$, respectively. When the linear uncoupling is reached, pump field belongs only to Resonator 1 while signal and idler only to Resonator 2, thus we can use equation (3.3) to rewrite (3.43) as

$$\mathcal{J}_{ch}\left(\omega_1, \omega_2, \omega_1+\omega_2\right) = -\,\mathrm{FE}_{1,\mathrm{TE0}}(\omega_1)\mathrm{FE}_{1,\mathrm{TE0}}(\omega_2)\mathrm{FE}_{2,\mathrm{TE2}}(\omega_1+\omega_2)$$

$$\times\left[i\int_0^{L_{\mathrm{DC}}}\cos^2\left(\kappa_{\mathrm{F}}z\right)\sin(\kappa_{\mathrm{SH}}z)e^{i\Delta kz}dz\right.$$

$$\left.+\int_0^{L_{\mathrm{DC}}}\sin^2(\kappa_{\mathrm{F}}z)\cos\left(\kappa_{\mathrm{SH}}z\right)e^{i\Delta kz}dz\right]\ . \tag{3.45}$$

Here, $\mathrm{FE}_{1(2),\mathrm{TE0}(\mathrm{TE2})}(\omega)$ is the field enhancement in Resonator 1(2) of the TE0(TE2) mode, whose modulus square is described by (1.71), the phase mismatch became $\Delta k = k_{\mathrm{TE2}}(\omega_1+\omega_2) - k_{\mathrm{TE0}}(\omega_1) - k_{\mathrm{TE0}}(\omega_2)$, with $k_{\mathrm{TE0}(\mathrm{TE2})}(\omega)$ the wavevector of the TE0(TE2) mode of the waveguide, and $\kappa_{\mathrm{F}}$ and $\kappa_{\mathrm{SH}}$ are the coupling coefficients of the DC at the fundamental and second harmonic frequency, respectively. A similar comparison that we did for SFWM between the overlap integral of a ring resonator $\mathcal{J}_{\mathrm{ring}}(\omega_1+\omega_2, \omega_1, \omega_2)$ and that in equation (3.45) can be made here. If we assume our structure parameters, $L_1 \simeq L_2 \simeq L_{\mathrm{ring}}$, the same quality factors for both systems, and $\Delta k = 0$, we obtain

$$\mathcal{J}_{ch}(\omega_1+\omega_2, \omega_1, \omega_2) \simeq \mathcal{J}_{\mathrm{ring}}(\omega_1+\omega_2, \omega_1, \omega_2)\frac{L_{DC}}{2L_{\mathrm{ring}}}\ , \tag{3.46}$$

thus giving an estimate of the decrease in the pair generation rate with respect to the standard ring. Differently from the SFWM case, there is not a theoretical optimal length for the DC, thus the limit is set by the coherence length of the process. In fact, we can further analyze the linear uncoupling strategy by studying the spatial overlap integral $\mathcal{J}_{ch}\left(\omega_1+\omega_2, \omega_1, \omega_2\right)$ of (3.45). We plot in Fig. 3.23 its modulus square as a function of $\Delta k$. We find a relatively wide region (some $0.01\,\mu\mathrm{m}^{-1}$), highlighted with a green band, around the phase matching condition $\Delta k = 0$ in which the strength of the nonlinear interaction has the same order of magnitude. This indicates that SPDC is particularly efficient as long as its coherence length $(L_{\mathrm{coh}} = \pi/\Delta k)$ is longer than $L_{\mathrm{DC}}$. This result is analogous to that observed for third-order nonlinear interactions in linearly uncoupled resonators, in which the required coherence length is set by the DC length and is independent of the quality factors
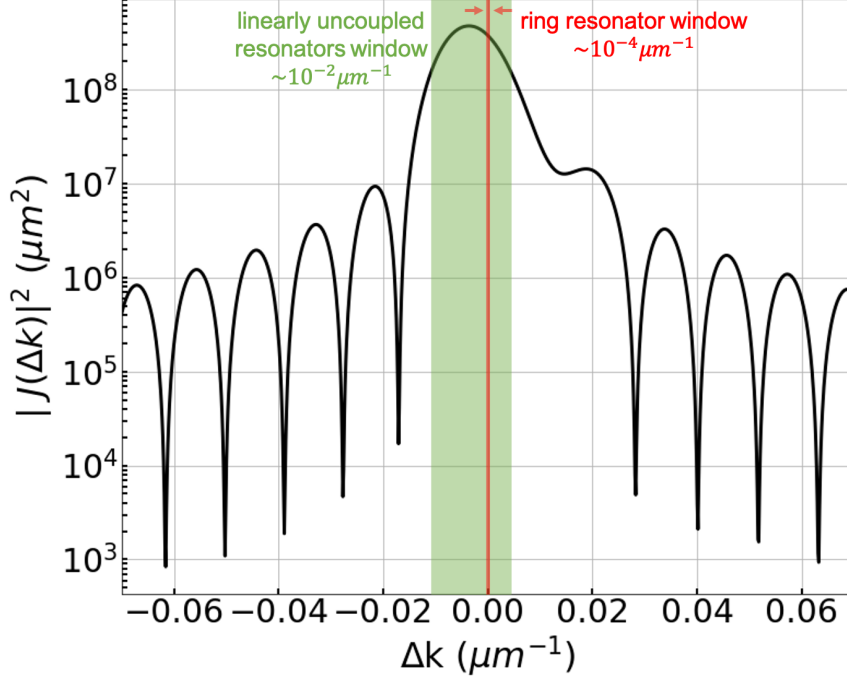
FIGURE 3.23. Spatial overlap integral (3.45) modulus square as a function of $\Delta k = k(\omega_{\mathrm{SH}}) - k(\omega_1) - k(\omega_{\mathrm{SH}} - \omega_1)$, with $\omega_{\mathrm{SH}} = \omega_1 + \omega_2$. The green band indicates the window in which the efficiency has almost the same order of magnitude; it can be compared to that of a single ring resonator (red band), that is two orders of magnitude smaller.

of the resonators [67]. On the contrary, in a single ring resonator, the coherence length is related to the distance travelled by light in a dwelling time $\tau_d = v_g Q / \omega$. For comparison, by assuming a ring resonator with our waveguide parameters, this would require a coherence length larger than $30\,000\,\mu$m, which corresponds to an operational bandwidth of only $\Delta k = 2 \times 10^{-4}\,\mu$m$^{-1}$, represented by the red band in Fig. 3.23. As a consequence, our system is more flexible and robust against fabrication imperfections that may affect the waveguide dispersion.

Now we turn to the generation of uncorrelated photon pairs, and we consider a Gaussian pump pulse centered at $\omega_{\mathrm{SH}}$, having duration $\tau = 28\,$ps and peak power $P_P = 15\,$mW, which corresponds to an average number $|\alpha|^2 = 1.6 \times 10^9$ of pump photons. The pulse is injected in Resonator 2 through the bus waveguide, and the photons are generated in the arms of the coupler and then collected via the waveguide coupled to Resonator 1. We compare the result we obtain for both DC and MZI structures. The choice of the coupling parameters $\sigma_1$ and $\sigma_2$ is linked to the goal of generating a separable photon pair. In fact, these parameters are chosen to ensure the quality factor of Resonator 1 to be larger than that of Resonator 2 ($Q_1 > Q_2$), providing a feasible strategy for the generation of nearly uncorrelated photon pairs [85]. The idea is to be as close as possible to the critical coupling condition for the
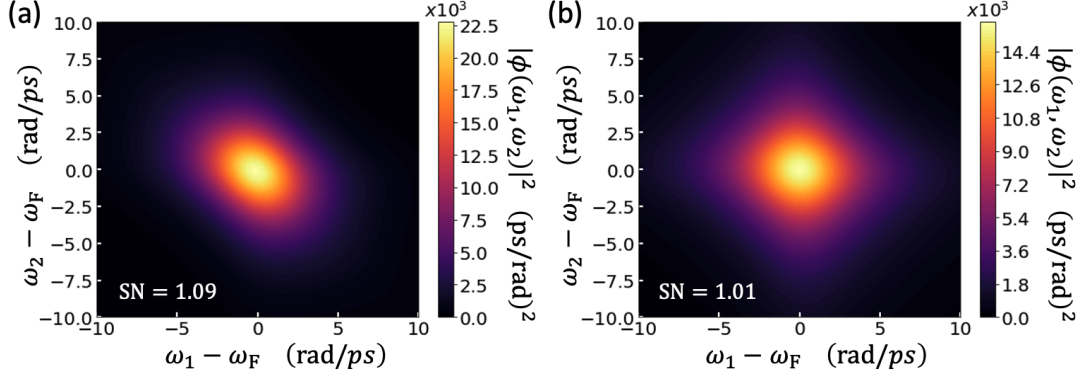
FIGURE 3.24. (a) JSD for a single ring resonator. The value of the SN is theoretically bounded to a minimum of 1.09. (b) Symmetric JSD for the linearly uncoupled resonators (same results for both DC and MZI). The SN is 1.01, below the single ring limit.

pump field at $\omega_{SH}$ and to overcouple the Resonator 1 at $\omega_F$; in this way one can increase the pump field enhancement and the outcoupling of the generated pairs. Thanks to the linear uncoupling strategy we gain the necessary independent control of the quality factors of the two combs of resonances.

From the biphoton wavefunction (3.44), we calculate the state Schmidt number SN [86] and the $|\beta|^2$ for the DC structure. The results are a SN = 1.01, below the single ring limit of 1.09, which confirms that the photons are nearly-uncorrelated, and a $|\beta|^2 \approx 0.01$. By assuming a pump repetition rate of 1 MHz, this correspond to a generation rate of $10^4$ pairs per second, which is comparable with that achieved with other integrated platforms [87]. Then, we calculate the $|\beta|^2$ for the MZI structure, using the mentioned parameters $\sigma_1$ and $\sigma_2$, chosen to obtain the same SN = 1.01. This decision is made to compare the efficiency of the structures when generating the same state. From our calculation we obtain a similar value $|\beta|^2 \approx 0.01$. We deduce that in the MZI structure, due to the bigger length of the resonators with respect to the DC case, the high losses at the SH lower the efficiency of the process. Thus, even if in theory this system should be more efficient, the result is the same as the DC case. Nonetheless, with the Mach-Zehnder interferometer we gain the advantage of the flexibility against fabrication defects discussed earlier. In Fig. 3.24 we plot the joint spectral density (JSD) $|\phi(\omega_1, \omega_2)|^2$, in the case of the standard ring resonator (panel (a)) and in both cases of DC and MZI structures (panel (b)). The latter JSD is symmetric, suggesting that the biphoton state is separable. This result shows how with the linear uncoupling strategy one can easily reach a value of the SN arbitrarily close to 1, for the quality factors of pump and generating resonators are intrinsically independent. The choice between uncoupling through DC or MZI is still linked to the advances in the technology, for the MZI structure, although more robust and efficient,

can suffer from high losses while the DC structure is less affected by this problem thanks to its smaller footprint.

## 3.5. Beyond two-photon states

We showed how the linear uncoupling strategy can provide a precise control on the linear properties of a structure which can be directed towards the generation and manipulation of photon pairs. One may ask if this strategy is applicable to go beyond two-photon states. Indeed, we investigate the possibility to reach optical parametric oscillations (OPO) in such structures, within the visible-IR light frequency spectrum.

### 3.5.1. Optical parametric oscillation study.
In a resonator, we call OPO the regime where the generated field is large enough to initiate the stimulate generation process. The threshold to this regime can be considered the moment when the pair generation rate equals the linewidth of the resonances

$$R_{\text{th}}^{\text{OPO}} = \Gamma_S = \Gamma_I \ . \tag{3.47}$$

With this hypothesis, we can estimate the pump power threshold for the OPO. Here, we discuss the case of SFWM, by considering the pair generation rate for a ring resonator (3.28) in order to calculate the pump threshold

$$P_{P,\text{th}}^{\text{ring}} = \frac{\omega_P^2 L Q_{C,P}}{8 \gamma_{\text{NL}} v_g^2 Q_P^2} \sqrt{\frac{\omega_S Q_I + \omega_I Q_S}{\omega_S \omega_I Q_S Q_I} R_{\text{th}}^{\text{OPO}}} \ . \tag{3.48}$$

It was demonstrated that in $Si_3N_4$ ring resonators one can achieve OPO with few milliwatts of pump power [88]. If we assume the structure parameters from [88], such as $R = 23 \, \mu\text{m}$, $Q \approx 10^6$, $\omega_S = 1431 \, \text{rad/ps}$, $\omega_P = 2033 \, \text{rad/ps}$, $\omega_I = 2602 \, \text{rad/ps}$ and $\Gamma_S = \Gamma_I = 1.88 \, \text{rad/ns}$, and typical $Si_3N_4$ platform values for the group index $n_g = 2.086$ and the nonlinear coefficient

$$\gamma_{\text{NL}} = \frac{\omega_P n_2}{c} \frac{1}{\mathcal{A}_{\text{eff}}^{\text{SFWM}}} \ , \tag{3.49}$$

with nonlinear refractive index $n_2 = 2.6 \times 10^{-7} \, \mu\text{m}^2/\text{W}$ [20, 89] and SFWM nonlinear effective area $\mathcal{A}_{\text{eff}}^{\text{SFWM}} = 0.645 \, \mu\text{m}^2$, by setting the condition (3.47) we get $P_{P,\text{th}}^{\text{ring}} = 3.4 \, \text{mW}$. We can then compare these results with the OPO power threshold in the case of linearly uncoupled resonators. We considered the case of uncoupling through MZI, assuming $R = 23 \, \mu\text{m}$, $L_1 = L_2 = 2L = 289 \, \mu\text{m}$, $L_{\text{MZI}} = \pi R = 72.26 \, \mu\text{m}$, and the same platform parameters as before, resulting in a threshold power $P_{P,\text{th}}^{\text{MZI}} = 54.5 \, \text{mW} = 16 P_{P,\text{th}}^{\text{ring}}$. In this calculation we assumed $L_{\text{MZI}} \ll L_{\text{coh}}$ and the DCs of the interferometer to work as (50):(50) beam splitters for all the three frequencies. This is an optimistic result, for the wide range of pump, signal, and idler hardly allows the DCs to work in this ideal situation. As we shall see, the feasible solution is to

split only the pump and the signal, while keeping the idler in only one arm of the interferometer.

**3.5.2. Power effect: self-phase and cross-phase modulation.** We want to study the behavior of integrated structures when we cannot consider a low pump power regime. In fact, we are approaching the OPO threshold by increasing the power $P_P$ injected in the system, thus requiring to account for the nonlinear Kerr effect; in particular self-phase modulation (SPM) and cross-phase modulation (XPM) (Fig. 1.9). We can estimate the strength of such effects by studying the nonlinear coefficients

$$\gamma^{\text{SPM}} = \frac{\omega_P n_2}{c \mathcal{A}^{\text{PPPP}}_{\text{eff}}} \text{ and } \gamma^{\text{XPM}}_J = \frac{\omega_J n_2}{c} \frac{1}{\mathcal{A}^{\text{PJPJ}}_{\text{eff,J}}} \ , \tag{3.50}$$

with $J = S, I$, which depend on the usual nonlinear effective areas [72]

$$\mathcal{A}^{\text{PPPP}}_{\text{eff}} = \frac{\left( \int |E_P(x,y)|^2 dxdy \right)^2}{\int |E_P(x,y)|^4 dxdy} \tag{3.51}$$

and

$$\mathcal{A}^{\text{PJPJ}}_{\text{eff,J}} = \frac{\left( \int |E_P(x,y)|^2 dxdy \right) \left( \int |E_J(x,y)|^2 dxdy \right)}{\int |E_P(x,y)|^2 |E_J(x,y)|^2 dxdy} \tag{3.52}$$

for SPM and XPM, respectively. In (3.51) and (3.52) we are considering an electric field $E(x,y)$ with only one component, and we are assuming only one relevant element of the $\chi^{(3)}$ tensor and, for each mode, a homogeneous phase and group indexes.

In a standard ring resonator, the effect of SPM is half that of XPM; in fact, usually one works in the anomalous dispersion regime (Fig. 1.8(b)), thus, when the power increases and the combination of SPM and XPM forward-shifts the pump resonance, this effect compensates the dispersion mismatch. For this reason, the ring resonator
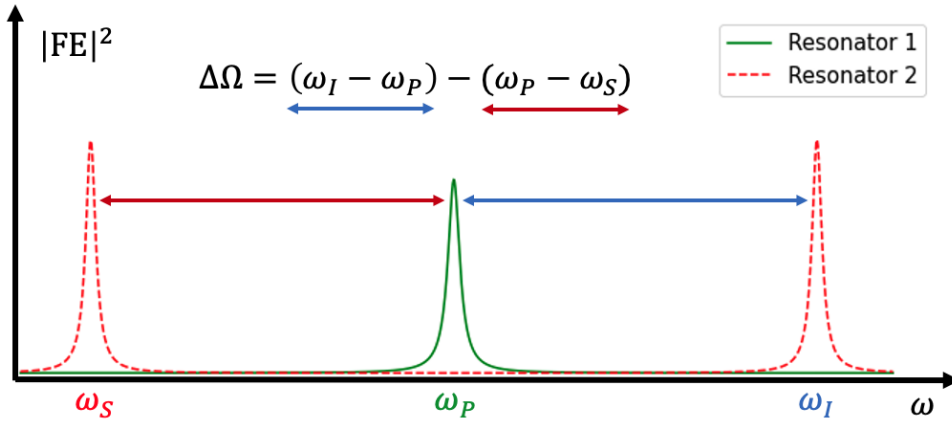


FIGURE 3.25. Pump, signal, and idler relative position in the case of linearly uncoupled resonators (figure of merit).

should be designed to cancel this phase mismatch at a sufficiently large injected power to initiate OPO. Here, we show how the MZI structure can be exploited to explore different configurations, for example allowing to work in a normal dispersion regime (Fig. 1.8(a)), by increasing the effect of SPM with respect to that of XPM, or in a configuration where the Kerr effect compensates the normal dispersion independently of the injected power, allowing for a reconfigurable OPO source. The idea is that, if we imagine to pump the system from Resonator 1, SPM acts all along that resonator, causing a refractive index change

$$\Delta n_{\mathrm{SPM}} \propto \frac{P_P n_2}{\mathcal{A}_{\mathrm{eff}}^{\mathrm{PPPP}}} \ , \tag{3.53}$$

while SPM and XPM are both present only in the coupler region, where all the fields overlap. We assume (50):(50) splitting ratio of the fields, getting

$$\Delta n_{\mathrm{SPM}}^{\mathrm{MZI}} = \frac{\Delta n_{\mathrm{SPM}}}{2} \ \text{and} \ \Delta n_{\mathrm{XPM}}^{\mathrm{MZI}} \simeq \Delta n_{\mathrm{SPM}} \ , \tag{3.54}$$

where we considered a similar contribution from the different effective areas. The overall effect is a larger phase shift induced by the SPM with respect to that of XPM. To analyze this effect, we define the figure of merit (FOM) shown in Fig. 3.25

$$\Delta \Omega = (\omega_I - \omega_P) - (\omega_P - \omega_S) \ , \tag{3.55}$$

which represents pump, signal, and idler resonances relative position. In Fig. 3.26 we compare this FOM as a function of the injected power $P_P$ for both the ring resonator and the MZI structure. As we can see, for increasing power, $\Delta \Omega$ assumes increasing
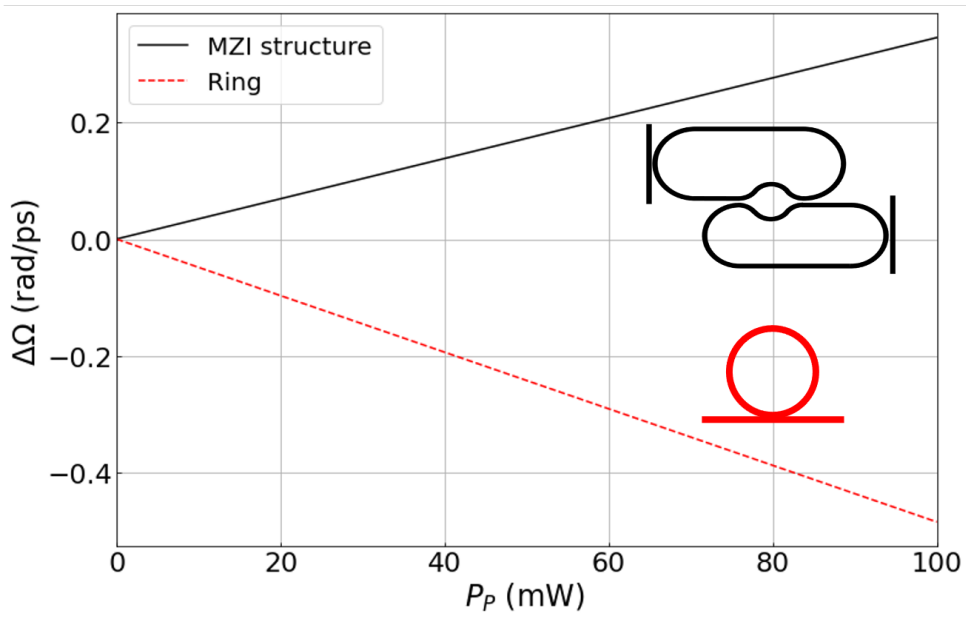


FIGURE 3.26. Comparison between the FOM of the ring resonator with that of the MZI structure.
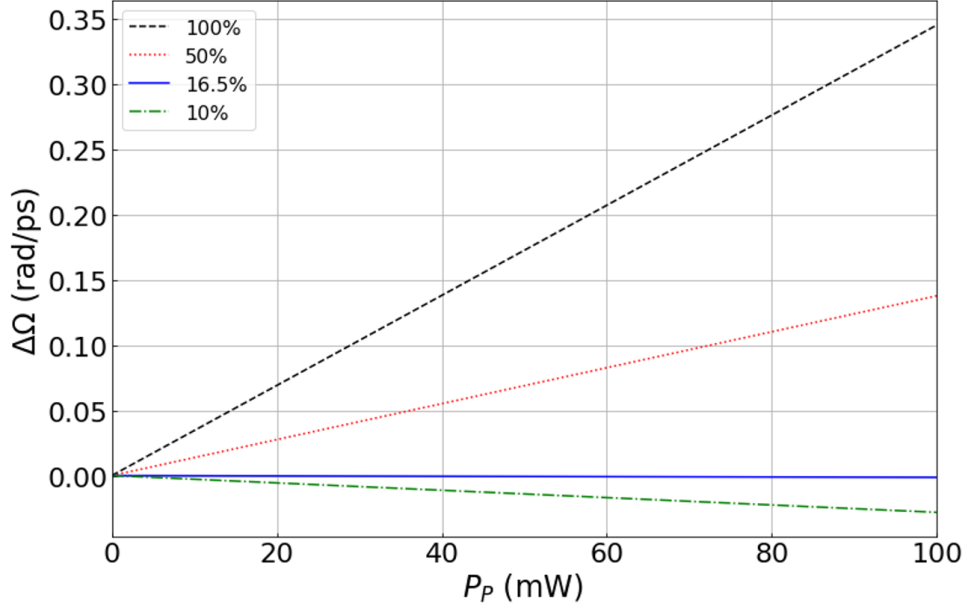
FIGURE 3.27. FOM for the MZI structure as a function of the injected power for different strength of the SPM.

positive values in the MZI case, while decreasing negative values in the ring case. This explains why one usually works in the anomalous dispersion regime with the ring and how with the MZI structure we can explore the normal dispersion regime. Moreover, with the flexibility of the MZI structure, we can investigate different configurations, where the strength of the SPM is tuned by playing with the width of Resonator 1's waveguide, modifying the mode confinement and consequently the SPM nonlinear factor (3.50). We show a simulation in Fig. 3.27, where we can actually work in both anomalous and normal dispersion regimes, deepening on the strength of SPM. For a specific value (blue solid line), it is also possible to design a power-independent OPO source, where the effect of SPM and XPM are compensated for any value of $P_P$.

**3.5.3. OPO in linearly uncoupled resonators design.** In order to actually design a working device, we have to consider the different behavior of both the Mach-Zehnder interferometer and the directional couplers of which it is composed, when dealing with distant pump, signal, and idler frequencies. For what concerns the DC, we want to obtain a situation where the fields are directed in the MZI such that they overlap as much as possible in at least one of its arms. Here, we design a $Si_3N_4$ waveguide, on a $SiO_2$ substrate surrounded by air, of width $w = 400\,\text{nm}$ and height $h = 400\,\text{nm}$. With this waveguide parameters, we set the gap of the DCs to $g = 200\,\text{nm}$ and study the coupling as a function of the DC length $L_{\text{DC}}$ for the three frequencies of interested $\omega_P = 2415\,\text{rad/ps}$ ($\lambda_P = 780\,\text{nm}$), $\omega_S = 2141\,\text{rad/ps}$ ($\lambda_S = 880\,\text{nm}$), and $\omega_I = 2691\,\text{rad/ps}$ ($\lambda_I = 700\,\text{nm}$). The plot of the effective

coupling coefficient $\kappa_{\text{eff}}$ for pump (solid green), signal (dashed red), and idler (dotted blue) is shown in Fig. 3.28. From this, we choose the optimal length to split the fields in order to maximize the overlap. Therefor, with a DC length of $L_{\text{DC}} = 13.5\,\mu$m we have a (50):(50) splitting of both pump and signal frequencies and $\approx(0):(100)$ splitting ratio for the idler frequency. This means the three fields overlap in the arm of the interferometer belonging to Resonator 1. The tolerance on the DC length can be up to $0.5\,\mu$m without any significant change in the result. Instead, when designing the MZI, the key point is obtaining a $\pi$ phase shift for all the resonances. To do so, we cannot rely only on the tuning mechanism offered by an electrical heater, but we need to employ an interferometer with unequal arms length. In our design, we choose the proper path difference $\Delta L_{\text{MZI}} = 31.53\,\mu$m between the arms of the MZI that satisfies $\Delta\phi_m = k_m \Delta L_{\text{MZI}} = (2n+1)\pi$, with $n$ integer, for each $m = P, S, I$. The heater on one of the arm of the MZI is still fundamental, for it provides the fine tuning to correct any fabrication imperfection on $\Delta L_{\text{MZI}}$ and ensures the $\pi$ phase shift for all the resonances. In this design we are including the Bezier curves we studied in chapter 1 to allow for the realization of high-Q resonators. In fact, we can see the non-zero coupling at $L_{\text{DC}} = 0$ in Fig. 3.28. We stress that the use of Bezier curves helps lowering the scattering losses but increases the overall length of the resonators, reducing its finesse. Depending on the fabrication quality and technique, the use of Bezier curves can be preferable. In Fig. 3.29 we show the estimate we obtain for a MZI structure with length of the Bezier curves $L_B \simeq 92\,\mu$m, length of the short MZI
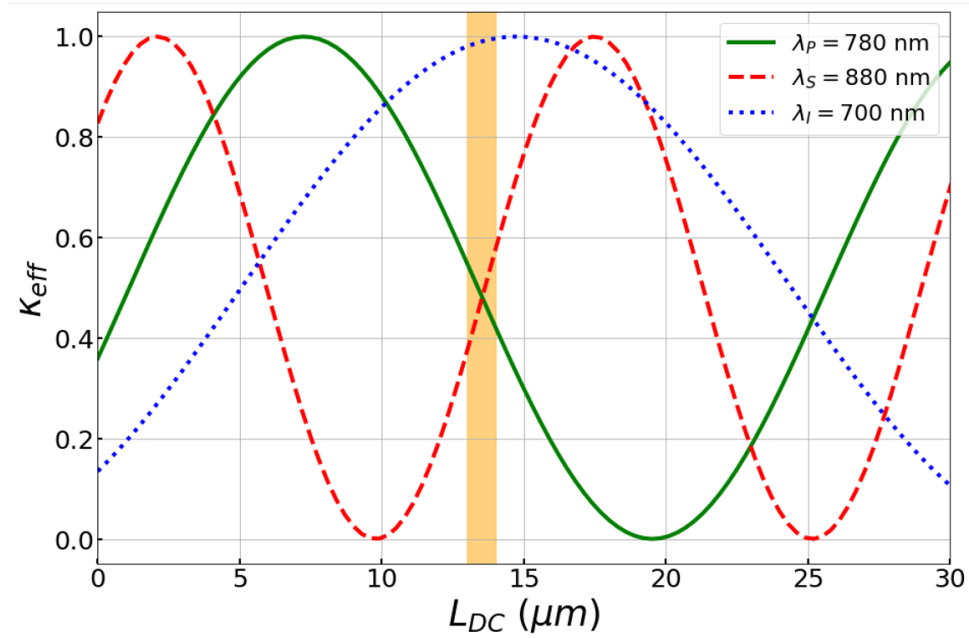


FIGURE 3.28. Effective coupling coefficient of the DC as a function of its length for the three frequencies of interest. The orange band indicates the chosen length and tolerance.
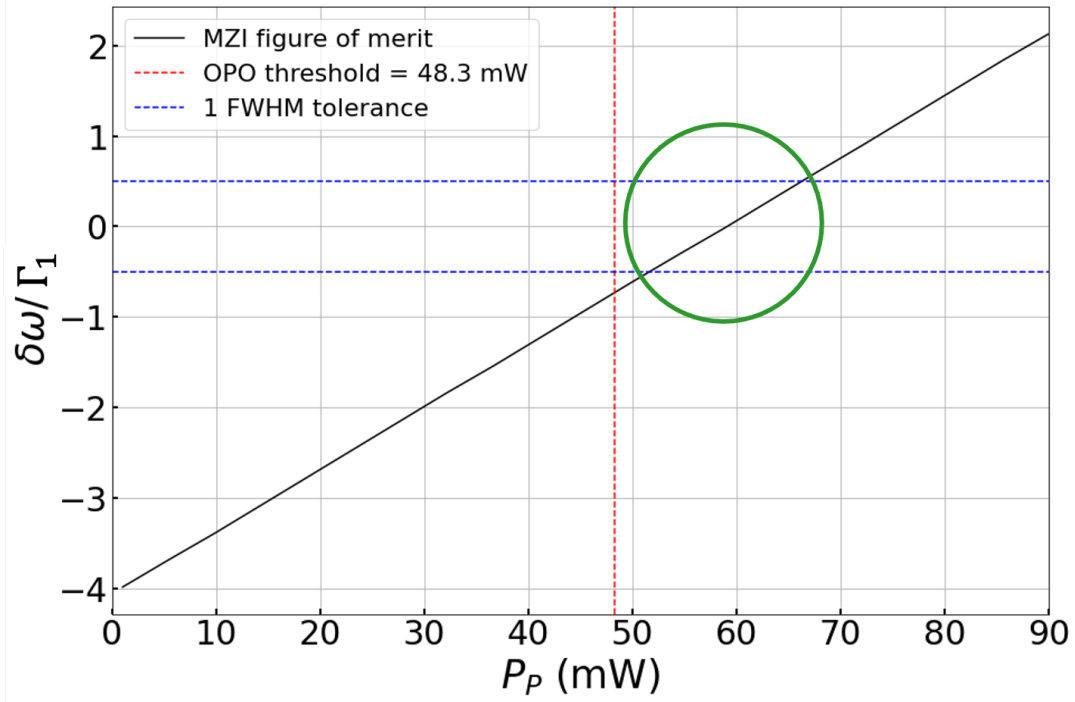
FIGURE 3.29. Figure of merit normalized by the resonator linewidth as a function of the pump power. The MZI working point is highlighted with the green circle, where the FOM is close to zero within one FWHM tolerance (dashed blue lines) and the injected power is larger than the OPO threshold (dashed red line).

arm $L_{\mathrm{MZI}} \simeq 168\,\mu$m and length of the long MZI arm $L_{\mathrm{MZI}} + \Delta L_{\mathrm{MZI}} \simeq 200\,\mu$m, for a total Resonator 1 length of $L_1 \simeq 575\,\mu$m and Resonator 2 length of $L_2 \simeq 606\,\mu$m. Both resonators have quality factors $Q \approx 10^6$ and linewidths $\Gamma_1 \simeq \Gamma_2 \simeq 3\,$rad/ns ($\approx 1\,$pm). With these parameters, the resonances of the cold structure, i.e. when the power is sufficiently low that Kerr effect can be neglected, are not aligned. As the pump power is increased, the FOM decreases, until it approaches zero. The goal is to get a zero FOM for a value higher, but as close as possible, to the OPO power threshold $P_{P,\mathrm{th}}^{\mathrm{MZI}} = 48.3\,$mW (dashed red line). In this simulation, we obtain a structure where the FOM is close to zero within one FWHM of tolerance (dashed blue lines) at $P_P \simeq 60\,$mW. This result shows how the realization of an OPO source that works in normal dispersion with relatively low pump power threshold is achievable.

# Conclusions

This research was focused on the theoretical study of the generation of nonclassical states of light via parametric fluorescence in integrated structure composed of two resonators by exploiting the coupling between them. In particular, we studied two phenomena: spontaneous parametric down-conversion (SPDC) and spontaneous four-wave mixing (SFWM). We developed the theory necessary to describe the generation of photon pairs in integrated photonic circuits, to understand how to increase the generation efficiency and, at the same time, how to gain control on the properties of the generated light. The core idea is to engineer some resonances of the system to overcome the limitation that are typical of simple structures like ring resonators. There, one can only play with the geometry of the waveguide forming the resonator to compensate for the material dispersion or use some tuning mechanism to rigidly shift the comb of the resonator. We examined two different strategies to achieve the same goal, by exploiting the coupling between the two resonators involved, and access to a new level of control of their properties. The first is the strong coupling strategy, the second is the linear uncoupling strategy.

Many results are the success of collaborations with theoretical and experimental research groups that made possible the comparison between different models and the realization of devices for experimental validation. We modelled nonlinear parametric processes in lossy integrated device in collaboration with the group at the University of Toronto (CA) [4, 90]. With Xanadu Quantum Technology (CA) we studied the squeezing in nanophotonic molecules, showing how with the strong coupling strategy one can tune only specific resonances of a comb, for example to suppress certain parasitic processes. With this technique it was possible to achieve record-level of squeezing on an integrated device, as reported in this work, thanks to the experiment carried out by the Xanadu team and to which we have contributed by providing theoretical support [60]. We investigated the advantages of the linear uncoupling strategy in several ways, in platforms that exploit both second- or third-order nonlinear interaction. In particular, we cooperated with the experimental groups at the University of Pavia and CEA-LETI in Grenoble (FR) by studying the design of the structure and its properties, actually demonstrating the suppression of the parasitic processes [69, 70], and in collaboration with the experimental group at the University of Munster

(GE) we investigated the generation of separable photon pairs [83]. Finally, we realized the design of an integrated optical parametric oscillators in collaboration with the National Institute of Standard and Technologies in Maryland (US). For all the different scenarios, we simulated the systems and provided a design of the devices by determining the best structure parameters compatible with the current technology. The field of integrated photonics is becoming of paramount importance for the implementation of practical quantum technologies, where reliable and efficient sources of nonclassical states of light are desirable. This research aims towards that direction, providing a practical and flexible solution.

# Some analytical calculation

## A.1. Analytic calculation of the Lorentzian shape of the resonances

Equation (3.22) is calculated from the Lorentzian shape of signal and idler resonances

$$
\ell(\omega_1) =
\left[ \frac{\frac{\Gamma_{2,S}^2}{4}}{\frac{\Gamma_{2,S}^2}{4} + (\omega_1 - \omega_S)^2} + \frac{\frac{\Gamma_{2,I}^2}{4}}{\frac{\Gamma_{2,I}^2}{4} + (\omega_1 - \omega_I)^2} \right] ,
\tag{A.1}
$$

and

$$
\ell(2\omega_P - \omega_1) =
\left[ \frac{\frac{\Gamma_{2,S}^2}{4}}{\frac{\Gamma_{2,S}^2}{4} + (2\omega_P - \omega_1 - \omega_S)^2} + \frac{\frac{\Gamma_{2,I}^2}{4}}{\frac{\Gamma_{2,I}^2}{4} + (2\omega_P - \omega_1 - \omega_I)^2} \right]
$$

$$
= \left[ \frac{\frac{\Gamma_{2,S}^2}{4}}{\frac{\Gamma_{2,S}^2}{4} + (\omega_1 - \omega_I)^2} + \frac{\frac{\Gamma_{2,I}^2}{4}}{\frac{\Gamma_{2,I}^2}{4} + (\omega_1 - \omega_S)^2} \right] ,
\tag{A.2}
$$

where we have considered signal and idler photons to be indistinguishable, and thus that they both can be generated in the resonance around $\omega_S$ and in that around $\omega_I$. These give the expression

$$
\mathcal{L}(\omega_1, 2\omega_P - \omega_1) = \ell(\omega_1)\ell(2\omega_P - \omega_1) \approx
$$

$$
\left[ \frac{\frac{\Gamma_{2,S}^2}{4}}{\frac{\Gamma_{2,S}^2}{4} + (\omega_1 - \omega_S)^2} \frac{\frac{\Gamma_{2,I}^2}{4}}{\frac{\Gamma_{2,I}^2}{4} + (\omega_1 - \omega_S)^2} \right] +
$$

$$
\left[ \frac{\frac{\Gamma_{2,S}^2}{4}}{\frac{\Gamma_{2,S}^2}{4} + (\omega_1 - \omega_I)^2} \frac{\frac{\Gamma_{2,I}^2}{4}}{\frac{\Gamma_{2,I}^2}{4} + (\omega_1 - \omega_I)^2} \right] =
$$

$$
\mathcal{C}_1(\omega_1) + \mathcal{C}_2(\omega_1) ,
\tag{A.3}
$$

where we have neglected the product of Lorentzians centered at different frequencies, given that generally $\text{FSR}_i \gg \Gamma_{i,m}$. This leads to

$$\int d\omega_1 \omega_1 (2\omega_P - \omega_1)\mathcal{L}(\omega_1, 2\omega_P - \omega_1) =$$

$$\int d\omega_1 \omega_1 (2\omega_P - \omega_1)\left[\mathcal{C}_1(\omega_1) + \mathcal{C}_2(\omega_1)\right] \ , \tag{A.4}$$

where

$$\int d\omega_1 \omega_1 (2\omega_P - \omega_1)\mathcal{C}_1(\omega_1) =$$

$$\pi \frac{\frac{\Gamma_{2,S}}{2}\frac{\Gamma_{2,I}}{2}}{\frac{\Gamma_{2,S}^2}{4} - \frac{\Gamma_{2,I}^2}{4}}\left[\frac{\Gamma_{2,S}}{2}\left(2\omega_P\omega_S + \frac{\Gamma_{2,I}^2}{4} - \omega_S^2\right)\right.$$

$$\left.- \frac{\Gamma_{2,I}}{2}\left(2\omega_P\omega_S + \frac{\Gamma_{2,S}^2}{4} - \omega_S^2\right)\right] =$$

$$\frac{\pi}{2}\frac{\Gamma_{2,S}\Gamma_{2,I}\left(2\omega_P\omega_S - \omega_S^2\right)}{(\Gamma_{2,S} + \Gamma_{2,I})(\Gamma_{2,S} - \Gamma_{2,I})}(\Gamma_{2,S} - \Gamma_{2,I}) =$$

$$\frac{\pi}{2}\frac{\Gamma_{2,S}\Gamma_{2,I}}{(\Gamma_{2,S} + \Gamma_{2,I})}\left(2\omega_P\omega_S - \omega_S^2\right) =$$

$$\frac{\pi}{2}\frac{\Gamma_{2,S}\Gamma_{2,I}}{(\Gamma_{2,S} + \Gamma_{2,I})}\left(\omega_S\omega_I\right) \ , \tag{A.5}$$

in which we considered $\left(2\omega_P\omega_S + \frac{\Gamma_{2,m}^2}{4} - \omega_S^2\right) \approx \left(2\omega_P\omega_S - \omega_S^2\right)$, since $\Gamma_{2,m} \ll \omega_m^2$, and

$$\int d\omega_1 \omega_1 (2\omega_P - \omega_1)\mathcal{C}_2(\omega_1) =$$

$$\frac{\pi}{2}\frac{\Gamma_{2,S}\Gamma_{2,I}}{(\Gamma_{2,S} + \Gamma_{2,I})}\left(2\omega_P\omega_I - \omega_I^2\right) =$$

$$\frac{\pi}{2}\frac{\Gamma_{2,S}\Gamma_{2,I}}{(\Gamma_{2,S} + \Gamma_{2,I})}\left(\omega_S\omega_I\right) \ , \tag{A.6}$$

and hence to the final value

$$\int d\omega_1 \omega_1 (2\omega_P - \omega_1)\mathcal{L}(\omega_1, 2\omega_P - \omega_1) =$$

$$\pi \frac{\Gamma_{2,S}\Gamma_{2,I}}{(\Gamma_{2,S} + \Gamma_{2,I})}\left(\omega_S\omega_I\right) \ , \tag{A.7}$$

of equation (3.23).

## A.2. Analytic calculation of $\mathcal{J}$-spatial

In the case of perfect uncoupling via the DC we have $f_{\mathrm{up},\omega_{1(2)}}(0) = f_{\mathrm{lo},\omega_{3(4)}}(0) = 0$, and hence the condition (3.3) for each frequency simplifies to

$$
\begin{cases}
f^{\mathrm{DC}}_{\mathrm{up},\omega_{1(2)}}(z) = -i f_{\mathrm{lo},\omega_{1(2)}}(0) \sin(|\kappa_{\mathrm{DC}}|z) \\
f^{\mathrm{DC}}_{\mathrm{up},\omega_{3(4)}}(z) = f_{\mathrm{up},\omega_{3(4)}}(0) \cos(|\kappa_{\mathrm{DC}}|z) \\
f^{\mathrm{DC}}_{\mathrm{up},\omega_{1(2)}}(z) = f_{\mathrm{up},\omega_{1(2)}}(0) \cos(|\kappa_{\mathrm{DC}}|z) \\
f^{\mathrm{DC}}_{\mathrm{up},\omega_{3(4)}}(z) = -i f_{\mathrm{lo},\omega_{3(4)}}(0) \sin(|\kappa_{\mathrm{DC}}|z)
\end{cases} ,
\tag{A.8}
$$

giving, from (3.18),

$$
\mathcal{J}_{\mathrm{up}}(\omega_1, \omega_2, \omega_3, \omega_4) = \mathcal{J}_{\mathrm{lo}}(\omega_1, \omega_2, \omega_3, \omega_4) =
$$
$$
f_{\mathrm{lo},\omega_1}(0) f_{\mathrm{lo},\omega_2}(0) f_{\mathrm{up},\omega_3}(0) f_{\mathrm{up},\omega_4}(0) \times
$$
$$
\int_0^{L_{\mathrm{DC}}} i^2 \sin^2(|\kappa_{\mathrm{DC}}|z) \cos^2(|\kappa_{\mathrm{DC}}|z) e^{i\Delta k z} dz
\tag{A.9}
$$

and hence

$$
\mathcal{J}(\omega_1, \omega_2, \omega_3, \omega_4) =
$$
$$
f_{\mathrm{lo},\omega_1}(0) f_{\mathrm{lo},\omega_2}(0) f_{\mathrm{up},\omega_3}(0) f_{\mathrm{up},\omega_4}(0) \mathcal{J}^{\mathrm{DC}}_{\mathrm{spatial}} ,
\tag{A.10}
$$

with

$$
\mathcal{J}^{\mathrm{DC}}_{\mathrm{spatial}} = 2 \int_0^{L_{\mathrm{DC}}} - \cos^2(\kappa_{\mathrm{DC}} z) \sin^2(\kappa_{\mathrm{DC}} z) e^{i\Delta k z} dz
$$
$$
\approx -\frac{L_{\mathrm{DC}}}{4} \left[ 1 - \mathrm{sinc}(4\kappa_{\mathrm{DC}} L_{\mathrm{DC}}) \right] .
\tag{A.11}
$$

Similarly, in the case of perfect uncoupling via a MZI coupler, we have $f^{(1)}_{-,\omega_{1(2)}} = f^{(2)}_{-,\omega_{3(4)}} = 0$ and, if we assume balanced beam splitters, $\sigma_{\mathrm{dx}} = \sigma_{\mathrm{sx}} = \sigma$ (and hence $\kappa_{\mathrm{dx}} = \kappa_{\mathrm{sx}} = \kappa$), condition (3.13) for the different frequencies simplifies in

$$
\begin{cases}
f^{\mathrm{MZI}}_{\mathrm{up},\omega_{1(2)}}(z) = i\kappa f^{(2)}_{-,\omega_{1(2)}} \\
f^{\mathrm{MZI}}_{\mathrm{up},\omega_{3(4)}}(z) = \sigma f^{(1)}_{-,\omega_{3(4)}} \\
f^{\mathrm{MZI}}_{\mathrm{lo},\omega_{1(2)}}(z) = \sigma f^{(2)}_{-,\omega_{1(2)}} \\
f^{\mathrm{MZI}}_{\mathrm{lo},\omega_{3(4)}}(z) = i\kappa f^{(1)}_{-,\omega_{3(4)}}
\end{cases} ,
\tag{A.12}
$$

and, from (3.18),

$$\mathcal{J}_{\text{up}}(\omega_1, \omega_2, \omega_3, \omega_4) = \mathcal{J}_{\text{lo}}(\omega_1, \omega_2, \omega_3, \omega_4) =$$

$$f_{-,\omega_1}^{(2)} f_{-,\omega_2}^{(2)} f_{-,\omega_3}^{(1)} f_{-,\omega_4}^{(1)} \int_0^{L_{\text{MZI}}} i^2 \sigma^2 \kappa^2 e^{i\Delta k z} dz, \tag{A.13}$$

and hence

$$\mathcal{J}(\omega_1, \omega_2, \omega_3, \omega_4) = f_{-,\omega_1}^{(2)} f_{-,\omega_2}^{(2)} f_{-,\omega_3}^{(1)} f_{-,\omega_4}^{(1)} \mathcal{J}_{\text{spatial}}^{\text{MZI}} , \tag{A.14}$$

with

$$\mathcal{J}_{\text{spatial}}^{\text{MZI}} = 2 \int_0^{L_{\text{MZI}}} (-\sigma^2 \kappa^2 e^{i\Delta k z}) dz \approx -\frac{L_{\text{MZI}}}{2} , \tag{A.15}$$

in the case of 50:50 point couplers ($\sigma = \kappa = 1/\sqrt{2}$).

## A.3. Generation rates in terms of Finesse

The expression for the generation rate can be written in terms of the finesse $\mathcal{F}$ of the resonators, thanks to the relation found in section II. For example, at the critical coupling condition, we have

$$R_{\text{pair}}^{\text{ring}} = \left( \frac{\gamma_{\text{NL}} P_P}{\omega_P} \right)^2 \left( \frac{\mathcal{F}_S}{\pi} \right) \left( \frac{\mathcal{F}_I}{\pi} \right) \left( \frac{\mathcal{F}_P}{\pi} \right)^2$$

$$\times \frac{\Gamma_{2,S} \Gamma_{2,I}}{\Gamma_{2,S} + \Gamma_{2,I}} (\omega_S \omega_I) \frac{L^2}{4} , \tag{A.16}$$

$$R_{\text{pair}}^{\text{DC}} = \left( \frac{\gamma_{\text{NL}} P_P}{\omega_P} \right)^2 \left( \frac{\mathcal{F}_S}{\pi} \right) \left( \frac{\mathcal{F}_I}{\pi} \right) \left( \frac{\mathcal{F}_P}{\pi} \right)^2$$

$$\times \frac{\Gamma_{2,S} \Gamma_{2,I}}{\Gamma_{2,S} + \Gamma_{2,I}} (\omega_S \omega_I) \frac{L_{\text{DC}}^2}{64} , \tag{A.17}$$

and

$$R_{\text{pair}}^{\text{MZI}} = \left( \frac{\gamma_{\text{NL}} P_P}{\omega_P} \right)^2 \left( \frac{\mathcal{F}_S}{\pi} \right) \left( \frac{\mathcal{F}_I}{\pi} \right) \left( \frac{\mathcal{F}_P}{\pi} \right)^2$$

$$\times \frac{\Gamma_{2,S} \Gamma_{2,I}}{\Gamma_{2,S} + \Gamma_{2,I}} (\omega_S \omega_I) \frac{L_{\text{MZI}}^2}{16} . \tag{A.18}$$

# List of publications

## Peer-reviewed journals

- **Luca Zatti**, J. E. Sipe, and Marco Liscidini, *"Generation of photon pairs by spontaneous four-wave mixing in linearly uncoupled resonators"*, **Physical Review A** 107, 013514 (2023)

- F.A. Sabattoli, H. El Dirani, L. Youssef, L. Gianini, **L. Zatti**, F. Garrisi, D. Grassani, C. Petit-Etienne, E. Pargon, J.E. Sipe, M. Liscidini, C. Sciancalepore, D. Bajoni, and M. Galli, *"Nonlinear coupling of linearly uncoupled resonators through a Mach-Zehnder interferometer"*, **Applied Physics Letters** 121.20 (2022)

- M Banic, **L. Zatti**, M. Liscidini, J.E. Sipe, *"Two strategies for modeling nonlinear optics in lossy integrated photonic structures"*, **Physical Review A** 106 (4), 043707 (2022)

- **Luca Zatti**, Nicola Bergamasco, Emma Lomonte, Francesco Lenzini, Wolfram Pernice, Marco Liscidini, *"Spontaneous Parametric Downconversion in Linearly Uncoupled Resonators"*, **Optics Letters** 47 (7), 1766-1769 (2022)

- F.A. Sabattoli, H. El Dirani, L. Youssef, F. Garrisi, D. Grassani, **L. Zatti**, C. Petit-Etienne, E. Pargon, J.E. Sipe, M. Liscidini, C. Sciancalepore, D. Bajoni, and M. Galli, *"Suppression of parasitic nonlinear processes in spontaneous four-wave mixing in linearly uncoupled resonators"*, **Physical Review Letters** 127 (3), 033901 (2021)

- Y. Zhang, M. Menotti, K. Tan, V. Vaidya, D. Mahler, L. Helt, **L. Zatti**, M. Liscidini, B. Morrison, and Z. Vernon, *"Squeezed light from a nanophotonic molecule"*, **Nature Communications**, 12 (1), 1-6 (2021)

## Conference Proceedings

- M. Banic, **L. Zatti**, M. Liscidini, JE Sipe, *"Out, Lost, or Broken: Photon Pairs from a Lossy Resonator"*, CLEO: QELS‗Fundamental Science, JTu3A. 20 (2022)

- **L. Zatti**, N. Bergamasco, E. Lomonte, F. Lenzini, W. Penrice, M. Liscidini, *"Spontaneous Parametric Down Conversion in Linearly Uncoupled Resonators"*, CLEO (2021)

- F.A. Sabattoli, H. El Dirani, L. Youssef, F. Garrisi, D. Grassani, **L. Zatti**, C. Petit-Etienne, E. Pargon, J.E. Sipe, M. Liscidini, C. Sciancalepore, D. Bajoni, M.

Galli, *"Suppression of Nonlinear Parasitic Processes in Linearly Uncoupled Silicon Resonators"*, CLEO: QELS_Fundamental Science, FTu2N. 4 (2021)

- F.A. Sabattoli, H. El Dirani, L. Youssef, F. Garrisi, D. Grassani, **L. Zatti**, L. Gianini, Camille Petit-Etienne, E. Pargon, JE Sipe, Marco Liscidini, C. Sciancalepore, D. Bajoni, M. Galli, *"Selective enhancement of nonlinear processes in linearly uncoupled silicon resonators"*, Smart Photonic and Optoelectronic Integrated Circuits XXIII 11690, 84-93 (2021)

- Sabattoli F.A., El Dirani H., Youssef L., Garrisi F., **Zatti L.**, Petit-Etienne C., Pargon E., Liscidini M., Sciancalepore C., Bajoni D., Galli M., *"Dual Pump Photonic Pair Generation with Suppression of Parasitic Processes in Linearly Uncoupled Silicon Resonators"*, Frontiers in Optics, FM4A. 2 (2020)

- **L. Zatti**, J.E. Sipe, and M. Liscidini, *"Engineering non-classical light in photonic integrated devices with linearly coupled and uncoupled resonators"*, 22nd International Conference on Transparent Optical Networks (ICTON), 1-4 (2020)

# Bibliography

[1] Nicolás Quesada and JE Sipe. "Why you should not use the electric field to quantize in nonlinear optics". In: *Optics letters* 42.17 (2017), pp. 3443–3446.

[2] G Breit and HA Bethe. "Ingoing waves in final state of scattering problems". In: *Physical Review* 93.4 (1954), p. 888.

[3] M Liscidini, LG Helt, and JE Sipe. "Asymptotic fields for a Hamiltonian treatment of nonlinear electromagnetic phenomena". In: *Physical Review A* 85.1 (2012), p. 013833.

[4] Milica Banic et al. "Two strategies for modeling nonlinear optics in lossy integrated photonic structures". In: *Physical Review A* 106.4 (2022), p. 043707.

[5] Matthias Stegmaier and Wolfram HP Pernice. "Mode control and mode conversion in nonlinear aluminum nitride waveguides". In: *Optics Express* 21.22 (2013), pp. 26742–26761.

[6] Xiang Guo, Chang-Ling Zou, and Hong X Tang. "Second-harmonic generation in aluminum nitride microrings with 2500%/W conversion efficiency". In: *Optica* 3.10 (2016), pp. 1126–1131.

[7] Chi Xiong et al. "Integrated GaN photonic circuits on silicon (100) for second harmonic generation". In: *Optics express* 19.11 (2011), pp. 10462–10470.

[8] Jianwei Wang et al. "Gallium arsenide (GaAs) quantum photonic waveguide circuits". In: *Optics Communications* 327 (2014), pp. 49–55.

[9] Lin Chang et al. "Strong frequency conversion in heterogeneously integrated GaAs resonators". In: *APL Photonics* 4.3 (2019), p. 036103.

[10] Iännis Roland et al. "Frequency doubling and parametric fluorescence in a four-port aluminum gallium arsenide photonic chip". In: *Optics Letters* 45.10 (2020), pp. 2878–2881.

[11] David P Lake et al. "Efficient telecom to visible wavelength conversion in doubly resonant gallium phosphide microdisks". In: *Applied Physics Letters* 108.3 (2016), p. 031109.

[12] Amnon Yariv and Pochi Yeh. *Photonics: optical electronics in modern communications*. Oxford university press, 2007.

[13] Mian Zhang et al. "Monolithic ultra-high-Q lithium niobate microring resonator". In: *Optica* 4.12 (2017), pp. 1536–1537.

[14]   Andreas Boes et al. "Status and potential of lithium niobate on insulator (LNOI) for photonic integrated circuits". In: *Laser & Photonics Reviews* 12.4 (2018), p. 1700256.

[15]   Michael Kues et al. "On-chip generation of high-dimensional entangled quantum states and their coherent control". In: *Nature* 546.7660 (2017), pp. 622–626.

[16]   Zhenshan Yang, Marco Liscidini, and John E Sipe. "Spontaneous parametric down-conversion in waveguides: a backward Heisenberg picture approach". In: *Physical Review A* 77.3 (2008), p. 033808.

[17]   Stefano Azzini et al. "From classical four-wave mixing to parametric fluorescence in silicon microring resonators". In: *Optics letters* 37.18 (2012), pp. 3807–3809.

[18]   Jacob S Levy et al. "CMOS-compatible multiple-wavelength oscillator for on-chip optical interconnects". In: *Nature photonics* 4.1 (2010), pp. 37–40.

[19]   Marcello Ferrera et al. "Low-power continuous-wave nonlinear optics in doped silica glass integrated waveguide structures". In: *Nature photonics* 2.12 (2008), pp. 737–740.

[20]   David J Moss et al. "New CMOS-compatible platforms based on silicon nitride and Hydex for nonlinear optics". In: *Nature photonics* 7.8 (2013), pp. 597–607.

[21]   E Timurdogan et al. "Electric field-induced second-order nonlinear optical effects in silicon waveguides". In: *Nature Photonics* 11.3 (2017), pp. 200–206.

[22]   Xueyue Zhang et al. "Symmetry-breaking-induced nonlinear optics at a microcavity surface". In: *Nature Photonics* 13.1 (2019), pp. 21–24.

[23]   Edgars Nitiss et al. "Optically reconfigurable quasi-phase-matching in silicon nitride microresonators". In: *Nature Photonics* 16.2 (2022), pp. 134–141.

[24]   JE Sipe et al. "Effective field theory for the nonlinear optical properties of photonic crystals". In: *Physical Review E* 69.1 (2004), p. 016604.

[25]   Lukas G Helt, Marco Liscidini, and John E Sipe. "How does it scale? Comparing quantum and classical nonlinear optical processes in integrated devices". In: *JOSA B* 29.8 (2012), pp. 2199–2212.

[26]   Avik Dutt et al. "On-chip optical squeezing". In: *Physical Review Applied* 3.4 (2015), p. 044005.

[27]   John Heebner, Rohit Grover, and Tarek Ibrahim. *Optical microresonator theory.* Springer, 2008.

[28]   Davide Grassani et al. "Micrometer-scale integrated silicon source of time-energy entangled photons". In: *Optica* 2.2 (2015), pp. 88–94.

[29]   Joshua W Silverstone et al. "Qubit entanglement between ring-resonator photon-pair sources on a silicon chip". In: *Nature communications* 6.1 (2015), pp. 1–7.

[30] Jose A Jaramillo-Villegas et al. "Persistent energy–time entanglement covering multiple resonances of an on-chip biphoton frequency comb". In: *Optica* 4.6 (2017), pp. 655–658.

[31] Jacob T Robinson, Long Chen, and Michal Lipson. "On-chip gas detection in silicon optical microcavities". In: *Optics Express* 16.6 (2008), pp. 4296–4301.

[32] Stéphane Clemmen et al. "Continuous wave photon pair generation in silicon-on-insulator waveguides and ring resonators". In: *Optics express* 17.19 (2009), pp. 16558–16570.

[33] Lewis Hill et al. "Effects of self-and cross-phase modulation on the spontaneous symmetry breaking of light in ring resonators". In: *Physical Review A* 101.1 (2020), p. 013823.

[34] MODE Finite Difference Eigenmode Solver, Ansys Lumerical.

[35] Michael E. Mortenson. *Mathematics for computer graphics applications*. Industrial Press Inc., 1999.

[36] Isidor Isaac Rabi. "Space quantization in a gyrating magnetic field". In: *Physical Review* 51.8 (1937), p. 652.

[37] Christopher Gerry, Peter Knight, and Peter L Knight. *Introductory quantum optics*. Cambridge university press, 2005.

[38] M e Tse et al. "Quantum-enhanced advanced LIGO detectors in the era of gravitational-wave astronomy". In: *Physical Review Letters* 123.23 (2019), p. 231107.

[39] Benjamin P Abbott et al. "Prospects for observing and localizing gravitational-wave transients with Advanced LIGO, Advanced Virgo and KAGRA". In: *Living reviews in relativity* 23.1 (2020), pp. 1–69.

[40] Joonsuk Huh et al. "Boson sampling for molecular vibronic spectra". In: *Nature Photonics* 9.9 (2015), pp. 615–620.

[41] Juan Miguel Arrazola and Thomas R Bromley. "Using Gaussian boson sampling to find dense subgraphs". In: *Physical review letters* 121.3 (2018), p. 030503.

[42] Thomas R Bromley et al. "Applications of near-term photonic quantum computers: software and algorithms". In: *Quantum Science and Technology* 5.3 (2020), p. 034010.

[43] Xiaogang Qiang et al. "Large-scale silicon quantum photonics implementing arbitrary two-qubit processing". In: *Nature photonics* 12.9 (2018), pp. 534–539.

[44] Rodney Loudon. *The quantum theory of light*. OUP Oxford, 2000.

[45] HA Bachor and TC Ralph. "A guide to experiments in quantum optics (Wiley". In: *VCH Verlag Gmbh & Co., Weinheim* 10 (2004), p. 9783527619238.

[46] R E Slusher et al. "Observation of squeezed states generated by four-wave mixing in an optical cavity". In: *Physical review letters* 55.22 (1985), p. 2409.

[47] Henning Vahlbruch et al. "Detection of 15 dB squeezed states of light and their application for the absolute calibration of photoelectric quantum efficiency". In: *Physical review letters* 117.11 (2016), p. 110801.

[48] Avik Dutt et al. "Tunable squeezing using coupled ring resonators on a silicon nitride chip". In: *Optics letters* 41.2 (2016), pp. 223–226.

[49] Varun D Vaidya et al. "Broadband quadrature-squeezed vacuum and nonclassical photon number correlations from a nanophotonic device". In: *Science advances* 6.39 (2020), eaba9186.

[50] Amir H Safavi-Naeini et al. "Squeezed light from a silicon micromechanical resonator". In: *Nature* 500.7461 (2013), pp. 185–189.

[51] Robert Cernansky and Alberto Politi. "Nanophotonic source of quadrature squeezing via self-phase modulation". In: *APL Photonics* 5.10 (2020), p. 101303.

[52] Guanhao Huang et al. "Thermorefractive noise in silicon-nitride microresonators". In: *Physical Review A* 99.6 (2019), p. 061801.

[53] Yuan Guo et al. "Telecom-band degenerate-frequency photon pair generation in silicon microring cavities". In: *Optics letters* 39.8 (2014), pp. 2526–2529.

[54] Z Vernon et al. "Scalable squeezed-light source for continuous-variable quantum sampling". In: *Physical Review Applied* 12.6 (2019), p. 064024.

[55] Stefan Ast, Moritz Mehmet, and Roman Schnabel. "High-bandwidth squeezed light at 1550 nm from a compact monolithic PPKTP cavity". In: *Optics Express* 21.11 (2013), pp. 13572–13579.

[56] LG Helt et al. "Parasitic photon-pair suppression via photonic stop-band engineering". In: *Physical Review Letters* 118.7 (2017), p. 073603.

[57] Stefano Azzini et al. "Ultra-low power generation of twin photons in a compact silicon ring resonator". In: *Optics express* 20.21 (2012), pp. 23100–23107.

[58] Imad Agha et al. "Low-noise chip-based frequency conversion by four-wave-mixing Bragg scattering in SiN x waveguides". In: *Optics letters* 37.14 (2012), pp. 2997–2999.

[59] Yun Zhao et al. "Near-degenerate quadrature-squeezed vacuum generation on a silicon-nitride chip". In: *Physical Review Letters* 124.19 (2020), p. 193601.

[60] Y Zhang et al. "Squeezed light from a nanophotonic molecule". In: *Nature communications* 12.1 (2021), pp. 1–6.

[61] RJC Spreeuw et al. "Classical realization of a strongly driven two-level system". In: *Physical review letters* 65.21 (1990), p. 2642.

[62] Tobias Grossmann et al. "Polymeric photonic molecule super-mode lasers on silicon". In: *Light: Science & Applications* 2.5 (2013), e82–e82.

[63] Mian Zhang et al. "Electronically programmable photonic molecule". In: *Nature Photonics* 13.1 (2019), pp. 36–40.

[64] Cale M Gentry, Xiaoge Zeng, and Miloš A Popović. "Tunable coupled-mode dispersion compensation and its application to on-chip resonant four-wave mixing". In: *Optics letters* 39.19 (2014), pp. 5689–5692.

[65] Mikkel Heuck et al. "Unidirectional frequency conversion in microring resonators for on-chip frequency-multiplexed single-photon sources". In: *New Journal of Physics* 21.3 (2019), p. 033037.

[66] Kosuke Fukui et al. "High-threshold fault-tolerant quantum computation with analog quantum error correction". In: *Physical review X* 8.2 (2018), p. 021054.

[67] M Menotti et al. "Nonlinear Coupling of Linearly Uncoupled Resonators". In: *Physical review letters* 122.1 (2019), p. 013904.

[68] K Tan et al. "Stimulated four-wave mixing in linearly uncoupled resonators". In: *Optics Letters* 45.4 (2020), pp. 873–876.

[69] Federico Andrea Sabattoli et al. "Suppression of Parasitic Nonlinear Processes in Spontaneous Four-Wave Mixing with Linearly Uncoupled Resonators". In: *Physical Review Letters* 127.3 (2021), p. 033901.

[70] F.A. Sabattoli et al. "Nonlinear coupling of linearly uncoupled resonators through a Mach-Zehnder interferometer". In: *Applied Physics Letters* 121.20 (2022), p. 201101.

[71] T Onodera et al. "Parametric fluorescence in a sequence of resonators: An analogy with Dicke superradiance". In: *Physical Review A* 93.4 (2016), p. 043837.

[72] Robert W Boyd. *Nonlinear optics*. Academic press, 2020.

[73] Martin HP Pfeiffer et al. "Ultra-smooth silicon nitride waveguides based on the Damascene reflow process: fabrication and loss origins". In: *Optica* 5.7 (2018), pp. 884–892.

[74] Houssein El Dirani et al. "Ultralow-loss tightly confining Si 3 N 4 waveguides and high-Q microresonators". In: *Optics express* 27.21 (2019), pp. 30726–30740.

[75] SM Spillane et al. "Ideality in a fiber-taper-coupled microresonator system for application to cavity quantum electrodynamics". In: *Physical review letters* 91.4 (2003), p. 043902.

[76] Erman Engin et al. "Photon pair generation in a silicon micro-ring resonator with reverse bias enhancement". In: *Optics express* 21.23 (2013), pp. 27826–27834.

[77] Boris Desiatov et al. "Ultra-low-loss integrated visible photonics using thin-film lithium niobate". In: *Optica* 6.3 (2019), pp. 380–384.

[78] Luisa Ottaviano et al. "Low-loss high-confinement waveguides and microring resonators in AlGaAs-on-insulator". In: *Optics Letters* 41.17 (2016), pp. 3996–3999.

[79] Yuntao Xu et al. "Mitigating photorefractive effect in thin-film lithium niobate microring resonators". In: *Optics Express* 29.4 (2021), pp. 5497–5504.

[80]   Yaowen Hu et al. "On-chip electro-optic frequency shifters and beam splitters".
       In: *Nature* 599.7886 (2021), pp. 587–593.

[81]   Cheng Wang et al. "Nanophotonic lithium niobate electro-optic modulators".
       In: *Optics express* 26.2 (2018), pp. 1547–1555.

[82]   Emma Lomonte et al. "Single-photon detection and cryogenic reconfigurabil-
       ity in lithium niobate nanophotonic circuits". In: *Nature Communications* 12.1
       (2021), pp. 1–10.

[83]   Luca Zatti et al. "Spontaneous parametric downconversion in linearly uncoupled
       resonators". In: *Optics Letters* 47.7 (2022), pp. 1766–1769.

[84]   Emma Lomonte, Francesco Lenzini, and Wolfram HP Pernice. "Efficient self-
       imaging grating couplers on a lithium-niobate-on-insulator platform at near-
       visible and telecom wavelengths". In: *Optics Express* 29.13 (2021), pp. 20205–
       20216.

[85]   Z Vernon et al. "Truly unentangled photon pairs without spectral filtering". In:
       *Optics letters* 42.18 (2017), pp. 3638–3641.

[86]   JH Eberly. "Schmidt analysis of pure-state entanglement". In: *Laser physics*
       16.6 (2006), pp. 921–926.

[87]   Lucia Caspani et al. "Integrated sources of photon quantum states based on
       nonlinear optics". In: *Light: Science & Applications* 6.11 (2017), e17100–e17100.

[88]   Xiyuan Lu et al. "Milliwatt-threshold visible–telecom optical parametric oscil-
       lation using silicon nanophotonics". In: *Optica* 6.12 (2019), pp. 1535–1541.

[89]   Hasan Yildirim. "Dispersion parameters and nonlinear optical properties of sili-
       con nitride rib waveguides". In: *Optics Communications* 284.7 (2011), pp. 2031–
       2035.

[90]   Luca Zatti, J. E. Sipe, and Marco Liscidini. "Generation of photon pairs by
       spontaneous four-wave mixing in linearly uncoupled resonators". In: *Phys. Rev.
       A* 107 (1 2023), p. 013514.